UNIVERSITÀ
DEGLI STUDI
FIRENZE

PhD in
Physics and Astronomy
CYCLE XXXVI

COORDINATOR Prof. Giovanni Modugno

Assessment and optimization of electromagnetic performance of low-frequency antenna arrays (SKA) by means of numerical methods

Academic Discipline (SSD): FIS/05, ING-INF/02

Doctoral Candidate
Dr. Georgios Kyriakou

Supervisor
Dr. Pietro Bolli

Prof. Assoc. Marco Romoli
MarcoRomoli

Coordinator
Prof. Giovanni Modugno
Giovanni Modugno

σε όλες τις ψυχές που χάθηκαν πνιγμένες στη Μεσόγειο

to all the lost souls drowned in the Mediterranean

a tutte le disperse anime annegate nel Mediterraneo

Abstract

Antenna arrays are widely used in many RF applications, since they provide advantageous characteristics in combining element and array layout design. Radio astronomers need receiving array instruments especially at low frequencies to increase sensitivity and resolution; one such case is the Square Kilometer Array (SKA), which aims to be the most sensitive radiotelescope to be built. In this thesis, I investigate phenomena relating to both the single element as well as the array electromagnetic performance of SKA-Low, with an aim to characterize critical aspects of the instrument in terms of far-field receiving patterns, array network properties as well as polarization purity.

An overview of array advantages at low frequencies, as well as the SKA current design and implementation status comprise Chapter 1. The numerical EM methods used throughout the various analyses are outlined in Chapter 2, while SKALA4.1, the SKA-Low array element, is simulated using three different approaches: the Method of Moments, the Characteristic Modes Analysis and a dipole array simplified model. Spurious narrow-band phenomena relating to the log-periodic nature of SKALA4.1 are analysed in Chapter 3, where a dipole RLC loading method is proposed as a remedy. In Chapter 4, the ground plane is included in array simulations and its diffraction effects are quantified; a grid mesh analysis is also performed and compared to the solid plane simulations. Finally, in Chapter 5, mutual coupling between pairs of antennas is examined probing a first-order coupling framework, while mitigation strategies of the strong coupling features are tested with the two SKALA4.1 antennas.

Even though the sensitivity requirements of SKA are largely met with the current design, it is essential that certain spectral smoothness properties be also satisfied for certain scientific objectives that SKA-Low aims to attain. The focus on improving the spectral purity must however maintain the antenna characteristics; thus most of the proposed changes are minimal. The high accuracy desired necessitates the use of commercial solvers over in-house or non benchmarked tools; our analysis relies on numerical results from two commercial solvers, while some experimental results have also been obtained.

In the addendum of this thesis, the antenna used for the Large Experiment to detect the Dark Ages (LEDA) is simulated on various platforms of soil volume and ground plane surface. The antenna spectral response is in this case tested in greater rigor by examining a correction factor taking into account the sky brightness temperature; useful conclusions are drawn on the antenna beam requirements of such 21 cm global signal cosmology experiments. An array of such antennas known as the Long Wavelength Array (LWA) is also treated focusing on the mutual coupling effects.

Acknowledgments

During the three years of my research as a PhD candidate at the University of Florence, I have received financial support by the Arcetri Astrophysical Observatory (INAF-OAA), through the grant "Numerical analysis and development of new algorithms for the electromagnetic characterization of SKA1-LOW", which I hereby acknowledge.

I would like to thank my supervisor Dr. Pietro Bolli for all his guidance, support, insights and experience, which have been the most crucial factor in accomplishing this thesis. His personal integrity has also been definitive in my research attitude. I also thank my co-supervisor, Dr. Marco Romoli, for having overseen my PhD candidacy at the University of Florence.

My acknowledgements also extend to all the friends and colleagues I have met and interacted with at Arcetri; Giulia Macario, Paola di Ninni, Fabio Giovanardi have been good friends and collaborators, Renzo Nesti, Gianni Comoretto, Luca Olmi have always responded to my curiosities, Aldo Sonnini and Luca Cresci have been instrumental in lending their technical experience in the measurement campaigns performed. Many friends deserve a special mention: Seyma Mercimek, Matteo Barbetti, Antonio Garufi, Lorenzo Pino, Francesco Belfiore, Essna Ghose, Matilde Signorini have all been supportive during these years.

I would also like to thank my parents; they have supported all my choices and transpired to me a lot of personal values. I thank my sister for her personal support. My uncle, Giorgos, has been a constant positive force in my life; he unfortunately passed away very early during this year.

I would further like to thank Marta Spinelli for the fruitful collaboration and having introduced me to the RF challenges of 21 cm signal cosmology experiments, as well as Gianni Bernardi and Lincoln Greenhill for many productive meetings. Special thanks also to Giuseppe Virone, Lorenzo Ciorba, Lorenzo Mezzadrelli and Maria Grazia Labate for their valuable collaboration on various topics, as well as Maria Kovaleva and David Davidson for supervising my visit at CIRA in Western Australia.

Finally, I thank my best friends Lefteris, Philippos, Giannis for all the good times, and I thank Maria, my partner, for her constant, genuine support in difficult times.

Contents

Chapter 1

Low-frequency arrays in Radioastronomy and the Square Kilometer Array

1.1 Why *arrays* of antennas at low frequencies?

The question of designing an electromagnetic instrument for the reception of radio waves is largely dependent on the nature of the electromagnetic spectrum. Roughly speaking, the dimensions of any such instrument should be comparable to the wavelength of reception (or observation, in the case of radio astronomy). A very concise treatment of the general case of a receiving antenna, for quasi-monochromatic signals and elliptically polarized elements, can be found in [1], where one of the main antenna figures of merit, the effective aperture A_e, is derived. It can therefore readily be realised that the lower the frequency, the larger the instrument dimensions should be to achieve a sensitive aperture. This means that building such instruments can be challenging!

The question of size though has some certain constraints when one takes into account the capability of observation from the surface of the Earth. It is well known that radio waves lower than 10 MHz are largely blocked by the Earth's ionosphere [2], cancelling the usefulness of ground-based instruments for that frequency range. Since this rough limit corresponds to a wavelength of 30 meters, one can conclude that this is an attainable limit for engineers to construct instruments of that size. The need for larger sizes (or apertures) for radio observation has been further dictated by the capacity of the instrument to angularly resolve narrow sources in the sky.

To understand this, one can use the diffraction limit of an aperture antenna. This limit is just a spatial-domain expression of the Nyquist sampling rule for the aperture synthesis Fourier transform [3], [4], when using the Fraunhofer approximation for the aperture far-fields. This means that the inverse angular width $1/\Delta\theta$ ("inverse beamwidth") of observation and the wavelength normalized maximum size of the aperture R/λ are constrained as:

$$\frac{1}{\Delta\theta} \geq \frac{1}{2} \cdot \frac{R}{\lambda} \Rightarrow \Delta\theta \leq 2 \cdot \frac{\lambda}{R} \tag{1.1}$$

In practice, this constraint is even tighter if we want to better sample an angular extent without the confusion that sidelobes of any far-field pattern introduce (e.g., $1.22 \cdot \lambda/R$ if we limit the sampling angle at half the maximum of an Airy pattern on a circular aperture [4]). It is therefore clear that, while an object is detectable at 10 MHz with an aperture of 30 m, it can only be resolved at ≈ 2 rad of angular extent at the limit of the sampling theorem. This is quite a poor resolution and calls for larger instrument sizes to increase the signal resolution. Fortunately, this is not the only technique by which one can enhance the resolution.

The breakthrough of early radioastronomers was the use of interferometry in radio receiving systems. An interferometer works as a discrete set of receivers that combine their signals to simulate that of an aperture that would have the same size as that of their maximum distance. This is the most advantageous feature of interferometry. The possibility to electronically synthesize voltage correlations by introducing phase delays to the received signals is an additional preferable feature than that of mechanical movement. In fact, since this operation is done offline, one can recreate the received data of a quite large patch of observation, which corresponds to the limits of the so-called beamforming. The degradation of the antenna beam as well as the phase and amplitude compensation dictate what field of view is available from these offline data, and along with the acquisition rate, the Survey Speed of the instrument. An increased survey speed is very important for certain types of scientific applications, which require quick tracking of the astrophysical sources. An extensive treatment of interferometry in radio astronomy can be found in [5].

1.2 The Square Kilometer Array

The Square Kilometer Array (or SKA) is an intergovernmental effort to build the world's largest radiotelescope. It is a project that was conceived as early as the '90s [6], followed by working groups that have advanced the system design during the previous decade, while it has been given the construction 'green light' in 2021[1]. One of the main goals of the Square Kilometer Array is to detect the Cosmic Dawn and Epoch of Reionization cosmological radio signals, an important gap in our knowledge of the early universe. Other scientific objectives that the SKA will explore are comsic magnetism, galaxy evolution, pulsar science, the origins of life through molecular line spectroscopy, and many more that can be found in [7].

The project is split in two independent instruments, targetting different frequency bands: the SKA-Low and the SKA-Mid; as the name suggests, the total collecting area is around 1 km^2. The governance body, SKAO, is overseeing its operation while the SKA Regional Centers (SRC) will be a network of facilities established in many of the partner countries to coordinate access to the enormous amount of data, as well as user support and scientific tools for their processing. SKA aims to also usher in the area of Open Science, by promoting the FAIR (Findability, Accessibility, Interoperability, Reusability) principles and ensuring that modern technical solutions are employed to allow for efficient data processing by the broad scientific community[2][8].

---

[1] `https://www.skao.int/en/about-us/91/history-ska-project`

[2] `https://www.granadacongresos.com/skaopenscience`

1.2.1 SKA-Low

The low-frequency part of SKA is an array of log-periodic dipole antennas, as seen in Fig. 1.1, and its installation site is the Murchison area in the outback of Western Australia. These antennas are organized in a set of 512 so-called stations, each of which encompasses 256 antennas. This amounts to a total number of 131.072 antennas. The layout of each station is currently semi-random (in essence, a random algorithm determines the positions within a circular area while at the same time ensuring accessibility), while the configuration of the stations is a spiral-like structure. Fig. 1.2 features a combined view of an already constructed station with an artist's impression of the future array. Each station lies on a circular ground mesh, which ensures the low-frequency front-to-back ratio of the antenna patterns is compensated for, while it also protects from the more volatile soil platform which would induce more unpredictable systematics.

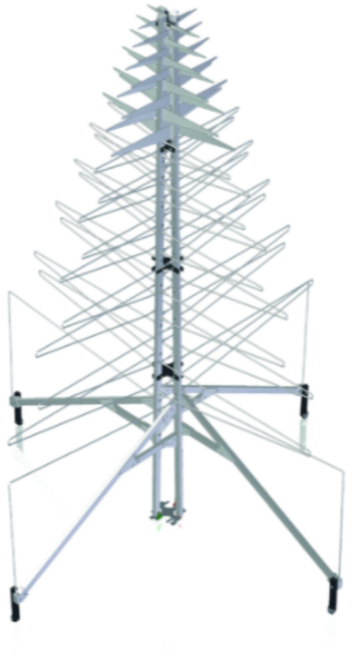

Figure 1.1. SKALA4.1 as-built antenna, occupying a 1.6 m × 1.6 m footprint and amounting to a height of 2.1 m.

The design of the single element that has been chosen for construction, is called SKALA4.1 [9] and is the evolution of previous design stages such as SKALA2, [10], SKALA3 [11]. It is a log-periodic dipole antenna composed of 20 dipoles, 19 of which are triangular, whereas the longest one has a bow-tie shape. This is intended to enhance the low-frequency response of the antenna down to 50 MHz, by using a more wideband geometric structure. The upper limit of its capacity is 350 MHz, ensuring a wide fractional bandwidth (7:1). Two rectangular conductors acting as a transmission line constitute its boom. SKALA4.1 is dual polarized, while its cross-polarization level is low (less than -11 dB). The Low-Noise Amplifier, in contrast with previous designs, is integrated in the higher boom ends via appropriately designed caps. This utilizes the shielding capability of the rectangular tube, both for the LNA and the coaxial cable that drives the RF signal to the Tile-Processing Modules (TPMs) of the station. The antenna is also hooked on the ground mesh for protection of the LNA electronics from electrostatic discharge.

The construction phase of SKA-Low is already commenced. After the operation of two Aperture Array Verification Stations (AAVS1[12] & 2 [13], respectively), both featuring a pseudorandom layout a third one is recently under comissioning. The first phase of the telescope is going to commence in 2024 [14]. A new, more canonical layout called the 'Vogel' is going to be tested with AAVS3 [15], which presents some benefits with respect to the mutual coupling mitigation. An overview of the semi-random and Vogel layouts implemented for AAVS2 & 3 respectively, can be found in [15, Fig. 3]. The single antenna footprint, which is 1.6 m, and the 38 m diameter of the wire mesh which is

Figure 1.2. Aerial view combined with artist's impression of the SKA-Low in the Murchison Radio Observatory, Western Australia, at the Wajarri-Yamatji people's traditional land.

the array 'platform', results in antennas that are very close to each other in AAVS2, while also aligned in some instances. This is quite detrimental for the mutual coupling; the Vogel layout ensures that every antenna polarization is misaligned at a minimum angle of $\approx 30°$ with respect to copolar elements of other antennas.

1.2.2 SKA-Mid

The SKA-Mid is another, separate array of antennas that are going to be built in South Africa, at Losberg (Karoo region). It will consist of 133 new dishes, along with the 64 already existing MeerKat dishes. Fig. 1.3 provides a similar combination of a photo of the MeerKat dishes with an artist's impression of the full array in the future. The dishes will be arranged in 3 logarithmic spirals, extending up to baselines of 150 km. The operating frequency range of SKA-Mid is between 0.35 GHz and 15.4 GHz, split in 4 bands, while it will use 4 feeds to cover these bands. The optics used is a Gregorian secondary focus, which is offset with respect to the main dish so as to allow for higher efficiency of the secondary beam, by avoiding feed blockage and ground spillover [16].

While the MeerKat dishes are unshaped, the new dishes will be shaped reflectors. Shaped reflectors are not exact paraboloids, but feature optimized 2D dish surfaces that can perform correction of optical aberrations. The diameter of the aperture is 15 m and the long axis of the system is 18.2 m. The subreflector diameter is ≈ 4.6 m and an extension of its lower rim allows for better shading of the ground, preventing in this way the noise temperature from rising. This is combined with a rotated pointing of the feed towards the primary dish, that increases the illumination efficiency. Using a shaped reflector further improves the illumination properties and reduces spillover, so it is the preferred way of achieving better gain and therefore

Figure 1.3. Aerial view of MeerKat combined with artist's impression of the SKA-Mid in the Karoo region of Losberg, South Africa.

sensitivity. For that purpose, studies have been carried out to optimize the mapping function which defines the reflector surface in [17, 18].

The feeds that will be mounted on the SKA-Mid dishes are single-pixel (single-port structures, so no simultaneous beams can be formed), and they are four, used in as many bands [19, 20]:

1. In Band 1 (350-1050 MHz) a so-called 'Quad-Ridged Flared Horn' will be used, which is a flared horn profile with four orthogonal ridges and readily provides for two linear polarizations. It has been developed at the Onsala Space Observatory and integrated electronics for signal calibration and amplifications are included in its 'package'.

2. In Band 2 (0.95-1.76 GHz) a wide flare angle horn is used, with axial corrugations, designed by EMSS antennas. Advanced cryogenics are required to cool down this feed and reduce the noise temperature, while an orthomode transducer (OMT) is used to separate the orthogonal polarizations.

3. In Bands 3, 4, 5a & b and 6 an integrated modular cryostat encompassing up to five horn feeds for each one of them has been designed by the Oxford University, and considerations of power consumption have also been made. The design is undergoing testing and its full capacity for all 5 bands is being investigated.

1.3 The necessity for electromagnetic simulations

The accurate description of the electromagnetic characteristics of any antenna is a crucial point in the design of an RF system, be it a radiotelescope, a mobile service station or a space probe [21, Ch. 1]. Apart from the engineering challenge of designing the correct geometric, material and modular properties of an antenna such that it conforms to a certain set of requirements (a task which for SKA-Low had been undertaken by the LFAA consortium [22]), a radiotelescope system like the SKA-Low presents new challenges that call for EM characterization. Specifically, the mutual coupling phenomena in a closely-packed array increase the complexity of the formed beam, such that calibration algorithms for the beam weighting gain and phase corrections at each antenna cannot simply rely on its response as an isolated element. This does not only mean that observational flux calibration needs new techniques to allow for the determination of a higher number of degrees of freedom that can be calibrated at a higher frequency of repetition (such as holography [23] and self-holography, [24]), but also that it needs the assistance of simulated patterns to accurately work [25].

While the presence of mutual coupling is certain due to the antenna electrical proximity, its mitigation by choosing specific array layouts is a task also assisted by electromagnetic simulations [26]. A theoretical understanding of the properties of coupled pairs or clusters of antennas is also desired, so that the optimization of the design is physics-driven rather than purely relying on generalized routines. Among the available suite of EM methods, we need fast solutions for the first task (in order to run multiple configurations), as well as methods that decompose the solution into blocks of sub-solutions (such as Characteristic Basis Functions or Characteristic Modes).

As far as an array is concerned, some of the challenges faced are:

- being able to create every single beam without multiple simulations by setting the desired excitations on the antenna array electromagnetic model
- coming up with faster computation techniques that can be applied to different excitation scenarios by breaking them down into local problems

The first point is solved by the linearity of the "vector space" of formed beams. One needs to find an underlying set of patterns that would act as a basis in order to apply weights at will after they are precomputed. A network-theory approach, which has been fully adapted to radioastronomical concepts in [21], enables the computation of Embedded Element Patterns (EEPs) as such a basis, which are patterns that result when one antenna is active and the other antennas are terminated with passive loads. The scattering parameters are also needed when one needs to convert such patterns from one loading condition to another or form the beam of an array mounted on a receiver front-end. Beamforming techniques can then also yield optimized results by leveraging optimization algorithms [27].

The second point arises in correlation to the first, when the inversion of the discretized matrix problem is sped up by domain-decomposition or other local methods (e.g., [28]). This means that when the number N of the Embedded Element Patterns is large, any such method which can speed up the computation of one EEP needs to do so at a rate less than $1/N$ for all useful purposes. This is because the different EEP computations would otherwise need to be parallelized to yield better performance. Thus in the case of array simulations, the implementation of new methods of computation that combine information non-locally to simultaneously speed up the calculation of all EEPs is an active area of research.

Chapter 2

Numerical electromagnetic modelling of antennas and its application on SKALA4.1

2.1 Frequency Domain methods

Within the framework of computational electromagetism, there is a multitude of methods, each of which is optimized for certain classes of problems. In low-frequency radioastronomical applications, the antenna properties of interest refer mostly to the far-field, e.g. embedded-element electric field response in an array environment, and extend to the scattering parameters as well as some other metrics relating to polarimetry (the Jones matrix and IXR [29], see Eq. (2.22)). Frequency-domain solvers are the dominant choice in such analyses, since the transient response is of no interest for the frequencies and timescales of data integration. Unlike telemetry applications, on the other hand, antennas used for radioastronomy need to resolve as many characteristics as possible in a detected signal so approximations for the receiving parts should be treated with caution, while the simulation meshes should capture fine details. We will focus our interest here on two such methods that are going to be employed throughout our simulations: The Method of Moments and the Characteristic Modes Analysis. Emphasis is also given to the network theory applied on receiving arrays, which uses such simulation outputs to further compute array quantities.

2.1.1 The Method of Moments (MoM) and its derivatives

The MoM is a general method that discretizes the problem of the current distribution on a manifold, given a certain excitation. The most common implementation is that of a distribution of currents on an arbitrary 2D surface S. The electric field scattering from a surface can be derived by imposing the boundary condition of the electric field tangential to the surface S being zero, $\hat{n} \times \left(\hat{n} \times \vec{E}\right) = 0$[1], and

---

[1] For any vector $\vec{E}$, the tangent-normal decomposition is written as the vector identity $\vec{E} = \hat{n} \times \left(\hat{n} \times \vec{E}\right) + (\hat{n} \cdot \vec{E})\hat{n}$

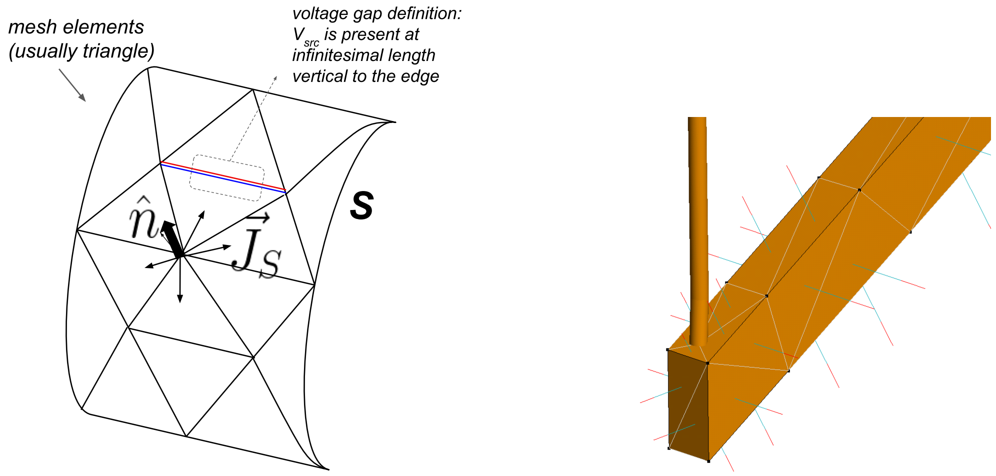

(a) **(b)**

Figure 2.1. (a): Schematic representation of an arbitrary surface S with the unitary normal $\hat{n}$ and the surface current $\vec{J}_S$ shown by arrows. Triangular MoM mesh elements, as well as an edge port is also drawn, (b): A FEKO MoM mesh including surface, wire and surface-wire junction elements; the unitary normal is also annotated here.

separating the source (src) and scattering (sct) components. If the scattering is expressed by means of the scalar and vector potentials, then one obtains:

$$\hat{n} \times \vec{E}_{src}(\vec{r}) = -\hat{n} \times \vec{E}_{sct}(\vec{r}) = -\hat{n} \times \left(j\omega\vec{A}(\vec{r}) + \nabla\Phi(\vec{r}) \right) \tag{2.1}$$

The potentials $\vec{A}$, Φ, given a certain surface distribution of currents and charge densities $\vec{J}_S$, Q_S, can exactly be solved by convolving with the 3D homogeneous Green function which is defined as $G(\vec{R}) = e^{jk|\vec{R}|}/(4\pi|\vec{R}|)$. Their expressions, when integrating the source region of point vector $\vec{r}'$ to a radiation region of point vector $\vec{r}$, are given as [30]:

$$\vec{A}(\vec{r}) = \iint_S \vec{J}_S(\vec{r}')G(|\vec{r} - \vec{r}'|)dS' \tag{2.2}$$

$$\Phi(\vec{r}) = \iint_S Q(\vec{r}')G(|\vec{r} - \vec{r}'|)dS' \tag{2.3}$$

where $k = \omega/c$ is the wavenumber and $c = 1/\sqrt{\mu\epsilon}$ the wave velocity in the homogeneous medium of dielectric ϵ and magnetic constant μ. The continuity equation is then used to combine the surface current density with the time-varied derivation of the charge density in the frequency domain, namely $\nabla \cdot \vec{J}_S(\vec{r}) = j\omega Q_S(\vec{r})$. This ensures that the total charge on the surface is conserved by the current flow it dynamically creates. When combined together with Eq. (2.3), (2.1), as well as using the definition of the wave impedance $\eta = \sqrt{\mu/\epsilon}$, one can derive [30]:

$$\hat{n} \times \vec{E}_{src}(\vec{r}) = \hat{n} \times \iint_S \left[jk\eta\vec{J}_S(\vec{r}')G(|\vec{r} - \vec{r}'|) + \frac{\eta}{jk}\nabla' \cdot \vec{J}_S(\vec{r}')\nabla' G(|\vec{r} - \vec{r}'|) \right] dS' \tag{2.4}$$

Taking the second cross-product and rendering it to a compact form using vector calculus, by defining the unit dyad $\boldsymbol{\mathcal{I}} = \hat{r}'\hat{r}'$ as well as the Green function dyad $\boldsymbol{\mathcal{G}}(\vec{r}, \vec{r}') = \left[\boldsymbol{\mathcal{I}} - \frac{1}{k^2}\nabla'\nabla'\right] G(|\vec{r} - \vec{r}'|)$, Eq. (2.4) can be written as:

$$\begin{aligned} \hat{n} \times \hat{n} \times \vec{E}_{src}(\vec{r}) &= \hat{n} \times \hat{n} \times \iint_S jk\eta \vec{J}_S(\vec{r}') \cdot \left[\boldsymbol{\mathcal{I}} - \frac{1}{k^2}\nabla'\nabla'\right] G(|\vec{r} - \vec{r}'|) dS' \\ &= \hat{n} \times \hat{n} \times \iint_S jk\eta \vec{J}_S(\vec{r}') \cdot \boldsymbol{\mathcal{G}}(\vec{r}, \vec{r}') dS' \end{aligned} \tag{2.5}$$

This is called the Electrical Field Integral Equation (EFIE) [30]. It is an integrodifferential equation that must be solved for $\vec{J}_S$, and in all practical cases, numerical techniques are used to discretize it. It is not the only such equation used in Method of Moments solvers: The Magnetic Field Integral Equation (MFIE) is also used in some implementations (especially closed geometries), while combinations of the two also help in overcoming numerical issues (CFIE, [31]). It is also well known [32] that the surface current $\vec{J}_S$ radiates an electric far-field which is computed as:

$$\vec{E}(r, \theta, \phi) = \frac{jk\eta e^{-jkr}}{4\pi r} \hat{r} \times \left(\hat{r} \times \iint_{S'} \vec{J}_S(\vec{r}') e^{jk\hat{r}\cdot\vec{r}'} dS'\right) \tag{2.6}$$

since this is the asymptotic expression of Eq. (2.5) in the Fraunhofer limit where $r \to \infty$ in a certain way for the phasor and inverse ("path loss") quantities of $|\vec{r} - \vec{r}'|$.

The surface integral is in the case of MoM calculated by discretizing the surface into a triangular mesh. A set of basis functions $\Psi = \left\{\vec{\psi}_i(\vec{r}),\ i \in \{1, \cdots, M\}\right\}$ is attributed to the discretized boundaries M of such a meshed geometry, while some test functions (optimally the same as the basis functions for most type of problems or Galerkin testing [33]) are used to create a square linear algebra problem. Fig. 2.1a summarizes in a schematic the meshed surface quantities featuring an edge port definition as a voltage gap source. We omit the details of the discretization procedure and provide the general formulas for the impedance matrix $\mathbf{Z}$ and the excitation vector $\bar{V}_{src}$ of the final equation $\mathbf{Z}\bar{J}_S = \bar{V}_{src}$:

$$Z_{ij} = jk\eta \iint_{S_i'} \iint_{S_j} \vec{\psi}_i(\vec{r}) \cdot [\hat{n}_i \times \hat{n}_i \times \boldsymbol{\mathcal{G}}](\vec{r}, \vec{r}') \cdot \vec{\psi}_j(\vec{r}') dS dS' \tag{2.7}$$

$$V_{src;i} = \iint_{S_i'} \vec{\psi}_i(\vec{r}') \cdot \left(\hat{n}_i \times \hat{n}_i \times \vec{E}_{src}(\vec{r}')\right) dS' \tag{2.8}$$

Here S_i', S_j denote the triangular surfaces of triangles i, j, the basis functions of which are interacting, while $[\hat{n}_i \times \hat{n}_i \times \boldsymbol{\mathcal{G}}]$ is a new operator which is the Green function dyad incorporating cross-products of the surface normals[2]. At this point, the tangential component is explicitly derived by the normal vector and is included in the derivation because the basis functions are arbitrary. In practice, the basis functions will mostly be defined as always tangential to the surface in case there is no conductive medium in each face and $\hat{n}_i$ would be included in the Green function

---

[2] e.g., see `eecs.umich.edu/courses/eecs730/lect/DyadicGF_W09_port.pdf` for dyad identities, where $\hat{n} \times \boldsymbol{\mathcal{G}} = (\hat{n} \times \hat{r}')\hat{r}' - \nabla'\nabla'\hat{n}\times$

derivation. If the system is solved with proper numerical matrix inversion techniques, then $\bar{J}_S = \mathbf{Z}^{-1}\bar{V}_{src}$ and the electric far-field can be approximated as:

$$\vec{E}(r,\theta,\phi) \approx \frac{jk\eta e^{-jkr}}{4\pi r}\hat{r}\times\left(\hat{r}\times\sum_{i=1}^{M}\iint_{S'_i} J_{S;i}\vec{\psi}_i(\vec{r}')e^{jk\hat{r}\cdot\vec{r}'}dS'\right) \tag{2.9}$$

The Basis Functions (BF) have to conform to some conditions in order to adequately represent an electromagnetic problem. They must not create line charges on the edges of triangles, so there has to be some definition that creates co-linear basis functions along edges or cancel the charges, having a zero total divergence, when they are summed. Such an implementation of basis functions are the Rao-Wilton-Glisson, or RWG [34]. These are attributed to the edges of the triangles and indeed cancel the charge on each edge by a dual definition of their unit vector on each of the two triangle faces in which the edge is contained. Their definition also ensures continuity of the normal current on the edge, which is the one actually "flowing" on the surface. The piece-wise linear (PWL) functions used in the early works of MoM in 1D geometry (on the Pocklington equation) are also special cases of the RWG where a basis function is attributed to each point between two wires, an equivalence that has been shown in [35]. The extension to Wire/Surface Junctions (W/SJ) has been presented in [36], where the current on each wire touching a surface is divided in all its adjacent triangles equally. Fig. 2.1b shows a real mesh by FEKO described by all of the aforementioned basis functions.

The Method of Moments is one of the most widely used and expanded numerical methods in Applied Electromagnetics [37]. A well-known extension is the Multi-Level Fast Multipole Algorithm (MLFMA), which uses multimode expansions of the green function for far-apart cross-element calculations [38]. The choice of BFs is also crucial to the size of any problem, and methods of reducing their number upon physics-based criteria exist. A wide category of those constitutes the Macro-Basis Function methods (MBFs), which have been described in various works, conveniently reviewed in [39]. The Characteristic Basis Function methods (CBFs) is one sub-category of those functions, firstly introduced in [40], in which BFs are constructed using geometrically separate sub-problems. The use of acceleration schemes such as Adaptive Cross-Approximation can also speed up calculations in conjuction with these BF expansions [41]. In general, many low-rank matrix-based, linear algebra techniques for acceleration exist as reviewed in [42].

Important advances have recently been made also for large array analysis, which is challenging due to the extremely large number of unknowns and in certain cases wide-band requirements, as with SKA-Low. The Domain Green's Function Method (DGFM) is itself a sub-domain method like CBFs but with further assumptions that evade some calculations. Recent work in this area of methods has also generalized the "infinite array" approach used by DGFM's by adding bias terms [43]. Both of these approaches have tested their results on aperiodic arrays of antennas similar to those of the SKA-Low. Many approaches, as in [44], commence their analysis by using the Isolated Element Pattern (IEP) and utilizing scattering formulations. It is also worth noticing that specifically in the context of SKA-Low, in which one station can result in up to 10^6 BF, some specialized methods have appeared. The HARP[45] method, which uses Harmonic Polynomials to interpolate between near-and far- field interactions of MBFs, controls the accuracy via a chosen Radius of Influence for the mutual coupling effects, while most recently a Fast Direct Solver has been developed with an error-controlled accuracy, amenable to the requirements set for EEPs [46].

2.1.2 Characteristic Modes Analysis (CMA)

The description of an electromagnetic problem in terms of characteristic modes has been an objective treated in the literature dating back even to the '60s, with the first work of Garbacz [47]. Later, a rigorous representation of the problem in terms of the MoM Z-matrix was introduced by Harrington [48], which marks the start of its use in numerical problems. The method has resurfaced in the last decade, as one of its principal advantages is the physical insight it can provide to various electromagnetic problems ([49]).

The method is stated as follows. Let us define an operator $\boldsymbol{\mathcal{Z}}_E$ such that:

$$\boldsymbol{\mathcal{Z}}_E(\vec{J}) := \hat{n} \times \hat{n} \times \iint_S jk\eta \vec{J}(\vec{r}') \cdot \boldsymbol{\mathcal{G}}(\vec{r}, \vec{r}') dS' \tag{2.10}$$

We drop the surface S index since we are only going to examine 2D geometries. Then the EFIE can just be written as: $\boldsymbol{\mathcal{Z}}_E(\vec{J}) = \hat{n} \times \hat{n} \times \vec{E}_{src}$. If $\boldsymbol{\mathcal{Z}}_E = \boldsymbol{\mathcal{R}}_E + j\boldsymbol{\mathcal{X}}_E$ are the real and imaginary parts of this operator, then instead of solving the excitation-dependent problem we first pose another, generalized eigenvalue problem which consists in requiring that the 2 operators $\boldsymbol{\mathcal{R}}_E$, $\boldsymbol{\mathcal{X}}_E$ are colinear for some subset of surface currents or that for some eigenvalues λ and eigenvectors $\vec{J}$ we can write:

$$\boldsymbol{\mathcal{X}}_E(\vec{J}) = \lambda \boldsymbol{\mathcal{R}}_E(\vec{J}) \Rightarrow \boldsymbol{\mathcal{Z}}_E(\vec{J}) = (1 + j\lambda)\boldsymbol{\mathcal{R}}_E(\vec{J}) \tag{2.11}$$

This problem can be solved with eigenvalue decomposition techniques (essentially, for invertible $\boldsymbol{\mathcal{R}}_E$ we have $[\boldsymbol{\mathcal{R}}_E^{-1}\boldsymbol{\mathcal{X}}_E - \lambda\boldsymbol{\mathcal{I}}](\vec{J}) = \vec{0})$. The result is a set of eigenvalues λ_n and eigenvectors $\vec{J}_n$, $n \in \{1, \cdots, N\}$, $N = \text{rank}(\boldsymbol{\mathcal{R}}_E^{-1}\boldsymbol{\mathcal{X}}_E)$. It is proven that for operators such as those originating from the EFIE, this set is complete with respect to the vector space of all currents $\vec{J}$. This means the following two conditions:

$$\iint_S \vec{J}_m^H(\vec{r}) \cdot \boldsymbol{\mathcal{Z}}_E\left(\vec{J}_n(\vec{r})\right) dS = (1 + j\lambda_n) P_{mm} \delta_{mn} \tag{2.12}$$

$$\forall\ \vec{J}\ \exists\ \bar{\alpha} = [\alpha_1, \ldots, \alpha_N] : \boldsymbol{\mathcal{Z}}_E(\vec{J}) = \sum_{n=1}^{N} \alpha_n \boldsymbol{\mathcal{Z}}_E(\vec{J}_n) \tag{2.13}$$

where $(\cdot)^H$ is the Hermitian operator (conjugate transpose), δ_{mn} is the Kronecker delta and P_{mm} is the real part of the left-hand-side integral of Eq. (2.12) (when it is non-zero i.e. $m = n$) and in the EFIE formulation represents a radiated power term that is due to eigencurrent $\vec{J}_m$. It can also be proven by introducing the excitation-dependent problem $\boldsymbol{\mathcal{Z}}_E(\vec{J}) = \hat{n} \times (\hat{n} \times \vec{E}_{src})$, that:

$$\alpha_n = \frac{\iint_S \vec{J}_n^H(\vec{r}) \cdot \left(\hat{n} \times (\hat{n} \times \vec{E}_{src})\right) dS}{(1 + j\lambda_n) P_{nn}} \tag{2.14}$$

It is important to note though that CMA can be applied in conjuction with many numerical methods [50]. In the case of a representation of $\boldsymbol{\mathcal{Z}}_E$ by a Method of Moments discretization as a $M \times M$ matrix $\mathbf{Z}$ and the eigencurrents as $M \times 1$ vectors $\bar{J}_n,\ n \in \{1, \cdots N\}$, the same relations apply in a matrix multiplication sense of the operator. In the asymptotic Fraunhofer limit expansion of $\boldsymbol{\mathcal{Z}}_E$, the electric far-field can be decomposed into characteristic far-fields as:

$$\vec{E}(r, \theta, \phi) = \sum_{n=1}^{N} \alpha_n \vec{E}_n(r, \theta, \phi) \tag{2.15}$$

where the $\vec{E}_n(r, \theta, \phi)$ are obtained by Eq. (2.9) substituting $\bar{J}$ by $\bar{J}_n$.

The coefficients α_n are called modal weighting coefficients (MWC). They are the product of modal significance $\mathrm{MS}_n = 1/(1 + j\lambda_n)$, which is excitation-independent and only has to do with the geometry of the structure, and the modal excitation coefficient $\mathrm{MEC}_n = \iint_S \vec{J}_n^H(\vec{r}) \cdot \left(\hat{n} \times (\hat{n} \times \vec{E}_{src})\right) dS/P_{nn}$, which measures how well the eigenecurrent $\vec{J}_n$ is excited by the source and is also a normalized quantity. An important aspect of CMA is the arrangement of the a_n solutions as functions of frequency f [50]. If we use for example the MoM discretization and attempt to calculate the eigenvalues of $\mathbf{Z}$ for a couple of frequencies $f_1,\ f_2$, their enumeration is not going to be consistent across different frequencies (that is, $a_1(f_1)$ does not map to $a_1(f_2)$). This is a numerical issue because the eigenvalue calculation does not keep track of any changes in the matrix entries, but assigns mode numbers in a self-consistent way. In order to re-arrange the modes in a way that makes physical sense, one has to employ extra algorithmic steps in the CMA implementation after the eigendecomposition. This is called tracking in the CMA literature.

Characteristic Modes Analysis can assist in reducing the complexity of antenna design, by means of highlighting the excitation-free, inherent geometric properties of an antenna, or reducing its scope to one mode orthogonal to all others. There are though some limitations to its application. Advanced eigenmode computation routines and tracking across frequency algorithms are of high computational complexity, scaling with the mode truncation order and the basis function size of the problem. Furthermore, convergence is easily achieved for far-field quantities for which the modal decomposition is complete, but near-field ones such as the reflection coefficient need “source-current" terms to compensate for the effects of travelling-wave evanescent modes (instead of only resonant, standing-wave modes) [51].

In array antenna systems, there are a number of CMA synergies for processing the mutual coupling between two or more antennas [52]. For an array of dipoles of arbitrary lengths, recent work examining their modes has connected the analytic methods with the CMA formulation [53][3]. Raines [54] has presented the treatment of a two-antenna system by block-partitioning the Z-matrix in 4 blocks (2 diagonal self-terms and 2 off-diagonal that describe the coupling), and applying the standard theory to its Schur complement, which characterizes the active antenna in presence of the passive one. Application of these techniques by element loading has been considered in [55, 56]. Ghosal [57] and Schab [58] have used the theory of coupled modes to

---

[3] This work can directly be extended to a single log-periodic antenna which is loaded by its boom; though arrays of such antennas have not appeared in the literature

directly partition the problem into uncoupled and coupled linear “subspaces”, aiming to understand the phenomenon from a more algebraic point of view. For finite arrays of a larger number of antennas, some of the current approaches are outlined in [59, 60], where a characteristic modes decomposition is attempted using the modes of a single element and either calculating modal coupling coefficients, or defining entire domain basis functions.

2.2 A quick introduction into the EEP network theory

The Embedded Element Patterns microwave network theory has consistently been summarized in [21, Ch. 5], based on works of previous authors. Importantly, a first representation of the array as multi-port network can be found in de-Hoop [61]. The main idea is that, in the same way that an antenna impedance can be defined for a single port, a multiport impedance matrix can also been defined for many antennas. Let us represent the antenna receiving system as a set of N such ports, as can be seen in Fig. 2.2. According to the Thevenin theorem, if $\bar{I}$ are the excitation currents and $\bar{V}_{oc}$ the open-circuit induced voltages, then the fundamental network relation computes the antenna port voltages as [21]:

$$\bar{V} = \bar{V}_{oc} + \mathbf{Z}_{ant}\bar{I} \tag{2.16}$$

If on these antenna ports (or terminals) an N-port load $\mathbf{Z}_L$ is connected, then $\bar{V} = -\mathbf{Z}_L\bar{I}$ (the current is now ingoing rather than outgoing). Combining this with Eq. (2.16), The antenna voltages and currents can be calculated as:

$$\bar{V} = \mathbf{Z}_L(\mathbf{Z}_{ant} + \mathbf{Z}_L)^{-1}\bar{V}_{oc}, \; \bar{I} = -(\mathbf{Z}_{ant} + \mathbf{Z}_L)^{-1}\bar{V}_{oc} \tag{2.17}$$

According to the analysis of [61], which exploits the reciprocity theorem, the open-circuit voltages can be expressed as:

$$\bar{V}_{oc} = \frac{4\pi}{j\eta k I_0}\mathbf{e}_{oc}\vec{E}_{src} \tag{2.18}$$

where $\mathbf{e}_{oc} = [\vec{e}^{\,T}_{oc,1} \cdots \vec{e}^{\,T}_{oc,N}]^T$ is the $N \times 2$ matrix collection of all the normalized[4] Embdedded Element Patterns at an open-circuit condition, when excited with a current I_0, and $\vec{E}_{src} = [E_{src;\theta} \; E_{src;\phi}]^T$ the excitation dual polarized far-field. The $\mathbf{e}_{oc}$ are exactly the far-field patterns one can obtain by simulation of the array with a constant current source I_0 using any convenient method. The subscript indicates the active element, while all the others are passive. We can therefore see that the antenna terminal voltages are a linear combination of the EEPs, and together with the antenna matrix $\mathbf{Z}_{ant}$ fully describe the N-antenna network.

Furthermore, to calculate the directivity (or gain) of an array, the same framework applies by considering a source impedance $\mathbf{Z}_s$ instead of a load. For example, if one excites the array with currents $\bar{I}$, then the total electric far-field pattern of the antenna in transmit mode can be expressed in terms of open-circuit (oc) and short-circuit (sc) EEPs as:

---

[4] Normalization here means removal of the radial dependency $1/r$ and the phase delay e^{-jkr}

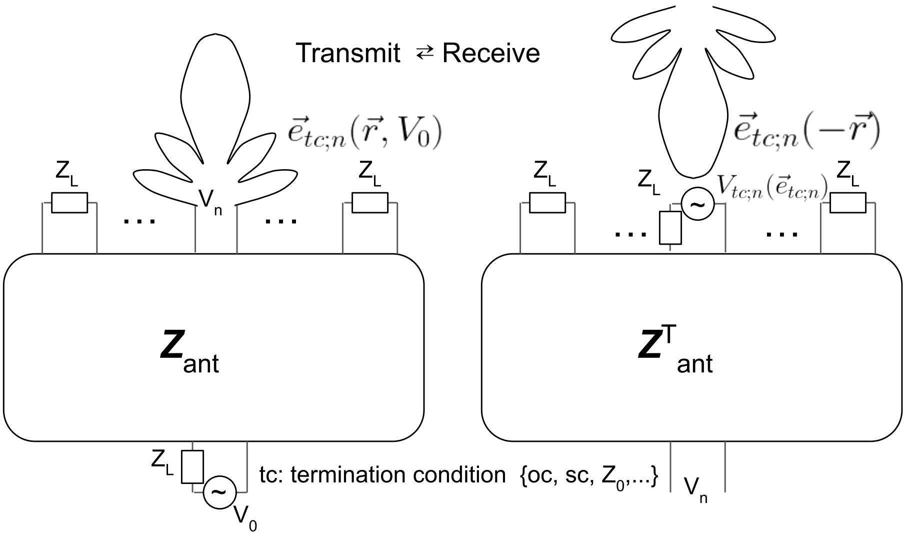

Figure 2.2. A schematic representation of an array of antennas as a N-port network, where one element is excited. The Thevenin representation is used with a Z_L source and load impedance to prescribe the desired termination condition, while the equivalence between transmit and receive mode is also described.

$$\vec{E} = \sum_{n=1}^{N} \frac{I_n}{I_0} \vec{E}_{oc,n} = \sum_{n=1}^{N} \frac{[\mathbf{Z}_{ant}\bar{I}]_n}{[\mathbf{Z}_{ant}\bar{I}_{0,n}]_n} \vec{E}_{sc,n} \tag{2.19}$$

where $\bar{I}_{0,n} = [0 \cdots I_0 \cdots 0]^T$ with an entry only at the n-th position (such that, eventually, $[\mathbf{Z}_{ant}\bar{I}_{0,n}]_n = Z_{ant;nn}I_0$). Other representations also exist for the dual case of a Norton circuit, when the load (or source) is expressed as an admittance matrix $\mathbf{Y}_L$ (or $\mathbf{Y}_s$). If a voltage V_0 is used as excitation in simulations, then the above total field can be computed with voltage weights $\bar{V}$ as:

$$\vec{E} = \sum_{n=1}^{N} \frac{V_n}{V_0} \vec{E}_{sc,n} = \sum_{n=1}^{N} \frac{[\mathbf{Y}_{ant}\bar{V}]_n}{[\mathbf{Y}_{ant}\bar{V}_{0,n}]_n} \vec{E}_{oc,n} \tag{2.20}$$

where $\bar{V}_{0,n} = [0 \cdots V_0 \cdots 0]^T$ with an entry only at the n-th position (and as before, $[\mathbf{Y}_{ant}\bar{V}_{0,n}]_n = Y_{ant;nn}V_0$). One can find extensive transformations between the various representations in the general case of Z_g, Y_g EEPs in [62].

2.3 The case of SKALA4.1

This section contains a review of the results of electromagnetic simulations of the SKALA4.1 antenna as they have been reported in [63, 9]. We emphasize on:

- the far-field pattern co-polarized to the excited polarization

Table 2.1. Comparison of meshing parameters using the FEKO and Galileo software (basis function types are described in Sec. 2.1.1

#BF	2D-RWG	1D-PWL	W/SJ	Total
FEKO	7471	934	84	8489
Galileo	8044	670	84	8798

- the S-parameters of the antenna as a 2-port system of the X and Y polarizations
- the IXR which quantifies the cross-polarization of the far-field pattern [29].

2.3.1 Method of Moments: FEKO and Galileo simulations

Two models have principally been used in the EM community of SKA-Low for simulations of SKALA4.1. The one which has been integrated in FEKO has extensively been described in [64], where a number of simplifications have been made in order to minimize the size without compromising the electromagnetic performance. The second one has been integrated in Galileo starting from the mechanical CAD model and has been described in [65]. Both FEKO[5] and Galileo[6] are EM simulation suites based on the Method of Moments, and have various implementation options that adhere to any specific problem (such as low-frequency optimization). The meshing has been deemed necessary to be uniform throughout the full frequency band of SKA-Low to avoid numerical issues. The EM models as meshed are jointly seen in Fig. 2.3, where a zoom into the voltage-gap port is also indented, while the resulting mesh sizes are analytically compared in Tab. 2.1.

We are first going to compare the far-field co-polar gain patterns for both polarizations of SKALA4.1, and by means of both solvers. The gain pattern does not depend on the excitation scheme, but it is useful to note that a constant voltage-gap excitation source is used[7]. Fig. 2.4 presents a comparison between the frequency response of the gain (in dBi) at zenith direction ($\theta = \phi = 0°$) computed using FEKO (solid curves) and Galileo (dashed curves), when exciting the X-polarized (blue) and Y-polarized (red) dipoles of SKALA4.1. The co-polar far-field is computed according to the Ludwig-III definition [66]:

$$E_{co}(r,\theta,\phi) = E_\theta(r,\theta,\phi)\sin(\phi) + E_\phi(r,\theta,\phi)\cos(\phi) \tag{2.21}$$

We note that both polarizations have a very similar co-polar pattern, while the two solvers agree at a very good level in the gain response. The zenith direction corresponds to maximum gain, which is centered around 7.8 dBi for SKALA4.1. There are also some important features of this pattern worth pointing out:

1. The presence of a ground plane, simulated as an infinite Perfect Electric Conductor (PEC), is responsible for the slow ripple of ≈ 1 dB in amplitude

---

[5] `https://altairhyperworks.com/feko/`

[6] `https://www.idscorporation.com/pf/galileo-suite/`

[7] While FEKO uses a port definition without a source impedance, Galileo incorporates this in its own definition. This will affect the electric field result, but both results can easily be streamlined in one preferred definition according to the operations of Sec. 2.2 for the one dimensional case.

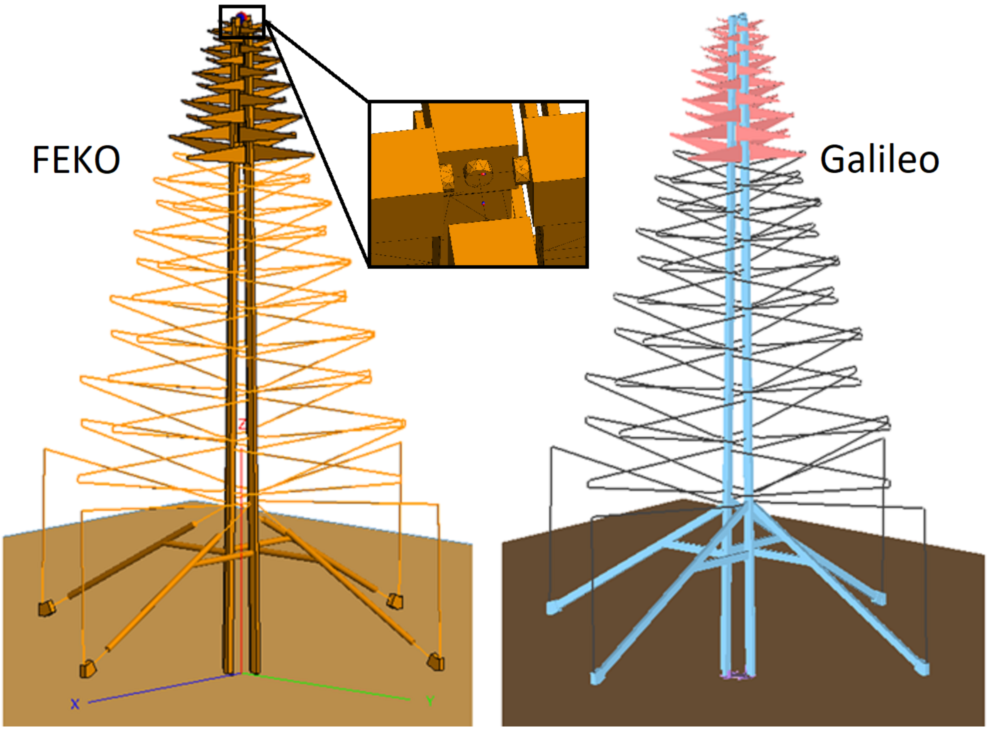

Figure 2.3. FEKO and Galileo electromagnetic models of SKALA4.1, as meshed in the respective CAD environments. A zoom into the top structure of SKALA4.1 is also seen, with a voltage gap port defined (approximation of the real, coaxial cable port).

and 75 MHz in repeating cycle. This reflection is not a worrying systematic effec; further analysis on diffraction effects is conducted in Ch. 4.

2. Some narrow-band anomalies are visible at specific frequencies, that are confirmed for both polarizations with both solvers. This is an intrinsic feature of the antenna and is addressed in Ch. 3.

Next we examine the frequency response of the scattering parameters for each polarization. Again the $|S_{XX}|^2$, $|S_{YY}|^2$ are compared (in dB) as calculated by both software in Fig. 2.5. We can conclude that both solvers calculate both parameters with high accuracy, while the X-polarized port is slightly better matched at 50 Ω than the Y-polarized (geometrically, X is placed lower in height from the ground than Y). The antenna is not well matched in the lower frequencies, due to the presence of the bow-tie dipole which extends the bandwidth but cannot achieve acute resonances. This aspect is also discussed in [9].

To test the effectiveness of SKALA4.1 in discriminating the two orthogonal polarizations, we can resort to the complementary Ludwig-III definition of cross-polarization, but this is a coordinate-system dependent metric[8]. In recent studies, the IXR is the preferred figure of merit; it measures the intrinsic crosspolarization of the system independent of the coordinate system, and for any polarimetric system described by Jones matrix $\mathbf{J}$ it is defined as [29]:

---

[8] The Ludwig-III cross-polar electric far-field is presented in Sec. 2.3.2 in comparison with CMA

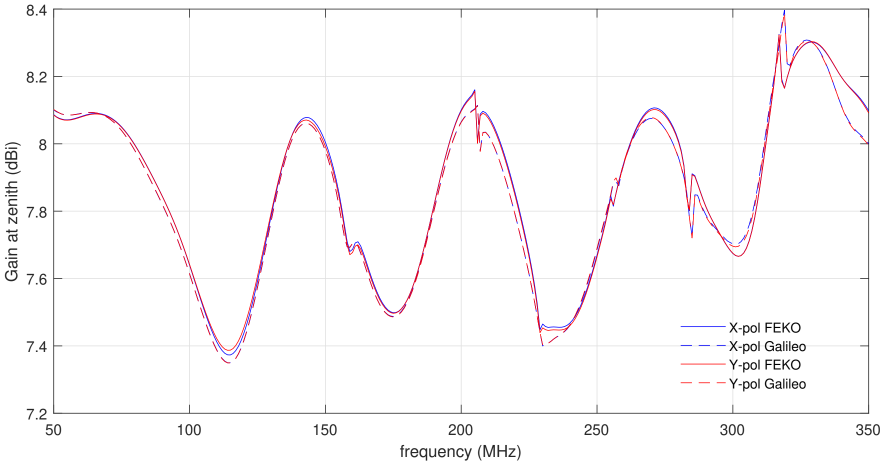

Figure 2.4. Co-polarized Ludwig-III gain in dBi at zenith ($\theta = \phi = 0°$) over the full frequency band of SKA-Low, both for a X- and Y-polarization excited SKALA4.1, using the EM software FEKO and Galileo.

$$\mathrm{IXR}_{\mathbf{J}} = \left(\frac{\sigma_{max}(\mathbf{J}^H\mathbf{J}) + \sigma_{min}(\mathbf{J}^H\mathbf{J})}{\sigma_{max}(\mathbf{J}^H\mathbf{J}) - \sigma_{min}(\mathbf{J}^H\mathbf{J})} \right)^2 \tag{2.22}$$

Here σ_{max}, σ_{min} are the maximum and minimum eigenvalues of the $\mathbf{J}^H\mathbf{J}$ matrix, which is hermitian and thus always results in real positive eigenvalues. In our case when using spherical coordinates, the Jones matrix can be described as $\mathbf{J} = [\vec{E}_X^T;\ \vec{E}_Y^T]$, where each row is the $\hat{\theta}$ and $\hat{\phi}$ components of the relevant excited port of the antenna (X or Y) [67]. Fig. 2.6a presents the minimum IXR calculated using the FEKO and Galileo simulated patterns. It should be noted here that a transformation of the FEKO patterns to agree with those of Galileo in their port definition (including the source impedance) has to be performed. The resulting curves agree with each other at a very good level and both respect the thresholds that have been stated in [63] for not majorly compromising the scientific impact of SKA-Low, being >12 dB in the 50-250 MHz band and >11 dB towards the higher end (note that these thresholds differ than their counterpart calculations in Ludwig-III terms). All the minimums are eventually reached at the edge of the chosen field of view, that is $\Omega = \{0 \leq \theta \leq 45°\}$. Finally, we also present a figure of the port cross-coupling $|S_{12}|^2 = |S_{21}|^2$, in Fig. 2.6b. The very low level of interaction of the two antenna ports means that we can usually ignore crosstalk from orthogonal ports when beamforming. The agreement now between the two solvers is less clear, which points to their limit in representing the sensitive, low-amplitude phenomena of the antenna. In both these plots, lower IXR (or higher $|S_{XY}|$) in higher frequencies mean that the solid dipoles of orthogonal polarizations are more coupled than the wire ones.

Some more investigations have recently been made in the phase response of the co-polar electric far-field pattern, which supplement these results and are useful in the beamforming of the array [68].

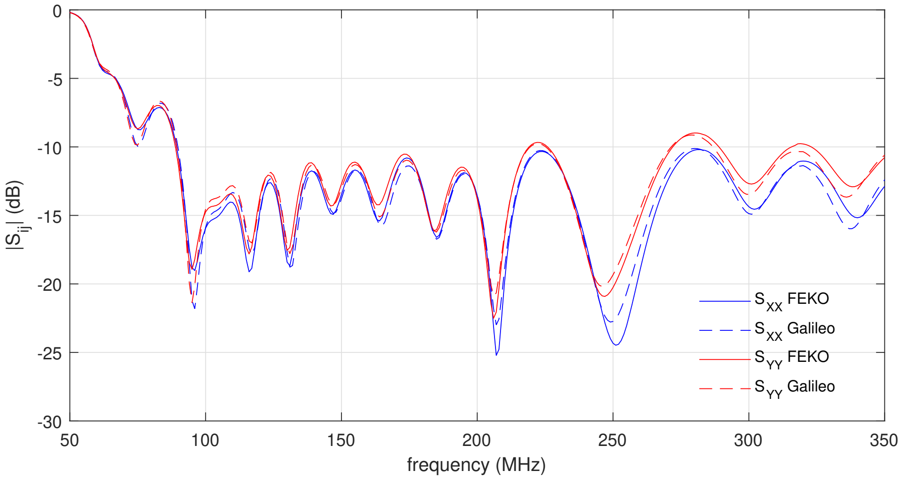

Figure 2.5. S-parameter power amplitudes in dB for the 2 polarizations of SKALA4.1 (XX, YY), computed with FEKO and Galileo software.

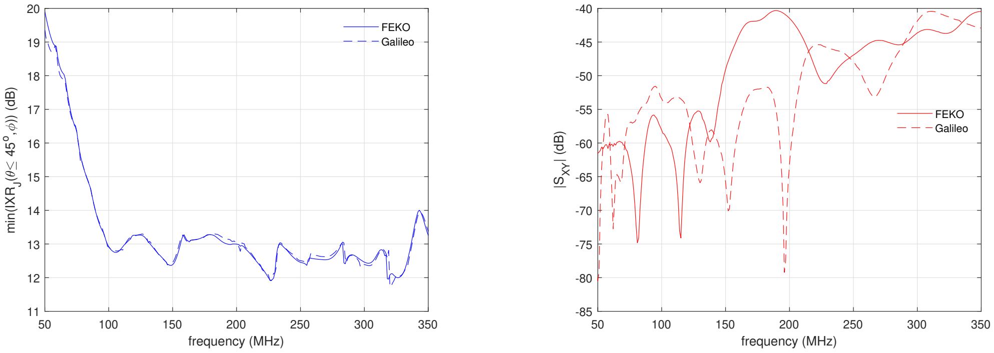

(a) **(b)**

Figure 2.6. Left: minimum IXR of SKALA4.1 in the full frequency range of SKA-Low, calculated in the Field of View limited at $\theta \leq 45°$ using both FEKO and Galileo, Right: $|S_{XY}|$ in dB in the same frequency range between the two ports of SKALA4.1 using both solvers.

2.3.2 Characteristic Modes: FEKO simulations

In this section, we will focus our analysis in the frequency range 50-100 MHz. This is a critical region for the scientific objectives of SKA-Low, since the Cosmic Dawn science is expected to be conducted there [69]. It is also important to note for the CMA that the solution is dependent on the mesh quality, as well as its size. Both allow for better convergence, as well as for better tracking. The size of a single antenna with some refinements has been augmented to a total of 15100 BF, which is almost double that of Tab 2.1. This size is challenging for experimentation with a method less tested with such problems, and we aim to analyse the results in comparison with the MoM derived ones to further test their accuracy.

We excite the SKALA4.1 antenna at its X-polarized dipoles (as in Fig. 2.3)

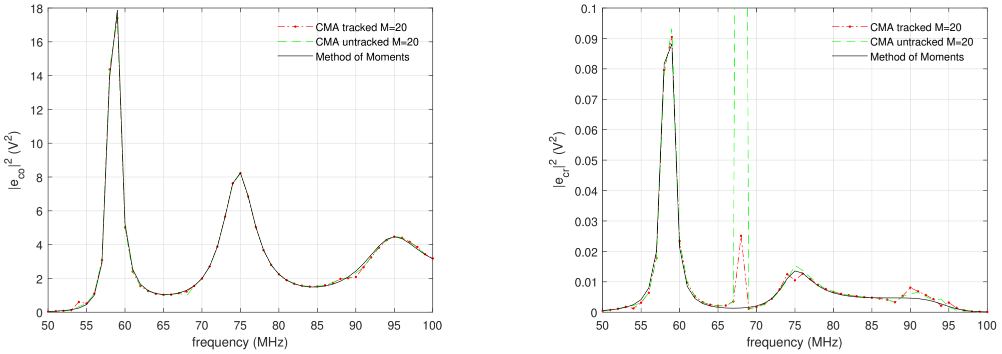

(a) **(b)**

Figure 2.7. (a) Square modulus of the co-polarized, normalized electric far-field values at zenith across frequency, using MoM and CMA with $M = 20$ modes. Even without the tracking routine, the CMA solution converges to that of the MoM, (b) The same quantity for the cross-polarized component.

with a constant voltage of $V_s = 1\ V$, and use a number of $M = 20$ modes for the approximation of the solution, heuristically chosen the same as the number of dipoles per polarization of the antenna. The frequency step is 1 MHz. In Fig. 2.7a, we present a comparison of the squared modulus of the co-polarized, normalized (with respect to radial dependence $1/r$) electric far-field values, $|e_{co}|^2 = r^2|E_{co}|^2$ (or far-field intensity), at zenith, computed using both the MoM and CMA solvers. Complementary to that, in Fig. 2.7b the normalized cross-polarized component $|e_{cr}|^2 = r^2|E_{cr}|^2$ is presented, which derives from the Ludwig-III definition as [66]:

$$E_{cr}(r,\theta,\phi) = E_\theta(r,\theta,\phi)\cos(\phi) - E_\phi(r,\theta,\phi)\sin(\phi) \tag{2.23}$$

We present both the tracked and the untracked solution. For the tracked one, FEKO's own tracking algorithm was used, which implies that the search-space extends in further than the first M modes numerically calculated, until such modes are found that satisfy the tracking criteria, which would in turn necessitate comparisons with modes of adjacent frequencies. On the other hand, for the untracked solution we bypass this algorithm by running each frequency separately and saving only the first M modes. It is seen that this number of modes can succeed in converging to the MoM without tracking, while both $|e_{co}|^2$ solutions generally converge, with a number of small anomalies (see green curve in Fig. 2.7a) at 54, 68 and 90 MHz. The regions around 59, 75 and 95 MHz contain the peaks of the antenna radiation in this range, also observed as $|S_{XX}|$ local minima in Fig. 2.5. Such peaks are directly related to dipole modes, namely the radiation resonances of the bow-tie dipole and dipole 19, the next one on the $+z$ axis, at frequencies 59 and 95 MHz respectively. In the $|e_{cr}|^2$ solutions, some more anomalies are present at 75 MHz and, more pronounced, at 68 MHz. In that case, it can be concluded that numerical issues in the eigen-decomposition prevent the solution from converging to the low value expected by MoM (<0.002).

An important step in CMA is the eigenmode tracking across frequency, that is necessary to avoid confusion of the physical properties of each mode. As has already been described, we expect continuity of the eigenmode as a function of frequency that the CMA tracking algorithm should ensure. We present the tracking across frequency of the three most significant modes in terms of their MWC. In Fig. 2.8a, we have identified modes $m = 3,\ m = 7$ and $m = 9$ (as labelled by FEKO) as those responsible for the radiation peaks reported. Some tracking issues have appeared in the examined frequency range for less significant modes, a motive for which we lower-thresholded the y-axis of Fig. 2.8a at 0.03; they will though not affect our analysis as long as a constant mode ordering has been chosen for the frequencies across which the solution is properly modally tracked.

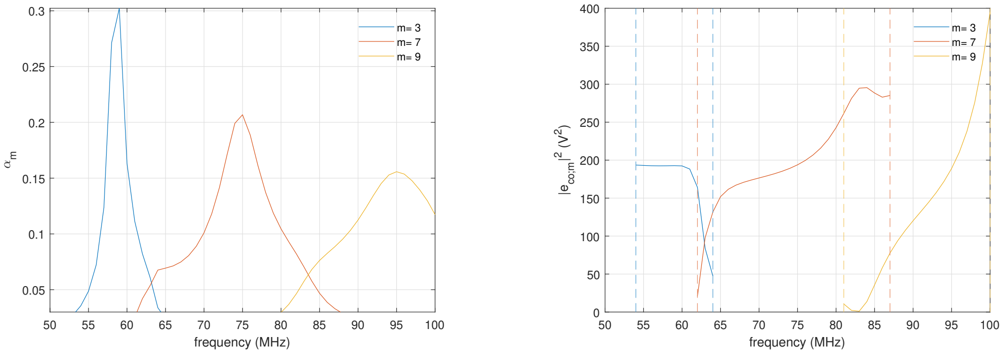

(a) (b)

Figure 2.8. (a) Tracking of the MWC's α_m across frequency of the three most significant modes, thresholded at 0.03. Two of them ($m = 3,\ m = 9$) directly associated to the dipole resonances at the respective peak of their α_m, (b) $|e_{co;m}|^2$ values for these modes, in the frequency ranges where the respective MWC is above the threshold.

In Fig. 2.8b, furthermore, the respective $|e_{co;m}|^2$ values are shown for each of the tracked MWC's, in the frequency range where each of them is above the set threshold (denoted by dashed vertical lines). We note that, at the 3 peaks identified, the modal value of the normalized electric field does not present some maximum; the dominant MWC is eventually determining the quality factor of the antenna resonance. The frequency response of those $|e_{co;m}|^2$ values though presents interesting, saddle-point like features around those peak frequencies.

Another noteworthy characteristic of the tracked modes are the crossings between them, meaning that at certain frequencies, some eigenvalues appear with multiplicity greater than one. According to [70, 71], this is an allowed feature of antennas belonging to certain symmetry groups (SKALA4.1 is symmetric with respect to a 180° rotation), while it can also serve as an evaluation of the tracking algorithm. It should also be clarified that this refers to the Modal Significance (MS), which is a characteristic of the impedance matrix independent of the excitation placement. We do not show MS but it has been verified to have the same trend and crossings.

2.3.3 A Transmission-Line loaded Dipole-Array approach

In this section, we will provide a description of SKALA4.1 using lighter MoM simulations of the antenna without its boom, which will be approximated as a perfect, non-radiating transmission line (TL). For that purpose, the remaining dipole array has to be fully characterized in terms of its dipole element EEPs and S-parameters as in Sec. 2.2. This approach is not novel in the literature, e.g. [72], although to the writer's best knowledge it has not been extensively explored with respect to its accuracy as is done here. Its usefulness is not the direct use of such results in view of their lighter simulation times, but rather the parametrization of our model for obtaining specific patterns such as when an interpolation between frequencies or spherical angle is desired. Furthermore, one can experiment by further loading the available ports of that representation with lumped elements without the need for more time consuming simulations, in order to obtain rough results of such practice (as has also been done in the following chapters). The use of a goal function in order to minimize the error between our approach and the full-wave one will be used for that purpose, in order to find the optimal parameters.

In Fig. 2.9, a network model of the dipole array matrix $\mathbf{Z}_{ant}$ is shown, interconnected with the transmission line segments of characteristic impedances and lengths $Z_{0;n},\ l_n$ respectively, for $n \in \{1, \cdots, 20\}$. The FEKO model of the dipole array, which will be used for the simulations, is presented in Fig. 2.9. The dipoles have a middle-wire connecting their two arms, while the last part of the boom connecting to the ground is considered part of the full wave problem of the 20-th dipole (bow-tie). This representation means that our voltages and currents on each dipole are not free to choose as in Sec. 2.2 but uniquely determined by the transmission line model "loading" the dipole array.

Twenty full-wave simulations have been computed by exciting each dipole separately, while all others are passively terminated at short-circuit, thus collecting all the $\vec{E}_{sc,n},\ n \in \{1, \cdots, 20\}$. As is seen in Fig. 2.9, we implement the interconnection between dipole n and the $(n-1)$-th TL segment output port, n-th TL input port as a junction where we apply the condition $I_{out;n-1} = I_n + I_{in;n}$. The voltages on this junction are equal ($V_{out;n-1} = V_n = V_{in;n}$), while we use the transmission line equations for the n-th segment:

$$\begin{aligned} V_{out;n} &= \cos{(kl_n)} V_{in;n} - jZ_{0;n} \sin{(kl_n)} I_{in;n} \\ I_{out;n} &= -j/Z_{0;n} \sin{(kl_n)} V_{in;n} + \cos{(kl_n)} I_{in;n} \end{aligned} \tag{2.24}$$

Here we have parametrized the transmission line characteristic impedance of the boom as $Z_{0;n}$, which allows for 20 of degrees of freedom in its representation of the guided wave, while its length l_n is the physical distance between the consecutive dipoles $n-1,\ n$. Passivity of this part of the model is still maintained, while the Z_0 as a function of the transmission line height from the ground should be smoother in the middle of the boom and more volatile at its ends. Finally, the simulated 20×20 $\mathbf{Z}_{ant}$ matrix accounts for the mutual coupling phenomena, since $\bar{V} = \mathbf{Z}_{ant}\bar{I}$.

Since we are using short-circuit EEPs with a voltage source of $V_0 = 1$ V, the total electric far-field pattern at direction is computed from Eq. (2.20) as $\vec{E} = \sum_{n=1}^{20} V_n \vec{E}_{sc,n}$. The reflection coefficient is a simple transformation of $S_{11} =$

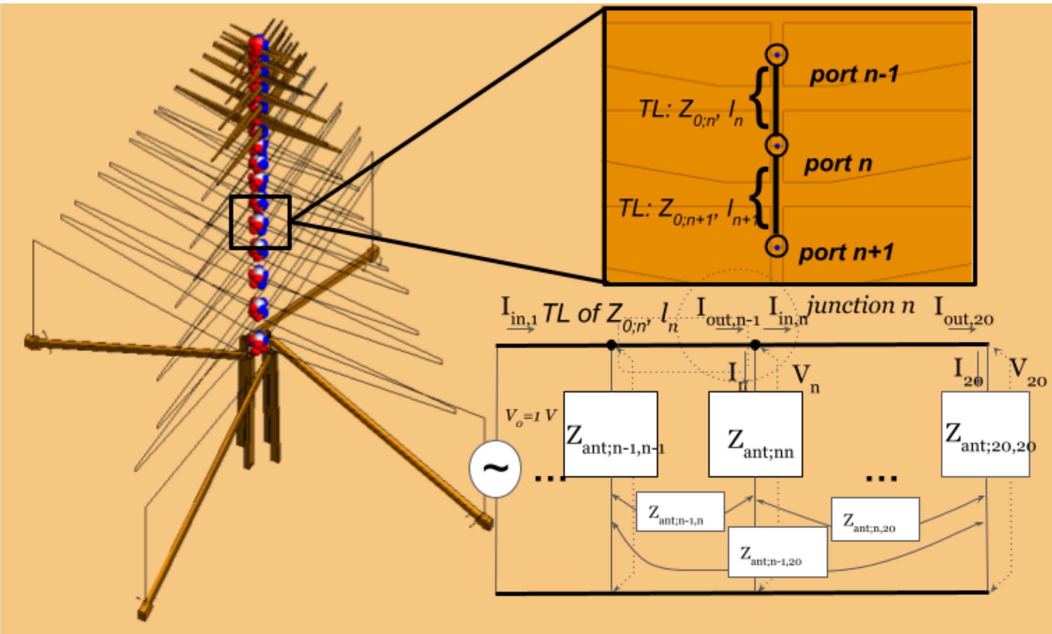

Figure 2.9. The FEKO electromagnetic model for SKALA4.1 without its boom, where ports have been assigned to each dipole in order to calculate the $\vec{E}_{sc;n}$, $\mathbf{Z}_{ant}$. A detail of the dipole progression can be seen, as well as a network model of the transmission-line loaded dipole array representing SKALA4.1. The matrix entries used are in the case of self-impedances real circuit connections, while in the case of mutual impedances they just represent the interaction and are properly handled in the full matrix equation.

$(Z_{11} - Z_0)/(Z_{11} + Z_0)$ where $Z_{11} = V_0/I_{in;1}$. We try to include both of these results in our goal function, since they both play a role in the antenna gain which is more representative of the antenna performance in the far-field $(4\pi/(2\eta)(|e_\theta|^2 + |e_\phi|^2) = P_{iso}$ on the nominator and $V_0^2/2\Re\{Z_{11}^{-1}\} = P_{rad}$ in the denominator). The reason why we do not directly try to optimize the fraction of these two quantities is because the various optimization techniques could converge on irrational values for the two quantities (with respect to our knowledge of such quantities from MoM simulations), while still maintaining the fraction at the designated goal, a solution which would clearly be unacceptable. It was further attempted to optimize with respect to gain and either P_{iso} or P_{rad}, but this would necessitate attributing weights (since they are not comparable quantities), which further complicates the problem.

Our investigation was first done by defining a goal function in order to minimize the frequency response at zenith (we have dropped the f, θ, ϕ dependencies on the above expressions for brevity). Our goal function in this case is expressed as:

$$F(\bar{Z}_0) = \|[\bar{P}_{iso}(\bar{Z}_0); \bar{P}_{rad}(\bar{Z}_0)] - [\bar{P}_{iso;fw}; \bar{P}_{rad;fw}]\|^2 \tag{2.25}$$

where the bar quantities mean a vector stacking along frequency points, and the subscript fw denotes the MoM, full-wave solution of the same quantity. The implementation of the network model with the equations given above, was scripted in a parametrized MATLAB function, that was then used for optimization. We have used the `fmincon` optimization routine in order to obtain the $Z_{0;n}$, $n \in \{1, \cdots, 20\}$

as a minimum of $F(\bar{Z}_0)$. The initial values that were given to the optimizing routine are $Z_{0;n} = 130\ \Omega$ for all n, and correspond (approximately) to the characteristic impedance value of the cross-section of the SKALA4.1 boom, as if it was an infinite TL. Two simulations of a very long such TL were conducted in oc and sc termination to estimate this value, using the formula $Z_0 = \sqrt{Z_{in;oc}Z_{in;sc}}$.

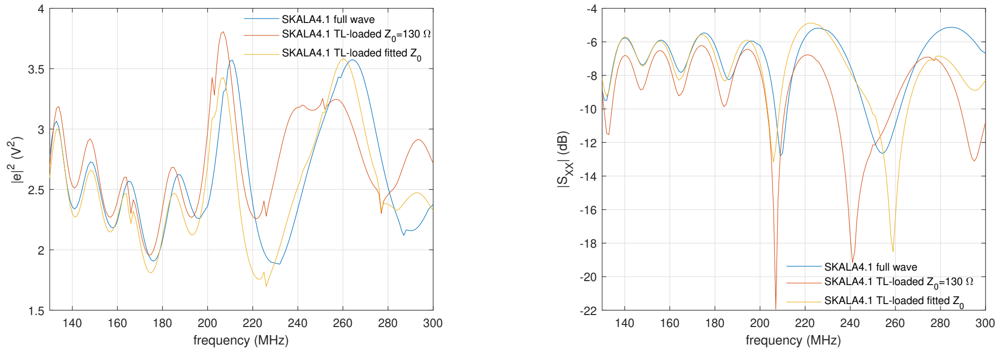

(a) **(b)**

Figure 2.10. (a): $|e|^2$ in V^2 for the case of TL segments of $Z_0 = 130\ \Omega$ and that of fitted values of $\bar{Z}_0$ by minimizing Eq. (2.25). The full-wave MoM solution is also plotted for comparison, (b): $|S_{XX}|$ in dB for the same cases as in (a).

The problem `fmincon` solves is of course non-linear and overdetermined, if we choose more than 20 frequency points. In order not to lose accuracy by fitting excessively many points with just 20 parameters, we have chosen a frequency range from 130 MHz to 300 MHz, avoiding the extremes of the band. In Fig. 2.10a we first present the $|e|^2$ response for the cases of the full-wave MoM solution, the response when the initial value 130 Ω is given to all TL segments as well as that of the fitted $\bar{Z}_0$. The same cases are examined in Fig. 2.10b for the $|S_{XX}|$. We can see that whereas the solution for ideal, constant Z_0 starts to diverge at around 200 MHz from the MoM solution, the optimized Z_0 values better recreate the resonant behaviour of the antenna both in terms of $|e|^2$ and $|S_{XX}|$ even up to 280 MHz. This means that the segmentation and Z_0 parametrization of the boom as TL is able, at least in half the frequency range of SKA-Low, to physically predict some of its parameters given the EEP and S-parameter response of the dipoles.

Finally, in Fig. 2.11a the gain is plotted for the three cases described above. Here the flexibility of the model is limited as it is only slightly different from that of the constant $Z_0 = 130\ \Omega$. This is due to the fact that we have not requested it directly in this optimization, as was explained before, but also due to the middle-wire feeding approach dictating the antenna resonances rather than the boom characteristic impedance. The optimal Z_0 values are shown in Fig. 2.11b and they are seen to oscillate more on the top of the antenna rather than at the bottom, close to the initial value of 130 Ω. There is no clear trend (e.g. a polynomial one), which means that the solution could also be improved with other optimization techniques adding extra constraints (here we only required that the values be positive). Other, relative-error goal functions might also be of interest for further experimentation.

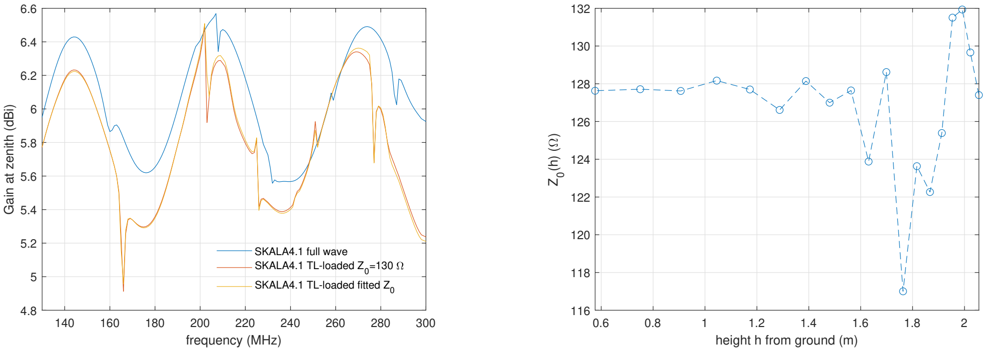

(a) **(b)**

Figure 2.11. (a): Gain at zenith (in dBi) for the case of TL segments of $Z_0 = 130\ \Omega$ and that of fitted values of $\bar{Z}_0$ by minimizing Eq. (2.25). The full-wave MoM solution is also plotted for comparison, (b): Z_0 of TL segments as a function of their height from the ground; the highlighted points correspond to segment 1 through 20 in reverse order.

Chapter 3

Spectral smoothness of SKALA4.1: higher frequency *“glitches"*

In this chapter, we will treat the problem of spurious radiation in Log-Periodic Dipole Antennas (LPDAs) [73] as well as a new technique of loading the antenna dipoles to dissipate the second order mode power on a resistor appropriately chosen as part of an RLC parallel circuit. The SKALA4.1 antenna performance will be examined both in terms of simulation and experimental measurement, but the concept is generalized for all similar antennas, i.e., log-periodic dipole antennas with non straight-wire dipoles. Despite the fact that SKALA4.1 has surpassed all major evaluation criteria, the problem of narrow gain discontinuities (or so-called glitches) has persisted, and this was the starting point of our present analysis.

The problem of narrow-band glitches, although minor for other applications, could potentially sever the narrow-band astronomical observations conducted with the SKA-Low [69]. Confident signal detection in radioastronomy requires a high degree of spectral purity, since the sought-out signals are weak. In the case of spectral lines (highly redshifted molecular or recombination lines, for meter wavelengths where SKA-Low will operate), acute features such as those we examine mimic them in the data. Furthermore, polynomial fitting and extraction techniques that work well in slowly varying instrumental anomalies cannot be applied in such narrow frequency bands, since they would also dampen the useful signal. The need for antenna hardware solutions, therefore, emerges for such problematic features.

While it is certainly desired, after the latest SKA Critical Design Review, to propose minimal changes to this antenna, a technique that does not set decisive constraints in an initial design process, rather corrects such spurious behaviour of LPDAs at a post-design phase, is not present in the current literature. Our method here mainly answers to the challenging scientific requirements of a complex project such as the SKA-Low. Due to its low-cost and post-design implementation, though, it is also an attractive method for other applications such as remote sensing.

3.1 Spurious LPDA characteristics and RLC loading

The problem of spurious radiation in this type of antennas has been described by some authors, citing mostly asymmetry concerns [74] as well as the finiteness of the structure and the associated termination [75, 73]. In most types of applications, though, such problems did not cause significant degradation of the performance, as their impact was mostly tackled by choosing a high input impedance [76].

As far as SKALA4.1 is concerned, we are looking into a different spurious radiation phenomenon, which has been hinted at by [73], and does typically appear in non-straight dipole elements; it originates from second order modes of these dipoles, which are undesired for the performance of the antenna. The active region of an LPDA where dipoles are excited with their primary mode (dipole length $l \approx \lambda/2$) is not perfectly matched to the feeding line impedance, while there are also dipoles in the operating frequency range for which the condition of length approaching λ occurs. Power leaks in the non-active regions being reflected back from the primary-mode excited active dipoles, and excites this secondary mode ($l \approx \lambda$) after propagating further down the boom to the longer dipoles, creating a second active region. For a SKALA4.1 antenna, this problem has been described and experimentally measured in [77]. In general, non straight-wire dipoles do not have the boundary condition of zero current at their edge, and their second order mode can have non-zero value at their middle. This mode can therefore be excited with a middle-placed port, which would not be possible for straight-wire dipoles (see also Fig. 3.2b).

It should be noted that, many other techniques already proposed in literature, such as the choice of different length to radius ratios l_n/a_n, a variable boom characteristic impedance Z_0 or dipole separation d_n[78, 75] have been proven insufficient or limited by more prioritized specifications in our examined antenna. For example, even though the input impedance of the SKALA4.1 is prioritized to be matched to 50 Ω as best as possible, a boom of varying Z_0 does not violate this requirement if a non-constant z-profile of the boom cross-section is chosen. Such attempts were made with constant, linear, parabolic boom profiles and combinations thereof, but were eventually not proven fruitful in tackling spurious radiation. A different shape of the dipoles besides the triangular, as in [74], was also an attempted solution, but apart from significantly changing the antenna geometry, it was again proven an unsuccessful redesign option. Indeed, as has been shown in [79] this is a complex problem involving both Z_0 and the dipole impedances.

Attempts at lumped element loading by using inductive or capacitive loads have already been made in a number of works, even for slot-antenna radar applications, as in [80]. Most relevant to ours, [81] and [82] used an inductance to suppress such undesired modes but in a 2-dipole configuration, while He et.al.[83] using a capacitive load aimed mostly at improving the reflection coefficient of the designed antenna. The choice of an RLC load as a bandstop circuit in this work is made both for simplicity of design as well as for practical reasons relating to phase stability. An RLC circuit is a well-understood element and has also found application in other types of antennas, such as to reduce mutual coupling in arrays. The position of such a circuit in any antenna design has to be integrated in such a way so as not to interfere with antenna performance. For resonant antennas, this mainly means the primary modes; as will be proven in the following section, in our case the

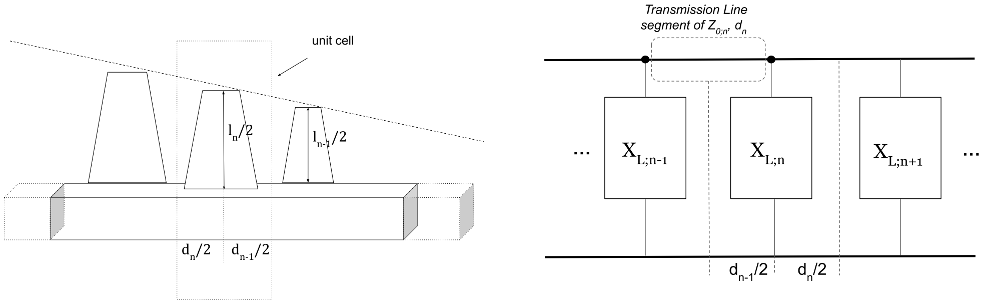

(a) **(b)**

Figure 3.1. (a) Log-periodic cell of an LPDA configuration, including the dipole of arbitrary shape and the boom segment to which it is connected (dimensions are also shown), (b) The equivalent circuit model of (a) in non-resonant regions of the LPDA.

placement should correspond to the maximum of the secondary dipole mode current distribution.

Our goal in the following section is to generalize this method in all LPDAs using non-straight wire dipoles, with respect to achieving gain smoothness, while keeping the reflection coefficient identical for all practical purposes. The cost on radiation efficiency should also be minimum.

3.2 Effect of parallel RLC load in LPDA regions

In this section, we consider all dipoles of an LPDA as potentially loaded with an RLC circuit, while application is found usually only on some of them, depending on the operating frequency range of the antenna. We shall examine the effect of dipole loading with an RLC parallel circuit in the frequency regions where the dipoles of an LPDA are non-resonant and the regions where the dipoles resonate with their primary or secondary mode. In all of these regions some approximations can be made both on the behaviour of the RLC load and the main function of the log-periodic "cells". One such cell is a dipole and a segment of the boom as transmission line, and is the unit element which is scaled in the log-periodic configuration, as can be seen in Fig. 3.1a where 3 cells are shown to highlight the cross-feeding of consecutive dipoles (by the symmetric boom conductor - not shown). All these cells connected as a network appear, approximately, either as continuously scaled transmission line segments (propagating power) or equivalent resonant circuits themselves (radiated power), or a combination of both [79].

3.2.1 Non-resonant regions

We first introduce a dipole indexing using an increasing n, from shorter to longer elements on an LPDA. If the wavenumber is $k = \omega/c_0$, then in the region $kl_n < \pi$, we expect all dipoles 1 through n to be short and thus to not radiate (the exact bound depends on the dipole's parameters). For an LPDA, this region "moves" when focusing on a different frequency. As has been shown in [84, 85], these dipoles load in parallel the boom transmission line, in this case capacitively. If a log-periodic cell n has an equivalent transmission line inductance $L_{0,n}$, capacitance $C_{0,n}$ and thus characteristic impedance $Z_{0,n} = \sqrt{L_{0,n}/C_{0,n}}$, then the reactance added to the boom is:

$$X_{L,n} = -Z_{0,n} \cot\left(\frac{kl_n}{2}\right) \tag{3.1}$$

A circuit equivalent of the log-periodic dipole antenna in its non-resonant region can be seen in Fig. 3.1b. Following the same indexing as that of the dipole it is potentially attached to, the parallel n-th RLC load has a complex value:

$$Z_{RLC,n} = \frac{j\omega L_n R_n}{R_n(1-\omega^2 L_n C_n) + j\omega L_n} \tag{3.2}$$

and it is tuned at the second resonant frequency of its dipole such that:

$$\omega_{n,2} = \frac{1}{\sqrt{L_n C_n}} \tag{3.3}$$

In the low frequencies that we are examining, we will approximate it as an inductive load $j\omega L_n$, since $\omega^2 L_n C_n \ll 1$ and $R_n \gg \omega L_n$. This n-th load, when attached to the dipole n, modifies $Z_{0,n}$ in a non-uniform way, perturbing the transmission line model. The inductance L_n has to be small with respect to $L_{0,n}$ and $1/(\omega_{n,2}^2 C_{0,n})$ (approximate expressions of which can be inferred from [86]), in order not to significantly affect the equivalent dipole characteristic impedance, and thus the added reactance to the boom.

In the frequency range, which according to the dipole n is approximately such that $\pi < kl_n < 2\pi$, we cannot employ the same transmission line model as in the short dipole region, because of the fact that we have non-negligible radiation which works as an end-effect on this transmission line. It should be clarified though that this region still propagates the power which has not been radiated due to non-perfect matching to the boom[1], even though the effect is more complicated. Lumped element non-dissipative loading of isolated dipoles in this region (as is also our case, since $Z_{RLC;n}$ can still be approximated as inductive), for straight wires, has been theoretically examined in [87]. The dipole input impedance is dependent on the current through the lumped element, which is zero for a straight wire dipole - hence no effect would be visible - but close to zero for other elongated shapes, thus we are not expecting any significant differences with respect to how an unloaded dipole would behave in the log-periodic configuration.

3.2.2 Resonant regions

In these frequencies, which are roughly around $kl_n \approx \pi$ or $kl_n \approx 2\pi$ respectively (see Tab. 3.1, rows $f_{n;1},\ f_{n;2}$), the dipole radiates power in its primary or secondary mode. The approximation depends on the width of the dipole (thick or thin), as well as on the resonance region; in fact, in an LPDA closely spaced dipoles interact, causing the

---

[1] This has been seen by checking the Poynting vector in near-field, 2D FEKO simulations of the xy-cut of the boom at heights z where the attached dipoles satisfy $\pi < kl_n < 2\pi$, which has confirmed that the bulk of complex power is reactive and propagating in the boom.

distinct resonance of each one to be away from its self-resonance. The most useful tool to assess their excitation is the quality factor. According to [88], the Q-factor of a resonant antenna at any resonant frequency ω_r of order r, is approximated as:

$$Q(\omega_r) = \frac{\omega_r |Z'(\omega_r)|}{2\Re\{Z(\omega_r)\}} \tag{3.4}$$

where $Z(\omega_r)$ denotes the complex impedance of the antenna, and the primed quantity is its derivative, at resonant frequency ω_r. It must be noted that this definition holds both for lossless and lossy antennas, by adding the losses as an equivalent term of the real part. For our loaded dipole case, as has been already mentioned, the best position to place the load is where the current excited at $\omega_{n;2}$ is maximum. This does not only stem from the intuitive fact that we want to suppress this current as efficiently as possible, but is also necessary if we want to not intercept power from the primary mode at $\omega_{n;1}$, whose current should be minimum at the same point. If the dipole has an elongated shape, a lumped impedance placed at both $x_n = \pm l_n/2$, i.e. the ends along the largest dimension, satisfies this requirement.

Focusing on the second resonance of interest, $\omega_{n,2}$, our load is at its resonant frequency so we have exactly $Z_{RLC;n} = R_n$. We can therefore represent this equivalent loss resistance, according to [88], as:

$$R_{L;n}(\omega_{n;2}) = \left| \frac{I_n(\omega_{n;2}, l_n/2)}{I_n(\omega_{n;2}, 0)} \right|^2 R_n \tag{3.5}$$

where $I_n(\omega_{n;2}, l_n/2)$ is the dipole current at the load placement and $I_n(\omega_{n;2}, 0)$ at the excitation point, at $\omega_{n;2}$. If we denote the n-th dipole impedance as $Z_{dip;n}$ then for the loaded (and hence lossy at $\omega_{n;2}$) n-th dipole the impedance of Eq. (3.4) is indexed as $Z_n = Z_{dip;n} + R_{L;n}$. By the desired level of the Q-factor, our R_n is chosen. Note that in this factor there is an implicit assumption of tuning the antenna to its resonance such that $\Im\{Z(\omega_r)\} = 0$; away from self-resonance (or in an untuned antenna as in [88]) there exists some extremum of $\Re\{Z(\omega_r)\}$ such that $\Im\{Z'(\omega_r)\} > 0$. To find other meaningful representations of modal Q-factors of the antenna by tuning a specific modal reactance to zero one would need to resort to an internal energy formulation, as in the work of Capek [89].

3.3 Application on the SKALA4.1 antenna

SKALA4.1 is a log-periodic antenna which features 19 triangular dipoles, a bow-tie dipole at its bottom, and a dual-conductor transmission line of rectangular cross-section as boom, while it is placed over a ground mesh which can be approximated as an infinite Perfect Electric Conductor (PEC). It is a dual-polarized antenna, but with a very low level of cross-coupling, so our previous findings should apply for each one of the polarizations independently.

Currently, the secondary modes are partially mitigated by tilting of both rectangular conductors at an angle $\theta_{boom} = 1°$. This allows for the boom to radiate part of the leaked power in a non-resonant manner, as it does not act as a perfect transmission line. A 3D view of the antenna has been presented in Fig. 3.2a.

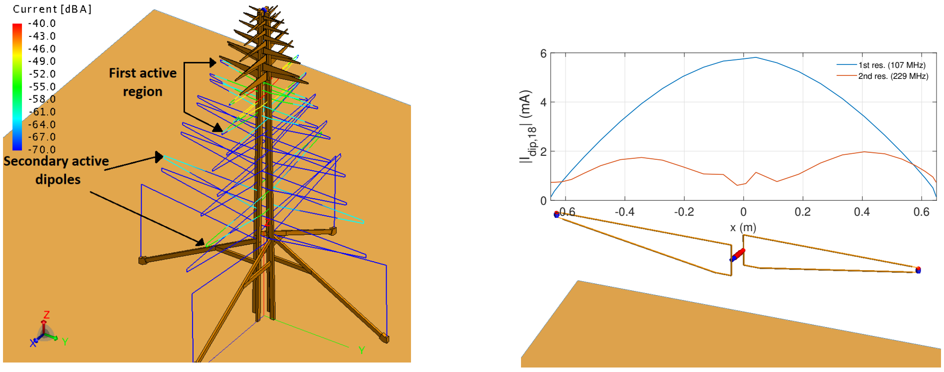

(a) **(b)**

Figure 3.2. (a): A SKALA4.1 antenna excited at 229 MHz, geometry colored for wire current in dBA. Two active regions are discerned, with dipole 18 (counting from top to bottom) being the parasitic, (b): A FEKO schematic of triangular dipole 18 of SKALA4.1 over an infinite PEC surface, where 3 ports can be seen: a middle one for the voltage gap excitation as well as two edge ports where the loads are placed. Plotted are also the current distributions of the first and second resonances, as a function of the x coordinate, at 107 MHz and 229 MHz respectively.

3.3.1 Individual Dipole simulations

We first examine individual dipoles of the SKALA4.1 antenna, which present a secondary mode due to their triangular shape. The 5 longest triangular dipoles (15 to 19) are examined separately, as their secondary modes fall within the operational range of SKA-Low. For each of these dipoles, we choose our RLC parallel load values according to 3 design criteria:

1. The second order resonant frequencies, given by Eq. (3.3) for each dipole and listed in Tab. 3.1.

2. The RLC resonant circuit Q-factor. It can be shown from circuit theory that Eq. (3.4) reduces to $Q_{RLC;n} = R_n\sqrt{C_n/L_n}$, for the RLC load attached to the n-th dipole. We would like to choose our bandwidth arbitrarily small, but this choice has practical issues since the tolerance of lumped elements cannot be zero. Thus, a value of $Q_{RLC;n} = 10$ was chosen as a compromise.

3. The value R_n is chosen, according to Eq. (3.5), which accounts for the desired level of ohmic losses at the resonance frequency. Simulations were needed to test various R_n values and assess their effect, because there is no simple closed-form of Eq. (3.5) for triangular dipoles.

In all the following simulations, FEKO commercial software is used, and the standard Method of Moments. To find suitable R_n values, the dipoles were modelled isolated and placed over a PEC, while excited at a wire port of characteristic impedance $Z_0 = 50\ \Omega$ connecting the triangular monopoles in their middle, with a fixed voltage set to $V_s = 1$ V. The two other ports seen with a red/blue polarity at the tip of the triangles are the loading positions. As an example, dipole 18 is

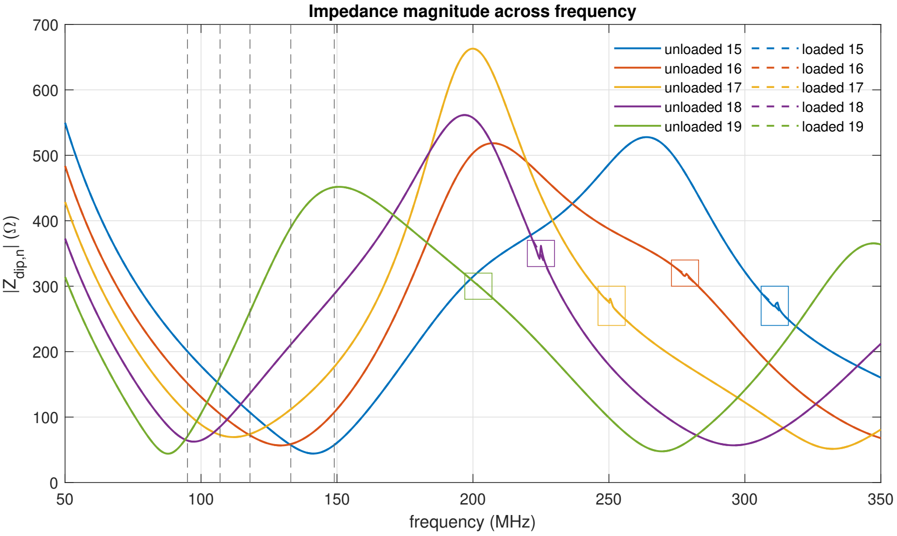

Figure 3.3. Simulated dipole impedance magnitude for unloaded and RLC loaded dipoles with an $R_n = 10\ \Omega$ in the operating frequency range of SKALA4.1. 10 curves are plotted, almost identical per 2, while the vertical lines indicate the $f_{n;1}$ of Tab. 3.1.

depicted in Fig. 3.2b, with its primary and secondary resonant currents are also plotted, while the x-axis values have been averaged for the corresponding mesh elements of the two triangle sides. We note the non-zero current on the two edges for the secondary resonance, as explained in Sec. 3.2. After assessing the impedance and current response, we have chosen a value of R_n such that the secondary mode no longer creates an impedance glitch, confirming that also for the gain pattern. The resistor value that seems to first show insignificant impedance and gain anomaly for all dipoles is $R_n = 10\ \Omega$.

We note that we did not further optimize the Q_n, R_n values (which are indicative more of the order of magnitude needed for the RLC circuits), since they were suitable for our simulations; higher Q's can also work but, as explained in Sec. 3.4, result in L values whose implemented components were not suitable for our prototypes. Higher R values might be needed for other antennas, but they would unavoidably induce more losses.

We first present the isolated dipole absolute impedance, to ascertain its behavior across the full frequency range when the load is added. Fig. 3.3 contains a plot of all unloaded dipoles, and all loaded ones with an RLC of $R_n = 10\ \Omega$. The respective unloaded/loaded curves are indistinguishable for this scale of values, such that the load has a highly targeted effect; the glitches are highlighted in boxes. We have also confirmed the validity of the transmission line model for the impedance of short dipoles, since all of them have a strong reactive component and are close to the cotangent shape of Eq. (3.1), up to frequency points close to the SKALA4.1 first resonances (vertical lines, see Tab. 3.1). The exact cut-off point of this model would have to result by a fit of the simulated data to the equation, which is out of our scope. It is also remarked that $|Z_{dip;n}|$ is influenced by the infinite PEC which is in some cases in the near field and thus interacting reactively.

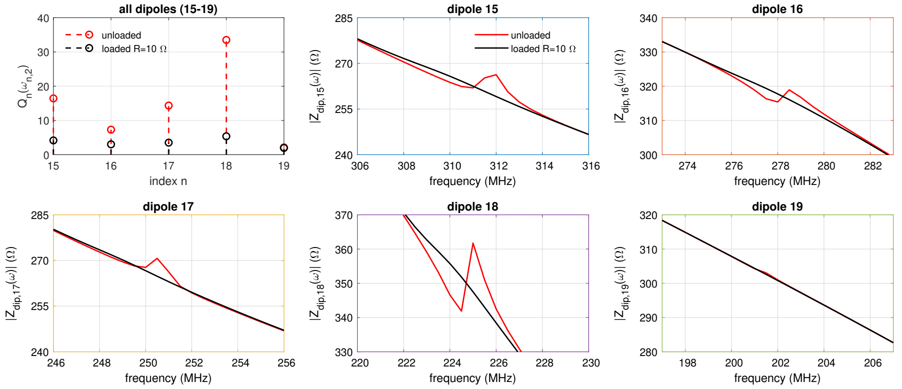

Figure 3.4. Calculated Q-factors of dipoles 15-19 (unloaded and loaded ones with an RLC of $R_n = 10\ \Omega$) of the SKALA4.1 antenna at frequencies $\omega_{n;2}$ (top left) and zoomed impedance glitches of (top right and the rest), whose color contour refers to the respective box of Fig. 3.3.

In Fig. 3.4 (top left), we present the calculated Q-factors for the unloaded dipoles, and the case of loaded ones with values $R_n = 10\ \Omega$. We use Eq. (3.4) for all cases preceded by index n before $r = 2$, while also adding the loss resistance of Eq. (3.5) for the loaded cases. All other subfigures zoom into the impedance glitch boxes of Fig. 3.3 (color contours of Fig. 3.3 correspond to box colors) to emphasize the desired mode suppresion. We can see from this plot that the calculated Q-factors drop below 5 with the addition of a load. Also note the apparent degeneracy of the calculated Q of dipole 19, which is low for all cases, along with the almost invisible glitch peak in the unloaded case. This could be a result of the closer near-field interaction of this dipole with the infinite ground plane.

The Q-factor calculation and impedance simulation serve mostly as an evaluation of the technique; the RLC circuit response as a filter is a typical bandpass curve, so relevant simulations are omitted (such a simulation curve can be found in Fig. 3.8b of Sec. 3.3 for verification purposes during our laboratory experiments). Specific antenna designs could require the choice of arbitrary resistors and Q-factors for each dipole of the antenna; for SKALA4.1, these constant values perform quite well without the need for further optimization. It is evident from the analysis of this section that the secondary mode glitch is inherent to the dipoles.

3.3.2 SKALA4.1 simulations

In previous simulations of SKALA4.1 [9], dipoles 15 through 19 tested in the Sec. 3.3.1 were observed, first by means of their anomalous gain response, to be resonating with secondary modes at the frequencies listed in Tab. 3.1 (with a maximum amplitude of around 0.2 dB, as seen in Fig. 3.5, “original SKALA4.1" curve). Also included in this table are the electric lengths of the dipoles at these frequencies, which are close to λ, and the respective amounts for the primary resonances. These are defined as local extrema of $\Re\{Z\}$ that satisfy $\Im\{Z'\} > 0$, as in [88], and have been extracted from simulated data of the antenna. We note the high accuracy of the theoretical approximations for both kinds of modes, with minor deviations for the primary

Table 3.1. First and second dipole resonance frequencies and electric lengths for a SKALA4.1 antenna

Dipole n	15	16	17	18	19
$f_{n,1}$ (MHz)	149	133	118	107	95
$f_{n,2}$ (MHz)	318	284	255	229	206
$l_n/\lambda_{n,1}$	0.477	0.473	0.464	0.462	0.456
$l_n/\lambda_{n,2}$	1.02	1.01	1.00	0.99	0.99

modes as we anticipate in Sec. 3.2.2, due to dipole thickness and mutual coupling.

Further verification was made by examining the excited currents of the involved dipoles, as in Fig. 3.2a for 229 MHz, where the full SKALA4.1 is displayed with a first active region which includes dipoles 10-12, while dipole 18 forms the second active region and is resonating with a secondary mode, which has a maximum current at the farthest points from the boom. The dynamic range has been chosen according to the maximum/minimum values, while the linear currents are shown in dBA to better emphasize their difference (which is around 30 dB).

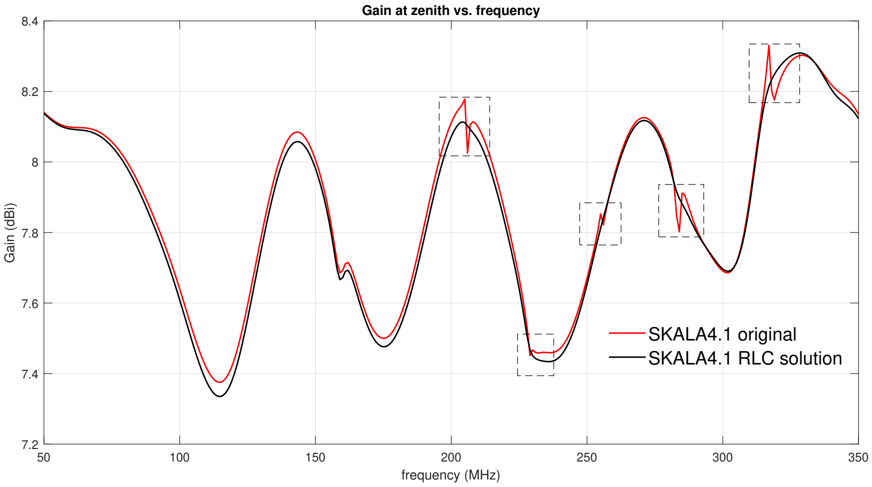

Figure 3.5. Gain in dBi at zenith for the SKALA4.1 X-polarized antenna for 2 different cases: unloaded (original SKALA4.1), RLC circuit loaded dipoles ($R_n = 10\ \Omega$). Dashed boxes are used to highlight the narrow-band glitches.

We next incorporate the RLC circuits into the full SKALA4.1 antenna, and a simulation is run with FEKO in the full operating frequency range. Fig. 3.5 shows our results in terms of antenna gain at zenith. The “original" label refers to the gain achieved with the unloaded antenna, while “RLC solution" label refers to our current loaded dipole solution. All dipoles 15-19 have been loaded in their respective edge (as in the ports of Fig. 3.2b). As can be seen, due to the adjusted 1-dB dynamic range, we have managed to eradicate the anomalous feature.

We also present some results in other spherical directions for the gain pattern. Fig. 3.6 shows the gain response in the band 200 MHz to 350 MHz for the same,

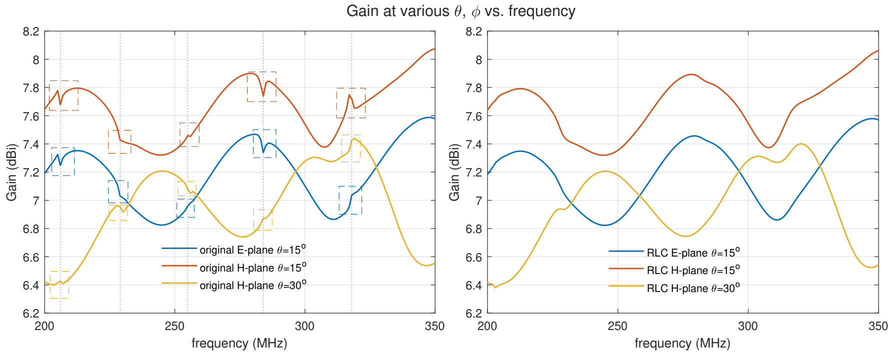

Figure 3.6. Gain in dBi at various θ, ϕ for the SKALA4.1 X-polarized antenna for two different cases: unloaded, original SKALA4.1 (left) and RLC circuit loaded dipoles (right). Dashed boxes are used to highlight the narrow-band glitches.

’original’ (left plot) and ’RLC’ loaded (right plot) antenna cases, at $\theta = 15°$ for the E- and H-plane ($\phi = 0°$ and $\phi = 90°$), as well as at $\theta = 30°$ for the H-plane. These directions were chosen such that all the gain values are comparable to each other and the glitches visible. It is concluded that, apart from a barely visible feature at $\theta = 30°$, $\phi = 90°$ and at 206 MHz, all other glitches are eradicated and the response appears smooth.

The cost on radiation efficiency is insignificant as well (less than 1%), as can be seen in Fig. 3.7a for the ’RLC solution curve’. This is in any case visible in the slightly lower gain values for the RLC solution throughout the full frequency band. The real aluminum antenna would also induce some more losses due to the finite conductivity [63], but those are additive with respect to the phenomenon we examine here so we need not simulate that model too.

In the case of SKALA4.1 antenna, simplicity of design is also a critical factor, and since the RLC load has optimized values for different dipoles, simpler solutions were also pursued. For example, we can use only a resistor to achieve the same performance in terms of glitch eradication, but we can directly see that this would degrade the low frequency performance. If we consider a per unit length R_n as an example for the losses of a short dipole transmission line model, and a loss factor of $\alpha_n l_n/2 = R_n l_n/(4Z_{0,n})$, the shunt load on the boom is such that:

$$\begin{aligned} Z_{L;n} = Z_{0;n} \coth\left((\alpha_n + jk)l_n/2\right) = \\ Z_{0;n}\frac{\coth(\alpha_n l_n/2)(1+\cot^2(kl_n/2))}{\coth^2(\alpha_n l_n/2)+\cot^2(kl_n/2)} \\ +jZ_{0;n}\frac{\cot(kl_n/2)(1-\coth^2(\alpha_n l_n/2))}{\coth^2(\alpha_n l_n/2)+\cot^2(kl_n/2)} \end{aligned} \tag{3.6}$$

Irrespective of the constants into the hyperbolic cotangent term (which is not exact since we assume distributed losses), numerical plots of the behaviour of $\Re\{Z_{L;n}\}$, $\Im\{Z_{L;n}\}$ in the limit $l_n \to \lambda/4$ have shown that the image term diminishes more quickly than real one. At lengths reaching $\lambda/4$ the lossy $\Re\{Z_{L;n}\}$ becomes important, and this is the mechanism by which the antenna loses energy, which we

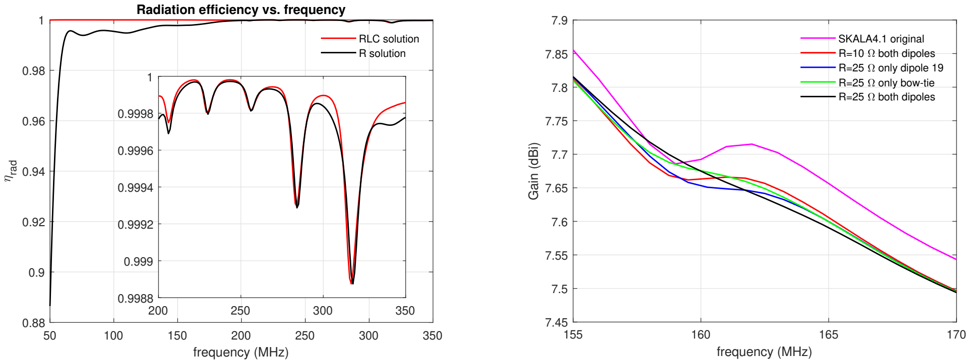

(a) **(b)**

Figure 3.7. (a): Radiation efficiency of SKALA4.1 antenna loaded at dipoles 15-19 with RLC circuits and solely resistors R, respectively. The original efficiency is not added since it is, given the PEC metal assumption, equal to 100%, (b): Gain at zenith glitch at 161 MHz, for an unloaded SKALA4.1 antenna, as well as cases of RLC parallel loads on dipoles 19, the bow-tie or both with $R = 10\ \Omega$ or $R = 25\ \Omega$.

expect to see as a radiation efficiency reduction. These wavelengths for dipoles 15 to 19 (listed in Tab. 3.1) correspond to frequencies of 50 MHz-70 MHz, so this is the most affected regime. Simulations have shown that indeed this solution has the same performance with respect to the glitch supression, but induces a 10% loss in radiation efficiency, as can be seen in Fig. 3.7a for the 'R solution' curve.

Other types of spurious radiation

In this section, a problem specific to the SKALA4.1 antenna is addressed, which is inherent to the addition of a bow-tie dipole at its bottom. Such phenomena may also appear in similar modifications of LPDAs, whereby the dipole at one of the antennas extremes has a different shape.

For SKALA4.1, since the bow-tie dipole (the 20-th dipole placed just above the ground) has a different shape and resonance feature, and is closely spaced to the triangular dipole 19, they interact strongly presenting mutual coupling related modes [82, 55]. It was observed by means of the gain pattern smoothness, that this mode is strong enough to create a glitch at around 161 MHz, which is visible in Fig. 3.5. In this case, the correct placement of an RLC parallel load was found to be at $x \approx$ ł$_{20}/4$ (here l_{20} stands for the x-axis wire dimension) of the two dipoles involved, by examining their maximum current at this resonant frequency. Fig. 3.7b shows another close-up of the gain response by tuning the RLC at 161 MHz, using $Q_{RLC} = 10$ and cases of $R = 10\ \Omega$ and $R = 25\ \Omega$. Since $R = 10\ \Omega$ was proven inadequate, for $R = 25\ \Omega$ we have placed the RLC loads on dipole 19, on the bow-tie, and both of them; the latter case was proven to have the best effect. We can see that the associated glitch is completely flattened when using $R = 25\ \Omega$ on both dipoles, while it is still visible for all other cases (it performs better though only on the bow-tie than only on dipole 19). Due to the position of the RLC load being away from the far end of the dipole, a sole resistor $R = 25\ \Omega$ would not achieve an acceptable performance in lower frequencies, so such a solution is not applicable to SKALA4.1 when all of its frequency coverage needs to be functional.

3.4 Experimental Verification

For the proposed RLC parallel circuit loading solution, we have attempted an experimental verification using a SKALA4.1 and replacing the dipoles responsible for the glitch phenomenon with new ones, designed in a custom way such that we could attach this type of load. Sirio Antenne (`https://www.sirioantenne.it/it/`), the contractor of antenna production for SKA-Low, has redesigned and manufactured these new dipoles. The practical solution for soldering the RLC circuit is a PCB element also designed by Sirio Antenne, a ≈ 2 cm long FR4 piece with conductive paths shown in Fig. 3.8b, and also screwed on one of the dipoles in Fig. 3.8a with its RLC components soldered.

3.4.1 RLC circuit measurement

To first measure and ascertain the performance of the RLC circuit as a 2-port device, we used an interface such as that shown at the center left of Fig. 3.8b. Coaxial cable segments, the inner conductors of which were extended via circular rings on their free end (the other end containing their SMA), were used for compatibility with the VNA interface. These rings were screwed on the PCB, while a short-circuit connection of the outer conductors creates a virtual ground. We have also introduced a modification of the values of the loading circuit in order for a feasible prototype to be constructed. If one uses a resistor of $R_n = 10\ \Omega$ that was found in the previous section to be ideal, then the inductance values turn out to be very low (in the order of 100's of pH). This kind of component can only be implemented as a surface mount, which is hard to integrate in a parallel circuit manually, as we planned to do. We thus scaled the L_n values by one order of magnitude, which according to Eqs. (3.3), (3.4) also means that C_n must be scaled down and R_n up by the same factor. That still allows for practical RC values, while a $R_n = 100\ \Omega$ resistor would induce some minor losses in the range 140-200 MHz.

To add to that complexity, it was further realised that parasitic components were inevitable in our manual RLC component integration on the PCB, which account for a shift in resonance frequency. For example, with an initial market inductance of $L_{18} = 7.15$ nH and a market capacitance of $C_{18} = 47$ pF used for constructing an initial circuit for the 18-th dipole, a parasitic $L_{p;18} = 8.44$ nH was calculated for a shift from the designed (229 MHz) to the initially measured (338 MHz) resonance, such that the actual inductance is $L'_{18} = L_{18} + L_{p;18} = 15.59$ nH. We should emphasize here that this PCB component was not optimized in its electric properties, and the soldering/screwing interfaces were expected to induce parasitics. Using a new value of $C'_{18} = 33$ pF, the new measured resonance, at 217.5 MHz, was the closest approach we could obtain to target the design frequency of 229 MHz. The constraint is set by C'_{18} as the closest standard market capacitance to the one obtained from Eq. (3.3) by using L'_{18}, keeping the resonance fixed at the design frequency. Tab. 3.2 collects the $L_n^{(sim)}$, $C_n^{(sim)}$ values that have been ideally used for each dipole in simulations

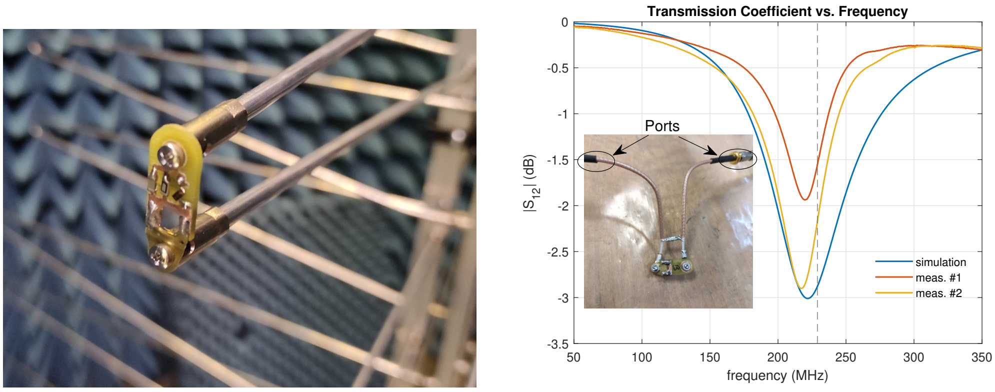

(a) **(b)**

Figure 3.8. (a) Redesigned triangular dipole by Sirio Antenne, adding a screwable PCB on which RLC components are soldered, (b): RLC parallel circuit $|S_{21}|$ in dB, for a simulated circuit using $R = 100\ \Omega$, $L'_{18} = 15.59$ nH, $C'_{18} = 33$ pF and two measured prototypes (one of them shown as constructed in the image at the center-left) using the same values, which are observed to resonate at 217.5 MHz. A parasitic inductance $L_{p;18} = 8.44$ nH can account for an initially measured shift (not shown) from the designed resonance frequency, while the amplitude is variable among our 2 prototypes.

in Sec. 3.3, the market inductances L_n used throughout, and the corrected market capacitances C'_n. These are the final values we used to construct the prototypes; the values C_n, L'_n are instead omitted since they are auxiliary for the correction procedure described above. It is reminded that, $R_n = 10\ \Omega$ and $R'_n = 100\ \Omega$ respectively, for all dipoles.

Table 3.2. Simulation and prototype construction L, C values. L_n and C'_n are market values. L_{16} and C'_{16} are omitted since an experimental verification was not possible for this dipole.

Dipole n	15	16	17	18	19
$L_n^{(sim)}$ (nH)	0.5	0.56	0.624	0.695	0.772
$C_n^{(sim)}$ (pF)	500.5	560.4	624.1	695	772.6
L_n (nH)	2.55	-	7.15	7.15	7.15
C'_n (pF)	20	-	24	33	44

The example effective circuit (considering the R'_{18}, L'_{18}, C'_{18} values) was also simulated. Viewing it as a 2-port network with the coaxial cables corresponding to its ports, and a reference impedance of $Z_0 = 50\ \Omega$, a simple Z-to-S transformation results in $S_{21} = (2Z_0)/(Z_{RLC;18} + 2Z_0)$, using Eq. (3.2) for $Z_{RLC;18}$. The $|S_{21}|$ of the simulated and measured RLC parallel load of 2 separate prototypes are presented for two constructed prototypes (meas. #1, meas. #2) in Fig. 3.8b (design frequency at the vertical line). The shape of the resonance features of the two curves is in good agreement, while the amplitude varies at a level of ≈ 1 dB among the constructed prototypes; despite that, these circuits turned out to be useful in the antenna measurements.

3.4.2 SKALA4.1 coupling measurement

The experimental test that we have conducted is essentially similar to that of [77], a measurement of the coupling between a SKALA4.1 antenna and a transmitting VHF antenna, in terms of the scattering parameters of the system. The VHF antenna is a Yagi-Uda composed of 7 dipoles for receiving TV signals in the range of 180-260 MHz, so we have focused our measurement on the 3 first glitches as previously described, while the highest frequency one was also observed. A number of anechoic chamber experimental campaigns took place at the Arcetri Astrophysical Observatory in Florence, as can be seen in the photo of Fig. 3.9a. Due to the limited dimensions of the anechoic chamber, the measurement is a near-field (reactive) one, with a horizontal pointing of the VHF antenna. The chamber was filled with extra absorbing panels on its floor, except for a cross-like area 1.6 m $\times$1.6 m that was occupied by a 5 cm-spaced rectangular grid acting as a ground plane. SKALA4.1 was excited along its Y-polarized dipoles, parallel to the dipoles of the VHF antenna, while its orthogonal polarization was terminated with a 50 Ω load, and an Agilent VNA was used to perform the measurement and save the data. Importantly, despite these differences from the simulations (non zenith pointing, non far-field regime), the glitch phenomenon clearly appears in our data.

During the anechoic chamber measurements, we obtained two sets of results, each of them an ensemble average of 10 frequency sweeps without changing any measurement condition to reduce the random noise, since the horizon pointing provides a low level of coupling more susceptible to it. A fine resolution of 0.25 MHz was used. Firstly, a set of measurements with the original dipoles of SKALA4.1 was made, while the next one was made after screwing the new, RLC-circuit loaded dipoles numbered 15, 17, 18 and 19. Intermediate measurements were also made after each dipole substitution to check the consistency of the results.

We first show in Fig. 3.9b the measured $|S_{22}|$, in the four frequency windows around the primary resonances of the dipoles (as listed in Tab. 3.1), so as to test the immunity of the response out of the frequency bands where the glitches occur. It has to be emphasized that due to the anechoic chamber environment having a close proximity to the antenna, imperferct absorption and scattering from the VHF antenna, the measured reflection and log-periodic resonant frequencies do not closely follow that of [9], which was a more precise measurement. However, it is evident that in the first 3 cases the shape is almost identical. The last panel is in the range of frequencies where the RLC load of dipole 19 should already attenuate and phase shift at an adequate level as to account for the apparent differences between the 2 curves.

For the second resonances, we will demonstrate the narrow-band $|S_{21}|$ measurement data in two ways: firstly, we show a zoom into a 5 MHz bandwidth to visually confirm their amplitude mitigation, as in the top panels of Fig. 3.10. The features are small in amplitude (as Fig. 3.4 has already suggested), but discernible from the otherwise smooth trend (only the last panels are more noisy, due to the lower level of coupling). As we have shown in previous results of this method of assessing the glitches in S_{21} measurements [77], there are many differences between the anechoic

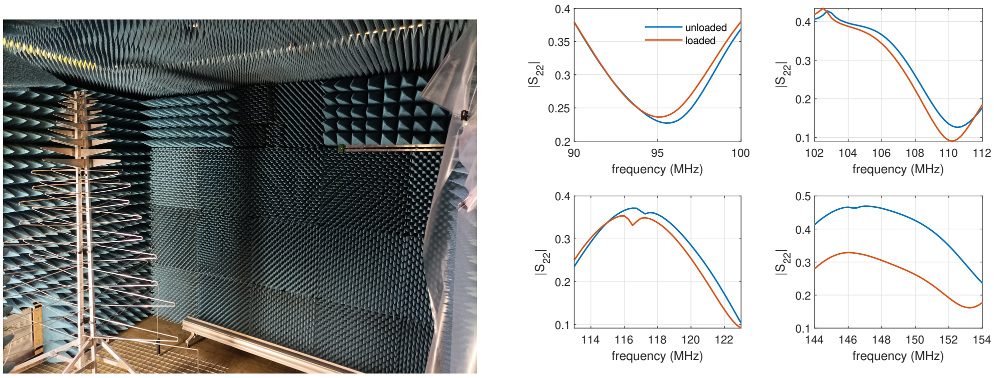

(a) **(b)**

Figure 3.9. (a) Measurement configuration of a SKALA4.1 antenna and a VHF Yagi-Uda antenna at the Arcetri Astrophysical Observatory anechoic chamber, (b): $|S_{22}|$ VNA measurement, where port 1 is connected to a VHF antenna and port 2 is connected to a SKALA4.1 under two conditions: original, unloaded dipoles 19, 18, 17 and 15 (left to right and top to bottom), and the corresponding redesigned, loaded ones. The 4 frequency windows chosen correspond to a 10 MHz range around the primary resonance frequency of each dipole, listed in Tab. 3.1.

chamber environment and a free-space simulation that is the most obvious way of a first approximation. We do not compare with simulation results here since it would be extremely challenging to introduce in the simulator the real operative conditions and reflection properties of the chamber walls. Therefore, the effectiveness of the proposed technique is here demonstrated by 2-step comparative measurements conducted on the antenna with and without the RLC load on the dipoles. A 'differential' such analysis ensures that the reduction of the glitch could not have been produced by the anechoic panel or by the VHF antenna whose contributions are identical in the two consecutive measurements.

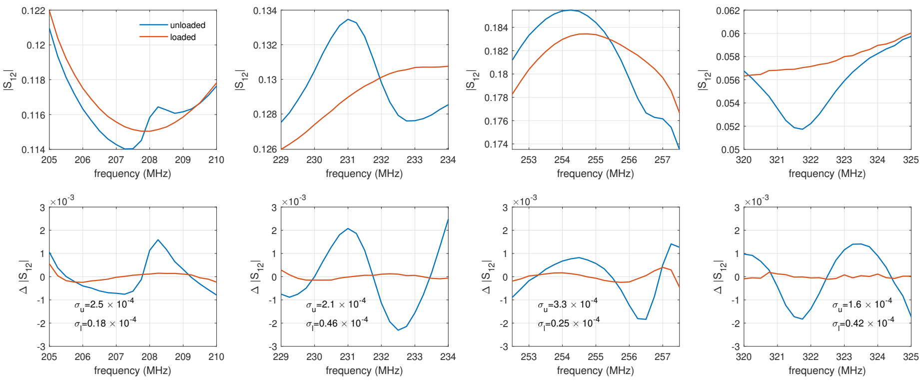

Figure 3.10. Top panels: $|S_{21}|$ measurement data, bandlimited to selected windows around each glitch of dipoles 19, 18, 17, 15 (top to bottom), Bottom panels: Residuals of the curves of the left panels after subtracting a polynomial fit of second degree to isolate the glitch from the smooth variation. Standard deviations are given on the lower left.

Secondly, for each of the two curves of Fig. 3.10, we fit a second degree polynomial and examine the residuals shown in the bottom panels of Fig. 3.10. This is a common method used in the de-embedding of instrumental effects on real radioastronomical data which, although different in our case (artificial source, coupling measurement and not far-field gain), can offer an insight on the smoothness of the curves [90]. On the lower left corner of these panels we report the standard deviation over the bandwidth for both the unloaded/loaded curves ($\sigma_{u/l}$). For this statistic measure to be comparable among the cases, the window has been selected such that the dynamic range of values does not change appreciably (≈ 0.01 for all cases), and the number of frequency points is also the same. It is verified that in all cases the loaded dipoles curve achieves a smoother trend with respect to the features resembling the glitches present in the unloaded dipoles curve. The residuals are always lower, as well as their standard deviation, a result which points to a smoother SKALA4.1 response under RLC dipole loading.

The problem of low-frequency dipole glitches eradication by RLC loading has been published in the Radio Science Journal as “Suppresion of Log-Periodic Dipole Antenna Spurious Radiation by Lumped Element loading for Radioastronomical Application", by the author and collaborators [91].

Chapter 4

Antenna platform effects on SKA-Low

Log-periodic antennas belong to the class of frequency-independent antennas, that is, constant characteristics in large frequency bands are approached. In practice though, the gain response of a log-periodic antenna, especially at the extreme of its operating band where the front-to-back (at 0° and 180°) beam gain ratio can deteriorate, can be enhanced by adding a ground plane that acts as a reflector. The presence of a metallic ground plane produces distinct spectral features when illuminated by an arbitrary antenna, due to the reflection from the backscattering of the antenna and diffraction from the edges.

Our main objective in this chapter is to examine the effect of a ground plane structure for a SKALA4.1 [9] array. While the principal reason for the employment of such a ground plane in SKA-Low is the antenna gain enhancement in low-frequencies, this choice also has to do with the soil which underlies the antennas, thus making the observation more sensitive to the environmental parameters (moisture, mineral content etc.) when it remains uncovered.

In the first and second engineering prototypes of SKA (AAVS 1& 2), certain concerns have been explored specific to the spectral smoothness of the antenna beam, in order to enable wide-band beamforming, as well as to fulfill the scientific prerequisite of decoupling the instrumental response from the astronomical signal of interest. On-site deployment and operation also demonstrated the calibration as well as commissioning challenges relating to large low-frequency arrays [13, 92].

The numerical simulations of such prototypes [67] usually assume an infinite ground plane in order to ease the computational burden, an approximation which is in general valid for high frequencies (and thus electrically large structures). Simulations including the finite ground plane, have only been performed in a pair of works [93] [94], both with the limitation of examining the antenna pattern in certain selected frequencies.

We focus here on the low-frequency (50-100 MHz) spectral response of both an isolated SKALA4.1 antenna placed at various positions with respect to its finite ground plane, as well as the Embedded Element Patterns (EEPs) of selected antennas of the full-station layout, and compare the results to the infinite ground plane solution. Two numerical solvers are used for initial verification, and the results are shown to be spectrally consistent with the far-field radiation by an arbitrarily illuminated circular plane. A speed-up 3-step approximation is also outlined for one of the solvers justifying its applicability on our problem.

4.1 Solid Ground plane

4.1.1 Theoretical approach (point source)

A circular plane of radius a illuminated by an azimuthally symmetric electric field amplitude vector $\vec{E}_i(\rho)$ (i.e., no ϕ dependence), produces a radiated electric far-field pattern [4]:

$$\hat{\theta} \cdot \vec{E}_a(k, r, \theta) = \frac{k\cos(\theta)}{r} \int_0^a \hat{\rho} \cdot \vec{E}_i(\rho) J_0(k\rho sin(\theta))\rho d\rho \tag{4.1}$$

Here $k = 2\pi f/c_0$ is the wavenumber, f the frequency, r the radial distance from the reference (center of the ground plane) to the observation point while $\vec{\rho} = \rho\hat{\rho}$ is the planar radial distance vector from the reference to the source point on the ground plane, $\hat{\theta}$ is the zenith angle unit vector and $J_0(\cdot)$ the zero-th order bessel function. This corresponds to a Hankel transform, but the finite upper limit means that there is a rectangular window function of size equal to the radius of the circular plane, which will cause the ground plane radiation wavenumbers to appear. We will use an isotropic spherical wave source at $z = 0.5\ m$, as a theoretic example for the illumination of the ground plane, since the diffraction effect we want to examine is in the far-field of the antenna where the illumination is roughly dependent on $1/\rho$. We also ignore its phase term for simplicity. Gain patterns at zenith of the total radiated field $\vec{E}_t = \vec{E}_i + \vec{E}_a$ (taking also into account the direct isotropic radiation by the spherical source on the upper hemisphere) were calculated for this theoretic case.

4.1.2 Numerical simulations of SKALA4.1

For an antenna such as SKALA4.1, it is expected that when placed at a central position and illuminating the ground plane, a ripple of the same periodicity as the theoretic example will appear. For off-center antenna placement on the ground plane, the illumination is more complex, the geometry is not azimuthally symmetric and we cannot intuitively expect the presence of this wavenumber undistorted. We must also note that SKALA4.1 has an electrical connection to the ground plane and does not always illuminate in the far-field (see schematic of Fig. 4.1, left), which makes the results of a full-wave solver different than if we attempted to use the SKALA4.1 far-field pattern as an illumination in Eq. (4.1).

As our first step in this numeric analysis, we simulate in Fig. 4.2, right, the pattern of a SKALA4.1 placed on a finite $a = 21\ m$ and infinite radius ground plane, and excite its Y-polarization. We use FEKO amd Galileo, and the Method of Moments solver for both. Moreover, to test the position dependence, we choose three positions, termed "center", "middle" and "edge", corresponding to the positions of antennas #120, #132, #130, respectively, of the next section (see Fig. 4.1, right,

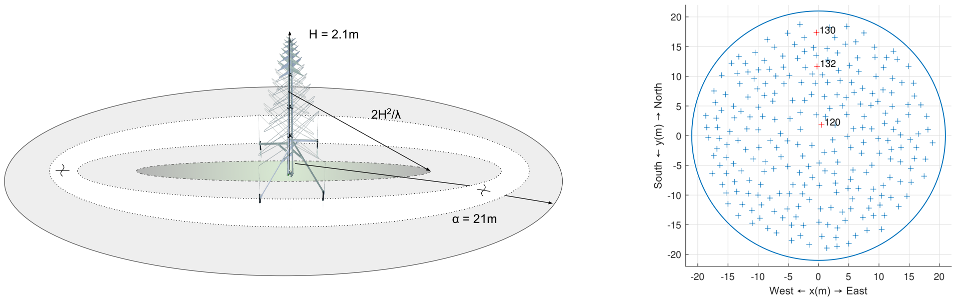

(a) **(b)**

Figure 4.1. (a): SKALA4.1 geometry, centrally placed on a 42m diameter ground plane, which is colored differently at its intersection with the near-to-far field sphere (not at scale), (b): AAVS2.0 two dimensional layout and ground plane perimeter, highlighted by crosses are all the antennas, while the examined ones are colored red and their identifying number is given.

but isolated on the ground plane for this section), and focus on 50-100 MHz with a 2 MHz step.

In Fig. 4.2 on the right, we first notice the gain at zenith results for the centrally placed antenna of either solver (blue curves). We can recognize a qualitatively similar ripple as in the theoretic spherical wave source case, as far as periodicity is concerned, although it is seen here to have a larger amplitude (since SKALA4.1 is more directional by design). There is again a negative slope owing to the reflection phenomenon by the ground plane of the antenna backscattering, which has initially been observed in the infinite ground plane simulations, as analysed in [9].

We then examine the gain response at zenith for all the antennas chosen, including comparisons between the two solvers used. In Fig. 4.2, right, it can be observed that all finite ground plane patterns exhibit more complex periodic deviations from the infinite ground plane solution, indicating that the main contribution of the ground plane across frequency is different than the zero-th order Hankel wavenumber. The two solvers give similar results. It is also evident that the periodicity away from the center is not the same, and not always centered around the infinite ground plane curve (e.g., the edge antenna has a systematic offset).

To look for the existence of periodic characteristics, we will use a Discrete Fourier Transform (DFT) on the data[1]. Since we are using a sampling rate of $f_s = 2$ MHz and $N = 26$ frequency points, the length-domain sampling will be $\ell_s = \frac{c_0}{N f_s} = 5.77$ m. By applying the DFT on real-number data as are the gain ratios between infinite and finite ground plane solution data ($R(G)$ on the Fig. 4.3 y-axis) we get a symmetric discrete spectrum, so we keep only the one-sided result, as in Fig. 4.3. We then normalize these amplitudes with respect to maximum so that the theoretic result of Fig. 4.2 is comparable to the SKALA4.1 simulations.

---

[1] The most appropriate would be a Discrete Hankel Transform, but since the data is band-limited, the complexity of this method to interpret such data is higher, so it will be the objective of future studies. Our implementation here was based on the relevant Matlab function utility `https://ch.mathworks.com/help/signal/ug/discrete-fourier-transform.html`

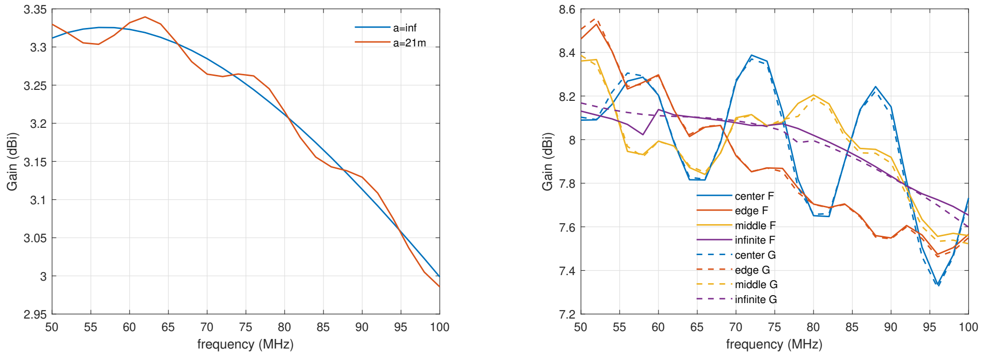

(a) **(b)**

Figure 4.2. Left: Gain at zenith in dBi, radiation by a circular ground plane of infinite and finite radius $a = 21\ m$ illuminated by an isotropic shperical wave source at height $z = 0.5\ m$, Right: Simulated gain at zenith in dBi, of a SKALA4.1 antenna placed on 3 positions of both infinite and finite ground plane cases, using FEKO ("F" in label) and Galileo ("G" in label).

We can now assess how close the amplitude peaks of each case approach $L = 23.07$ m, which is the fundamental length that the point source solution peaks at (as expected, close to our radial length $a = 21$ m highlighted in red), or what multiple of this fundamental length they correspond to, by examining the discrete spectrums of Fig. 4.3a. It can be seen that for the central antenna the highest peak is present at $0.75L$, while the one which deviates the most is the edge antenna, whose fundamental peak lengths seem to be $0.25L$ and $0.5L$ (descending order), indicating that the distance from the edge is interpreted as the effective radius "seen" by the diffraction integral. Finally, the middle antenna has 2 peaks at $0.5L$ and $0.25L$ (descending order), leading to the same conclusion for its diffraction properties.

4.1.3 SKA-Low station: ground plane effect in a closely packed array

Emdedded Element Patterns

As mentioned above, a SKA-Low station consists of 256 SKALA4.1 antennas, arranged in a quasi-random configuration as in Fig. 4.1 on the right, which shows the AAVS2.0 layout. The pattern of each antenna when excited, while all other antennas are passive, is an Embedded Element Pattern (EEP) and differs from others due to the antenna mutual coupling being irregular. We simulated 3 such patterns in the same frequency range as before, exciting them with unit amplitude and a 50 Ω source impedance while also terminating the passive antennas with 50 Ω. Since the antenna station is large, the addition of a 42m ground plane makes the problem computationally more expensive, so we use a 3-step approximate method implemented in the Galileo solver already known to speed up the analysis of large electromagnetic structures without compromising accuracy [94]. This method is based on the approximation of decoupling the computation of currents between

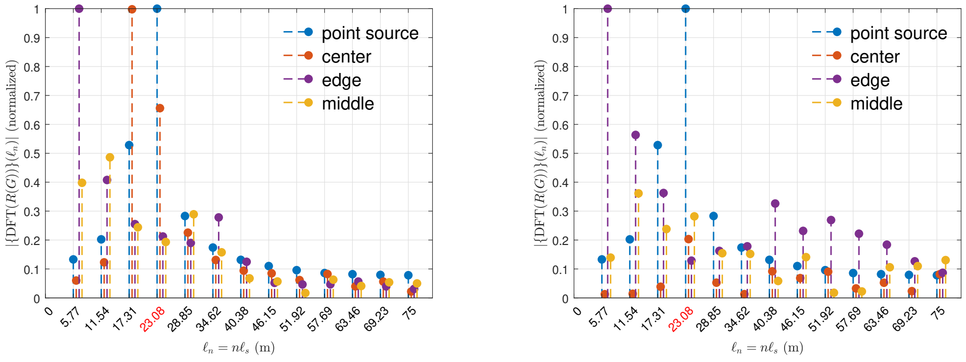

(a) **(b)**

Figure 4.3. (a): DFT amplitudes of the gain ratio $R(G)$ between infinite and finite ground plane solution patterns, for all 3 isolated antennas of Fig. 4.1 and the theoretic source of Fig. 4.2. The sampled lengths are $\ell_n = n\ell_s$, and we also normalize the vertical axis to its maximum, (b): Same as left panel, but for the embedded antenna patterns and the same theoretic source data.

antennas and ground plane, and can be summarized as follows:

1. The currents on the array are computed with a full-wave solution of the MoM, using an infinite ground plane through its reflection
2. These currents are then used to illuminate the finite ground plane, thus decreasing the dimensionality of the problem to the unknowns of the now meshed plane
3. The radiated electric field components of both structures are superimposed

Fig. 4.4a presents the selected EEP gains at zenith for the full-station with a finite ground plane in comparison to the corresponding ones computed with an infinite ground plane. We can see in this plot that the mutual coupling disturbs the patterns across the whole frequency range, with a number of mutual coupling related gain drops of 2-3 dB in magnitude. Usually, the EEP distortion is averaged out when forming the beam from all of them, however there are frequency regions where glitches of not random nature occur and therefore they are still present in the station beam as investigated in [95]. The finite and infinite ground plane cases differ by less than 1 dBi and this difference is fluctuating between positive and negative values. To acquire an estimate of any periodicity on the ratio between finite and infinite ground plane cases, we present the normalized DFT amplitudes as has been done in the isolated case, in Fig. 4.3b. The central antenna, #120 in AAVS2.0 now peaks at the fundamental length L, even with some slight peaks elsewhere. Antennas #130 and #132, as with their isolated "middle" and "edge" counterparts, have a more complex shape: notably, we identify that both of them have a much more spread-out spectrum even if they mostly retain their peak components inherited from the isolated antennas.

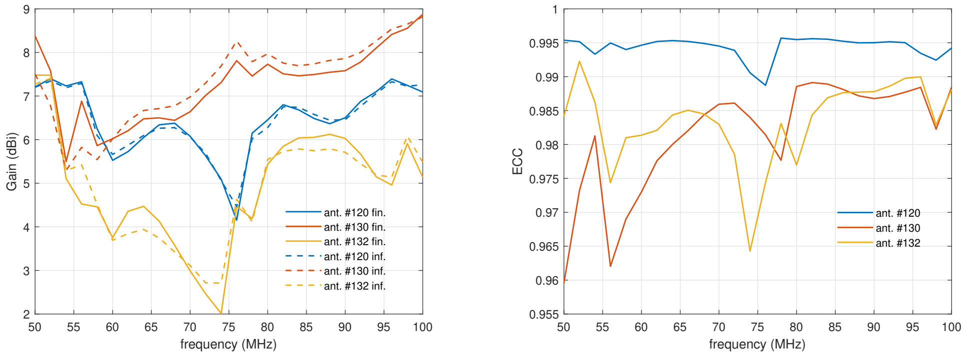

(a) **(b)**

Figure 4.4. (a): Simulated gain at zenith of EEPs in AAVS2.0 using Galileo, for all 3 antennas of Fig. 4.1, right panel. Included here are also the same quantities for the infinite ground plane solution, (b): Envelope Correlation Coefficient (ECC) over frequency for the same three AAVS2.0 embedded antennas.

Next we also present the Envelope Correlation Coefficient (ECC), calculated between the infinite ($\vec{E}_1(\theta,\phi)$) and finite ($\vec{E}_2(\theta,\phi)$) ground plane solutions. This coefficient is defined as:

$$\mathrm{ECC}(\vec{E}_1,\vec{E}_2) = \frac{\left|\int_0^{2\pi}\int_0^{\pi}\vec{E}_1(\theta,\phi)\cdot\vec{E}_2^{*}(\theta,\phi)d\theta d\phi\right|^2}{\int_0^{2\pi}\int_0^{\pi}|\vec{E}_1(\theta,\phi)|^2 d\theta d\phi\int_0^{2\pi}\int_0^{\pi}|\vec{E}_2(\theta,\phi)|^2 d\theta d\phi} \tag{4.2}$$

and makes use of the full complex valued electric field patterns $\vec{E}_1$, $\vec{E}_2$ over the 3D sphere to evaluate their similarity. For the selected antennas of the AAVS2.0 station, we calculate this coefficient using both electric field E_θ and E_ϕ quantities and present the results in Fig. 4.4b. Antenna #120 seems to best follow its infinite ground plane performance. In contrast, the middle and edge antennas have the most disturbed coefficients. It is noteworthy though that all three EEC drops are centered around the mutual coupling glitches identified at 55 MHz, 77 MHz in [95], and 98 MHz, showing that this effect can be volatile depending on the ground plane size. Due to the complexity of both the ground plane ripple and the mutual coupling phenomena, they cannot be isolated and quantified separately in terms of the ECC, but these values are always over 0.96 so the amplitude of each EEP beam volatility with respect to the ground plane being finite or infinite should be limited.

Station beam

In this section, we will examine the station beam for some of the frequencies in the 50-100 MHz range. We will use the EEPs to construct the total weighted electric field response, as well as the S parameters in order to calculate the input power. The S-parameters used will be those of the infinite ground plane solution. We have the station beam electric field expressed as:

$$\begin{pmatrix} E_{st,\theta}^{Z_g} & E_{st,\phi}^{Z_g} \end{pmatrix} = \bar{w}_g^T \cdot \begin{pmatrix} \bar{E}_\theta^{Z_g} & \bar{E}_\phi^{Z_g} \end{pmatrix} \tag{4.3}$$

where the overbar quantities are 256 × 1 column vectors, the superscript is used to indicate EEPs calculated with the $Z_g = 50\ \Omega$ termination and the voltage weights are all unit, $\vec{w}_g = (1, \ldots, 1)$. The radiated power $P_{rad}^{Z_g}$ is calculated by integrating the far-field intensity over the 3D sphere as:

$$P_{rad}^{Z_g} = \frac{1}{2\eta_0} \int_0^{2\pi} \int_0^{\pi} (|E_{st,\theta}^{Z_g}|^2 + |E_{st,\phi}^{Z_g}|^2) r^2 d\theta d\phi \tag{4.4}$$

In Fig. 4.5, we present (in dBi) the station beam directivities at the E- and H- plane of an AAVS2.0 layout station using the above approach and utilizing the infinite ground and finite ground solutions at 55, 65 and 77 MHz. Another curve is added for comparison, which presents the station beam by the simpler approach of multiplying the electric field of an isolated antenna by the array factor and its input power by the number of antennas, ignoring in such a way all mutual interactions. This is presented only for the infinite ground plane solution. Even though this method is close to the accurate EEP calculation, it can be seen that at the third side lobe it starts to significantly deviate. As far as the maximum value is concerned, at 55 MHz a deviation of 0.7 dB of the EEP solutions with respect to the array factor method. This means that the station beam is not significantly compromised by the mutual coupling at this glitch frequency, whereas at 77 MHz the deviation is even less significant. The finite ground plane station beam gains are in excellent agreement with those of the infinite ground plane solution. The lower panels present the difference between finite and infinite ground plane solutions normalized to the maximum of the infinite case, which fall off from a peak value of about 1% at zenith.

This work has been submitted by the author of this thesis and collaborators in the “International Journal of Antennas and Propagation" and is currently under review [96].

4.2 Discrete ground plane: a quantitative analysis

It is not hard to imagine that a solid circular surface of $D = 42$ m would have been prohibitive to deploy in real conditions in terms of cost, installation and maintenance. To reach a more realistic construction plan, SKA-Low considers employing a circular *grid* instead designed to have a rectangular discretization step of 5 cm, corresponding to an electrical size of almost $\lambda/20$ at the highest frequencies of operation of SKA-Low (350 MHz), which was considered fine enough to reproduce the reflectivity of a full solid plane. One should also bear in mind that while the spacing of the grid is more crucial at high frequency, this is not the case for SKA-Low where the back radiation of the SKALA4.1 antenna at high frequency is definitively smaller than at low frequency, thus reducing the ground screen's role. So far, all EM analysis has been conducted, for the sake of running time, by assuming a solid plate. In this section, we compare simulations of such a wire mesh with respect to that of a solid surface, while we also attempt to sparsen the grid to 10cm and 30cm and assess how this would impact the antenna performance. The choice of an appropriate grid spacing, according to these results, might further reduce the cost of the ground plane implementation, without significantly compromising the accuracy of electromagnetic performance.

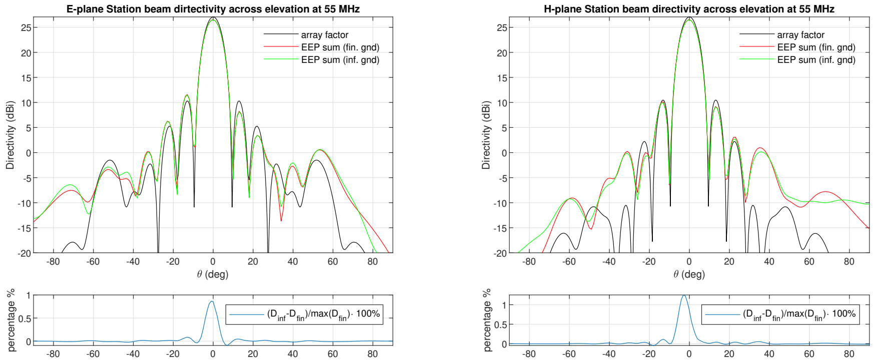

(a) 55 MHz

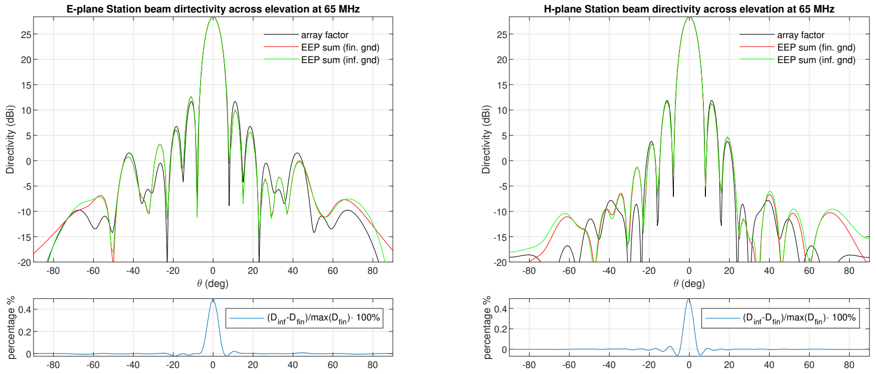

(b) 65 MHz

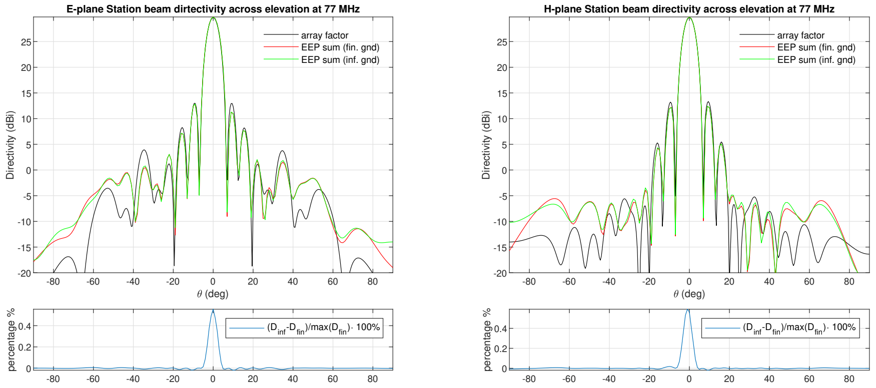

(c) 77 MHz

Figure 4.5. Station beam directivity of an AAVS2.0 layout of SKALA4.1 antennas, at 55 MHz, 65 MHz and 77 MHz (top to bottom), for E-plane (left) and H-plane (right). The full-wave EEP summed solutions of the finite and infinite ground plane cases are presented, along with an array factor approach for the infinite ground plane solution. The bottom panels show the percentage difference, normalized to the beam maximum, of the finite and infinite ground plane beams.

4.2.1 Ground plane simulations: solid surface and wire mesh

For the following simulation results, we have used the FEKO (from Altair) and Galileo (from IDS) commercial software. A reference model was created which consists of a solid circular surface and a SKALA4.1 antenna. In this section of the analysis, we omit the soil underlying the antenna and ground plane; relevant work on a previous model of the SKALA antenna has reported such results [97].

The wire mesh models are created with x-y crossing wires of radius $r_w = 2$ mm. All wire parts that are crossed by the circular circumference are deleted; we only keep those that create squares. It is also desirable to approximate the area that connects and grounds the bottom end of the boom of SKALA4.1 as a solid square plate. The actual shape of such a plate, which serves in “hooking” the antenna to the mesh on-site, is more complicated but does not impact the electromagnetic problem. The radius of the ground plane circumference was set to R=5 m both for the solid and the gridded scenarios. This is a compromise between the actual size (21 m) and the size of grids that FEKO can unite as geometry parts; there is no trivial way to connect the numerous crossing wires without intensive geometric operations. Attempts to create the full grid by such operations resulted in waiting times of more than a day, which were then terminated. An image of the 10 cm × 10 cm wire mesh model is shown in Fig. 4.6. A zoom at the central point also shows the touching part between antenna - ground mesh.

The wire grid models that were tested were of 3 discretization steps: 5 cm, 10 cm and 30 cm, which we call small ($\lambda/17$ at 350 MHz), intermediate ($\lambda/8$ at 350 MHz) and large ($\lambda/3$ at 350 MHz), respectively. The frequencies that were tested are: 60, 100, 200 and 350 MHz, that cover very sparsely the range applicable for SKA-LOW. In more detail, 60 MHz is slightly higher than the lower extreme where the antenna is badly matched, 100 MHz is about the limit of the dense regime, 200 MHz is the middle of the SKA-Low band and 350 MHz its higher extreme. The quasi-90° symmetry of the antenna (and the perfect such symmetry of the ground plane) allow us to examine the results testing only one of the examined polarisations and terminating the orthogonal one at 50 Ω.

We present in Fig. 4.7 the results of gain (in dBi) of a SKALA4.1 antenna placed on each of the ground planes (grids) and excited at its Y port, for the E-plane and H-plane cuts. The results are with respect to the zenith angle θ (truncated at 70° to compare the 2 planes in the same dynamic range) and at the 4 frequencies presented above. It can be seen that the large spacing diverges in all cases (especially at lower frequencies) from the ideal values; it is actually included as the “bad” case. The small spacing (currently employed) performs excellent for all frequencies, while the intermediate one presents minor differences. These are found at the highest frequencies (200 and 350 MHz), where the grid spacing is also a multiple of more wavelengths. The gain for angles closer to the zenith are affected more by the grid spacing. At 60 MHz, the vicinity of the antenna active region (excited dipoles) to the interface between antenna and ground plane likely makes the antenna patterns more sensitive to the gridding/solid connection.

As a validation of the accuracy of the previous results, we present the comparison of some of the FEKO gain results with the Galileo-computed corresponding ones. We choose 100 MHz and 350 MHz; at 60 MHz, there were no results computed

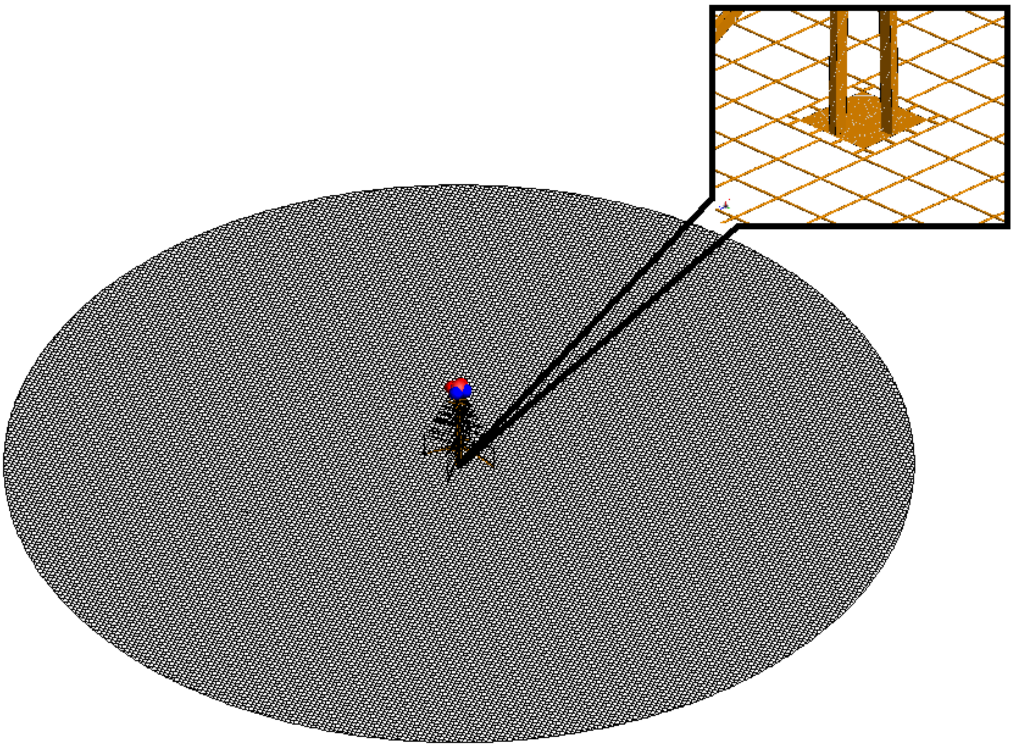

Figure 4.6. A SKALA4.1 antenna placed on a square grid of wires of radius re=2 mm, and a circumference of radius R=5 m. Also shown in a zoomed window is the part at z=0 m where the antenna and wire grid are touching.

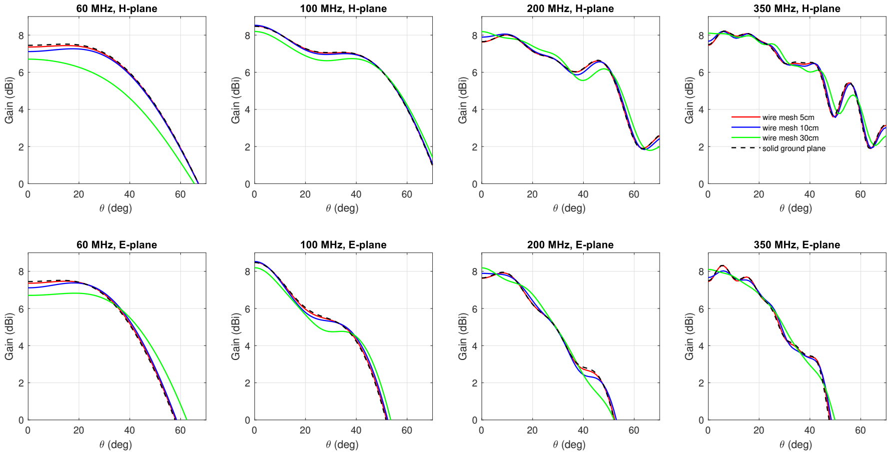

Figure 4.7. H-plane and E-plane cuts across zenith angle of the gain response in dBi, for a SKALA4.1 antenna placed on 4 different kinds of ground planes (3 grids plus 1 solid). The results are for 4 different frequencies.

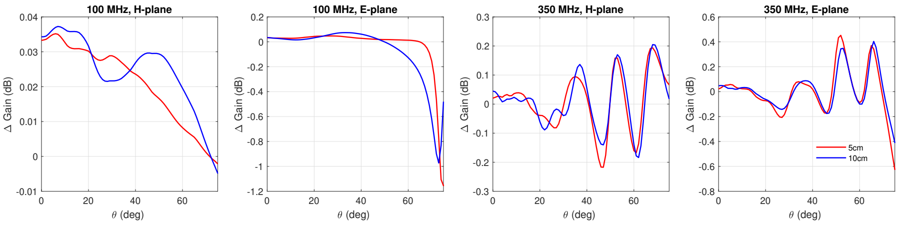

Figure 4.8. Differences in dB between results generated using FEKO and Galileo software, across zenith angle for the H-plane and E-plane cuts.

with Galileo, while at 200 MHz the differences are always less than 0.1 dB, which is insignificant. Fig. 4.8 presents the dB differences of patterns from the 2 solvers. We note that E-plane differences are more acute and at 100 MHz, they diverge for high zenith angles to -1 dB. However, some systematic agreement between the small and intermediate grid step suggests that this is due to the slightly different SKALA4.1 models used in each solver, apart from their intrinsic differences in implementing the Method of Moments.

4.2.2 Including the soil dielectric parameters: dry and wet conditions

In this section, we will consider the semi-infinite soil volume beyond and under the ground plane as described by some set of dielectric permittivities ϵ_r and conductivities σ, for two cases of conditions representing dry and wet soil. Both of these sets have been measured in 3 certain frequencies (50, 160 and 280 MHz) in [98], and interpolated in the frequencies used in this study. These parameters are collected in Tab. 4.1. As per FEKO's requirements, the solid ground plane was elevated at a minimum distance of 1 mm above the soil surface so that mesh triangles don't touch onto it; this ensures that currents can be impressed on an infinite surface, otherwise surfaces touching to meshed parts cannot be treated with the standard impressed current approach used by FEKO.

condition ↓	freq. →	50 MHz		160 MHz		280 MHz	
dry ($\epsilon_r \vert \sigma$)		3.9	0.0007	3.7	0.0018	3.7	0.0022
wet ($\epsilon_r \vert \sigma$)		17.8	0.1	14.8	0.11	14.4	0.11

Table 4.1. Relative dielectric permittivity ϵ_r (dimensionless) and conductivity σ (in S/m) at the 3 measured frequencies for dry and wet soil conditions. The values used to simulate the frequencies examined in Fig. 4 are linear interpolations of the listed values.

We will present our results in the 4 frequencies examined also in Sec 4.2.1, omitting the large spacing mesh since it has already been proven to be insufficient for screening purposes. Fig. 4.9 contains these plots for both dry and wet conditions. The level of gain at zenith is again affected the same way by increasing the spacing, meaning that some of the power “leaks” to the soil (it is now considered in the losses, though). Furthermore, at least at 200 MHz and higher, the antennas patterns are

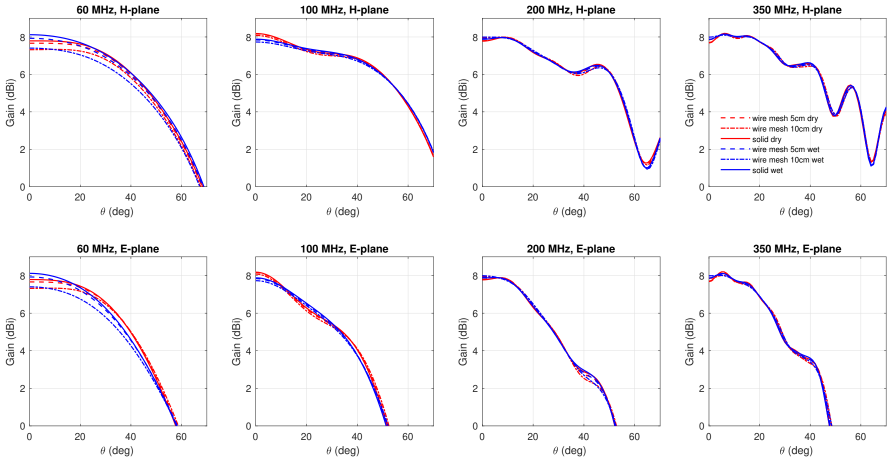

Figure 4.9. H-plane and E-plane cuts across zenith angle of the gain response in dBi, for a SKALA4.1 antenna placed on the solid, small step and intermediate step grid acting as a ground plane. The dry and wet conditions values are used to simulate the soil volume.

largely decoupled from the terrain conditions. What is important to distinguish between dry and wet conditions are certain zenith angles where the curve presents a "bend" (or saddle point). These features can vary in amplitude depending on the dielectric parameters since they play a role in the diffraction phenomenon at the transition from perfect to lossy conductor [94], [93]. We can see such features at 100 MHz on 20°, at 200 MHz on 20°, 40°, and at 350 MHz on 5°, 10°, 25°, 40° (effect present on both planes).

Another useful comparison is between the patterns simulated in this section, with the ones without the inclusion of soil. Since the wet conditions are the most divergent ones in terms of dielectric parameters, we will compare the sets of wet soil patterns with the free-space patterns of Sec. 4.2.1. Fig. 4.10 presents this comparison, in which we see significant deviations, especially for the 2 lowest frequencies. It is worth mentioning that the soil makes the ripple-like diffraction pattern less in amplitude, which is a positive aspect for the smoothness of the curve and the instrumental response as a whole, in all of the ground plane cases examined.

4.2.3 Gain response across SKA-Low frequency band

In this section, some results are presented focusing on specific pattern points of the antenna and ground plane (or mesh) system examined in the previous sections. We have selected the zenith ($\theta = 0°$), and the E-plane and H-plane cuts at zenith angle $\theta = 45°$ ($\phi = 0°$, $\phi = 90°$ respectively), and tested the frequency response from 60 MHz to 350 MHz using a 10 MHz step. The frequency point of 50 MHz was excluded since it is degenerate in gain owing to the small size of the ground plane. All the in-between points with a frequency step of 1 MHz, were filled using a standard cubic interpolation to facilitate the visualisation; in general, the trend observed in all curves agrees with the simulated gain of [9]. It is interesting to note in this plot a couple of findings:

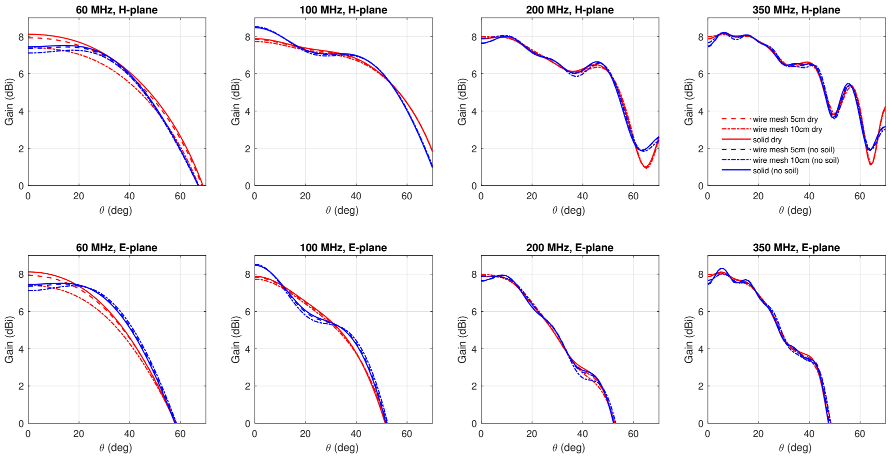

Figure 4.10. H-plane and E-plane cuts across zenith angle of the gain response in dBi, for a SKALA4.1 antenna placed on the solid, small step and intermediate step grid acting as a ground plane. The wet-soil conditions is compared to the no-soil model of Sec. 3.

- The zenith response, when interpolated, presents faster variability with respect to the E-plane and H-plane 45° points. Even though the interpolation might not accurately represent the pattern, the ground plane is certain to affect the zenith direction in a stronger way due to the diffraction [4].

- There are various frequency points where either the small or the intermediate step grid better approximate the response of the antenna placed on a solid ground plane. It can be concluded that differences on the level of 0.5 dB, as are the higher ones seen here, are inevitable for any such mesh discretization of the solid surface of D=5 m.

- The small step wire mesh model agrees at zenith and at 45° H-plane consistently better with the solid plane, with respect to the intermediate step one.

Finally, we present in Tab 4.2 the RMS/Mean values calculated by the curve data, along all 3 sets of pattern points, between small step wire mesh and solid plane, as well as between intermediate step wire mesh and solid plane. These confirm the last 2 points made above. Importantly, the H-plane seems to be reproduced by both spacings.

This work has been published in a SKAO technical report by the author of this thesis and collaborators [99].

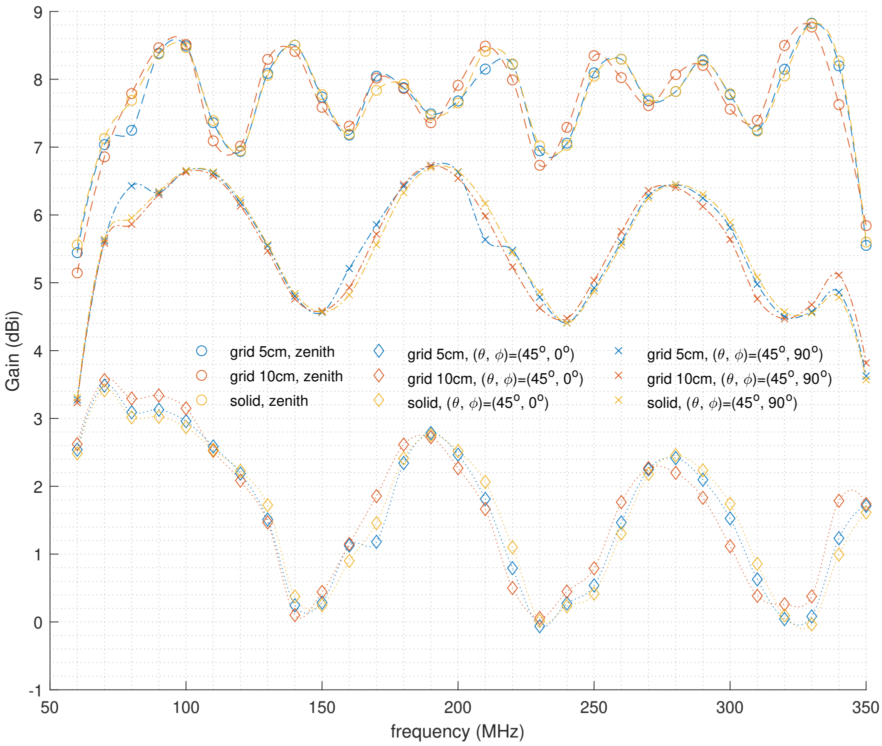

Figure 4.11. Frequency response of the gain (dBi) of a SKALA4.1 on the solid plane model, as well as the small and intermediate step meshes, at 3 points corresponding to the zenith and the E-plane and H-plane cuts at zenith angle $\theta = 45°$. The points in-between the annotated (simulated) ones are filled using a cubic interpolation.

models ↓	direction →	zenith	$\theta = 45°,\ \phi = 0°$	$\theta = 45°,\ \phi = 90°$
small step wire - solid		0.025	0.031	0.04
interm. step wire - solid		0.055	0.073	0.033

Table 4.2. RMS/Mean value at different directions of the antenna gain pattern calculated between *small* step wire mesh and solid plane, as well as between *intermediate* step wire mesh and solid plane.

Chapter 5

Array Mutual Coupling of SKA-Low: lower frequency *“glitches"*

5.1 SKALA4.1 array mutual coupling

5.1.1 Overview of array configuration modelling and optimization

Mutual coupling in antenna clusters or arrays is quite a well known phenomenon. In applications such as massive Mutiple-Input-Multiple-Output (MIMO) systems, it can even be harnessed to improve the channel throughput, i.e. the data rate of a telecommunications link [100]. Usually, though, mutual coupling is ignored in applications where a sparser array configuration is employed, or the full knowledge of the antenna beam is not an impactful parameter in the design of the final system. For low-frequency arrays used in radioastronomy, and particularly SKA-Low, both these conditions are violated.

The problems that mutual coupling induces in such arrays are various. At a first glance, one can confirm that if there is a systematic effect that cannot be randomized out by a pseudo-random array configuration, the drop of gain within the field of view - and subsequently the effective area of the array - leads to a decrease in its sensitivity. The deterioration of the array matching properties can also contribute to that, since the SEFD (System Equivalent Flux Density) depends on the antenna multi-port impedance [101]. Preliminary sensitivity measurements in the AAVS2.0 prototype SKA-Low station have also highlighted the effect of mutual coupling [13].

Most importantly, mutual coupling features, which usually are sharp due to spurious excitation of unwanted modes, disrupt the spectral smoothness of the antenna patterns [102]. This is connected to the remarks in Ch. 3 for the narrow-band glitches, but can, in the case of mutual coupling, hinder calibration in a much more significant way, due to the features’ magnitude, as well as the wider bandwidths affected. We note, for example, the complications of the spatial (or delay) power spectrum measurement of the Cosmic Dawn - Epoch of Reionization when a beam suffers first-order coupling effects [103], where computational simulations can assist in such mock-measurement pipelines. Perturbed beam models due to mutual coupling can also result in larger calibration errors [104].

Recent efforts have been made to optimize the layout of the AAVS2.0 station in an ad-hoc way, retaining its pseudo-random characteristics. Repositioning some antennas according to exclusion zones surrounding their vicinities in a 16-element array [95], as well as repositioning according to statistic measures of both the interelement distances and alignment angles in the full-AAVS2.0 [105] have yielded improvements. The need to avoid unwanted close spacings resulting from the randomization process can also be tackled by other, more regular layouts e.g. the Vogel layout [15]. The Voger layout, which ensures disalignment of the antennas on the 2D plane, some improvements are seen in the effective area [106] and IXR of the station [107], but other severe effects have emerged due to repeated intra-station baselines [108]. The persistence of the problem and especially the immunity of its central frequency hint to fundamental antenna properties as responsible for its manifestation.

5.1.2 A baseline two-antenna configuration: simulation and experimental results

In the following subsections of this chapter, we mainly focus on a configuration of two antennas which we call *baseline* to showcase the mutual coupling phenomena. We are keeping the two antennas on the same plane and their polarizations aligned on a nominal coordinate system, which is a requirement set by both mechanical constraints as well as easier polarimetric analysis. Such a configuration can be parametrized by 3 non-trivial variables, in terms of its electromagnetic response:

1. The distance between the center of the antennas D_0
2. the angle between this distance vector and the plane x-axis, ϕ_0
3. the receiving and terminated polarizations

A geometric image of the *baseline* configuration is seen in Fig. 5.1a. Let us define its FEKO model composed of two SKALA4.1 antennas laid over an infinite perfect electric conductor, aligned in the x-axis. Since the instrument is used only for reception, we prefer to label the elements as *receiving* and *terminated* element, respectively. The simulation (in transmit) is conducted by exciting the port of the receiving element, while the non-excited ports are terminated with 50 Ω loads.

Owing to the asymmetry of the excitation placement, the EEP is generally tilted from the zenith direction; this is evident in Fig. 5.1b where the E-plane EEPs for several frequencies between 67 MHz and 85 MHz are reported, when $D_0 = 1.5$ m, $\phi_0 = 0°$. Moreover, while the curves are rather close to each other for most of the reported frequencies (dashed lines), the trend is lost around 77 MHz where highly perturbed patterns appear (solid lines), with also a deep null at zenith at 77 MHz (about -13 dB with respect to the maximum). This picture highlights the sharp nature of the resonance phenomenon. As described in [67], this is a systematic effect which is not mitigated by the pseudo-random distribution of the antennas.

In Fig. 5.2a and 5.2b we also reproduce Fig. 2 of [95]. These plots show the volatility of the configuration of Fig. 5.1a with respect to its two geometric parameters.

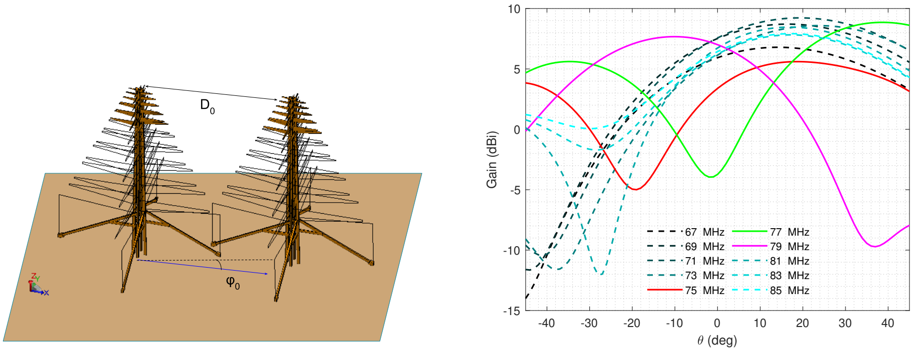

(a) **(b)**

Figure 5.1. (a): Ideal FEKO model of two SKALA4.1 antennas placed at a distance of $D_0 = 1.5\ m$ (center-to-center) on the x-axis ($\phi_0 = 0°$). Ant.1 is the *receiving* (X-polarized reception) and Ant.2 is the *terminated* antenna (50 Ω termination). Both are placed on an infinite PEC ground plane, (b): E-plane EEPs of the two-antenna array, for a set of frequencies. Negative zenith angles θ are towards the terminated antenna.

We can see that by increasing the distance D_0 the amplitude of the features at 55 and 77 MHz is moderated, but the frequency is almost unaffected. On the other hand, when ϕ_0 is increased, a similar but slower trend is seen: in particular, some angles can lead to worse spectral structure of the glitches. Again, the frequency diversity is limited to 1-2 MHz. Since the system is almost symmetric by mirroring (with minor deviation due to the cross-feeding by the boom), if Ant. 2 was receiving and Ant. 1 was terminated we would observe similar phenomena; that extends to both antennas as receiving due to their similar EEPs adding up to the total response.

For the experimental test describing this phenomenon, an array of two SKALA4.1 antennas 1.5 meters apart (center-to-center) was set up as shown in Fig. 5.3a. The two SKALA4.1 antennas were mounted on two square-grid ground planes of similar dimensions. Both the grids had a mesh size of 25 mm and were electrically connected with each other. The Low-Noise Amplifier (LNA) on top of the antenna was replaced by a passive connection to avoid non-linearity phenomena induced by radio frequency interference in the outdoor measurement field. The receiving element was connected to a Agilent E4402B Spectrum Analyzer (SA) through a 60 m long LMR400 cable, whereas the remaining three ports were terminated with 50 Ω loads. The measurement is focused in the second mutual coupling phenomenon, centered at 77 MHz, since the hardware available was more robust in this range.

The measurements were performed with a quadcopter implementing Real-Time Kinematic (RTK) positioning, with a high degree of accuracy. As far as the RF transmitter is concerned, the UAV carried a 2 m long dipole fed by a Valon 5015 frequency synthesizer and a balun. The synthesizer produced a stepped swept-sine signal within the range 66-85 MHz in 0.1 MHz steps with a duration of 1.5 seconds each. The chosen parameters result in 191 frequency points and 5 minutes of sweep duration. During this lapse, the UAV remains steady in the sky at 60 m altitude above ground level at the zenith of the receiving element and a Spectrum Analyzer measures the received power. The pattern was then computed following the approach

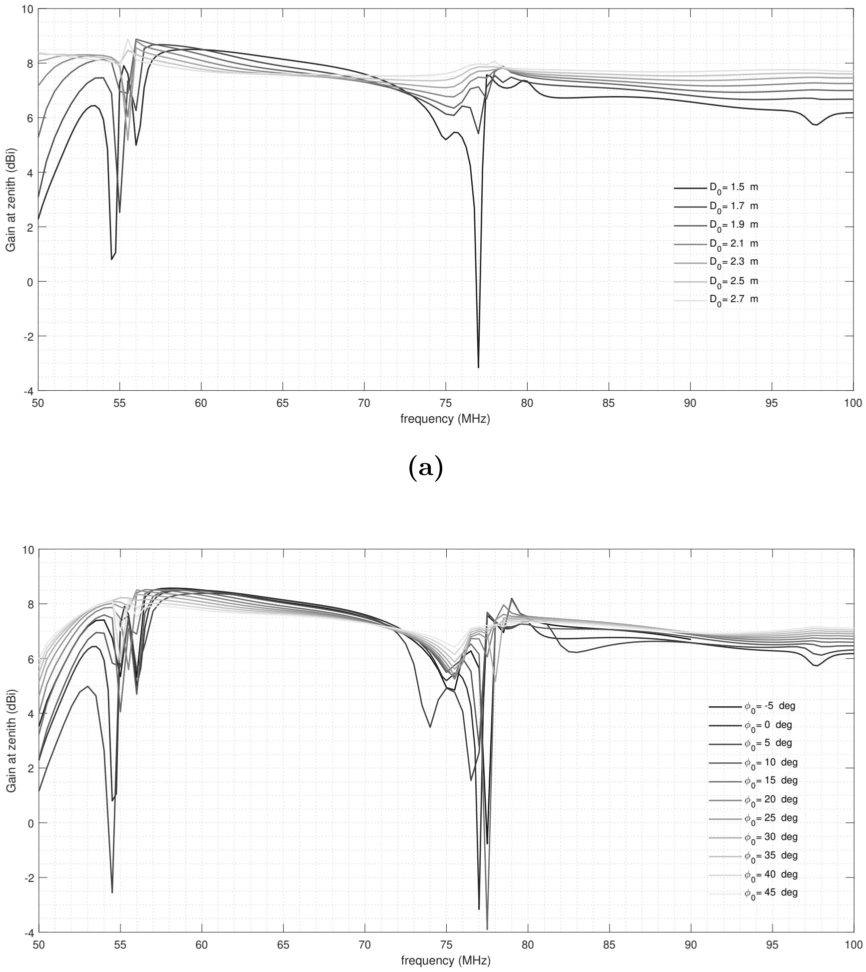

(a)

(b)

Figure 5.2. (a): Gain at zenith (dBi) over frequency of the two-antenna system of Fig. 5.1a for various D_0 at $\phi = 0°$, (b) the same for various ϕ_0 at $D_0 = 1.5$ m.

of [109] based on the Friis equation. The resonant frequency of the transmitting dipole is found within the chosen frequency range, and the impedance mismatch factor has been simulated and compensated for.

Fig. 5.3b shows the measured (orange curve) and simulated (gray envelope) zenith gain variation versus frequency. It should be pointed out that the EM model was, for this plot, carefully refined to reproduce with high fidelity the real setup. In particular, two solid, finite rectangles were now modeled as perfect electric conductors and placed underneath the antennas and on the top of the surface of a semi-infinite dielectric medium to simulate the soil. This soil volume was included in the solution by means of the Sommerfeld integral equation, which, in FEKO, is hybridized with the MoM used for the mesh parts. We then varied the soil complex permittivity to account for the margin of error related to its approximate modeling. The gray envelope of Fig. 5.3b shows the simulated results for 5 sets of relative permittivity

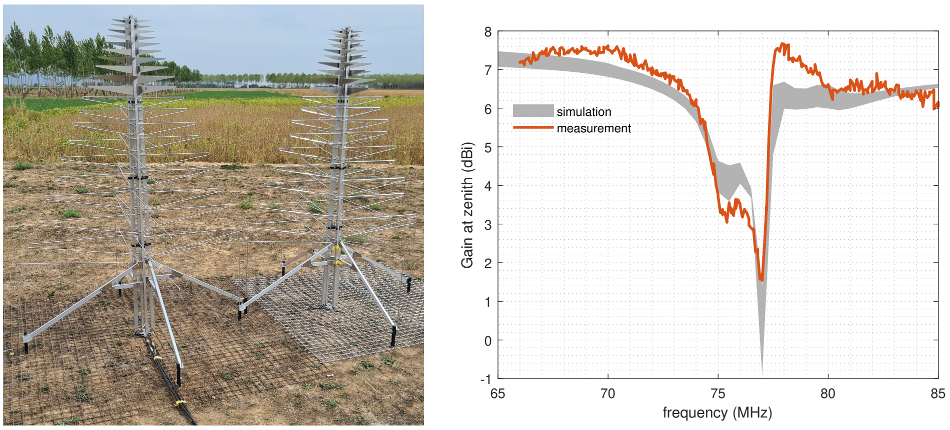

(a) **(b)**

Figure 5.3. (a): Two adjacent SKA-Low elements over mesh ground plane. *Receiving* element on the left, *terminated* element on the right, (b): Measured (orange) curve and simulated (gray envelope) zenith gain versus frequency. A number of 5 sets of (ϵ_r, σ) was used for the simulations. The measured curve is normalized to the simulated one (*baseline* model) at 66 MHz.

ϵ_r and conductivity σ, and is defined by the min/max of these 5 models at each frequency. For our *baseline* model, we used a relative dielectric constant of $\epsilon_r = 4$ and a conductivity of $\sigma = 10^{-3}$ S/m, representing mainly dry moisture content of sandy clay loam [110]. To test deviations from these conditions, the more volatile conductivity was scaled by a factor of 5 (i.e., 5×10^{-3} S/m and 2×10^{-4} S/m) while retaining $\epsilon_r = 4$, whereas the dielectric constant was scaled by a factor of 2 (i.e., 2 and 8) while retaining $\sigma = 10^{-3}$ S/m.

For further check of the simulated EEPs, Fig. 5.4a and 5.4b show the normalized E-plane EEPs for a minimal set of two frequencies chosen within the unperturbed frequency band (70 MHz) and where the mutual coupling effect is maximum (77 MHz). The simulation envelope corresponding to the extremes of all sets of soil parameters (gray area) covers all the zenith angles whereas the measured curve (orange) is limited to the field of view covered by the UAV flight (±60°). While the curves almost perfectly agree in the unperturbed frequency of 70 MHz, an angular offset is present at 77 MHz where the mutual coupling creates a dual lobe. The distribution of radiated power showing a maximum in far off-zenith directions is a non-trivially described phenomenon, which could lead to small inaccuracies between measurements and simulations. Nevertheless, the perturbed EEP at 77 MHz is fully confirmed by such measurements (similar error levels have been reported in previous works [111]).

This work has been co-authored by the author of this thesis and published in IEEE Antennas and Wireless Propagation Letters [112].

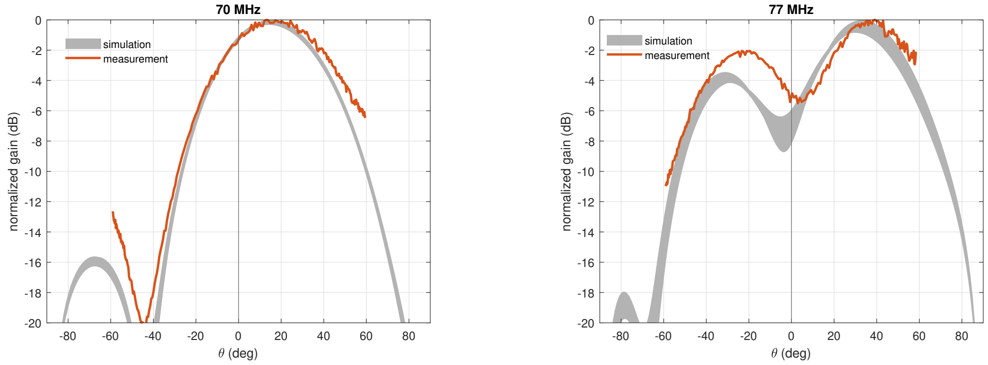

(a) (b)

Figure 5.4. Measured (orange curve) and simulated (gray envelope) normalized EEPs at 70 MHz (a) and 77 MHz (b).

5.2 A CMA approach for the two-antenna system

5.2.1 Full CMA

We focus our analysis here in the *baseline* configuration of two SKALA4.1 antennas. We consider the nominal placement at a distance of $D_0 = 1.5\ m$ on the x-axis, since we want to examine mutual coupling phenomena at the configuration corresponding to their maximum effect, which is when they perfectly align in their E-plane. It should be taken into account that, in this way, we approximately create another geometric symmetry on the problem (that of mirroring with respect to the Oyz-plane), which will certainly give rise to characteristic mode traces almost crossing, that increase the difficulty of tracking [70]. The increased complexity and size of the problem also result in FEKO's tracking routine further lacking in accuracy [113].

The simulation procedure discussed in Sec. 2.3.2 has been repeated on the antenna pair using a larger number of modes to achieve convergence. We first present in Fig. 5.5a the same zenith far-field $|e_{co}|^2$ values, starting by $M = 20$ and converging at $M = 30$ to the MoM solution. We note that the values of $|e_{co}|^2$ are lower than that of Fig. 2.7a, meaning that the radiated power is also lower. As has been shown, though, in [67], the gain remains relatively constant with respect to that of the single antenna, at the frequencies where the mutual coupling is not significant. We observe that the three distinct radiation peaks, a characteristic inherited from the active antenna, are now disturbed; due to the poor tracking we were not able to directly associate these features with their distinct modes. The CMA solutions could not be sufficiently tracked even at a post-processing stage, since it requires sophisticated algorithms [71].

As expected from Sec. 5.1.2, we identify the mutual coupling features, that discontinuously alter the smooth response, at frequencies 56 and 78 MHz ([67]). A better idea of the mechanism that drives the anomalies can be obtained by examining the cross-polarized radiation as well. We have verified at various spherical angles that the reconstruction by CMA is valid, and we show here the results for the maximum $|e_{cr}|^2$ over frequency in Fig 5.5b. This occurs almost always around $\phi = 4° - 8°$,

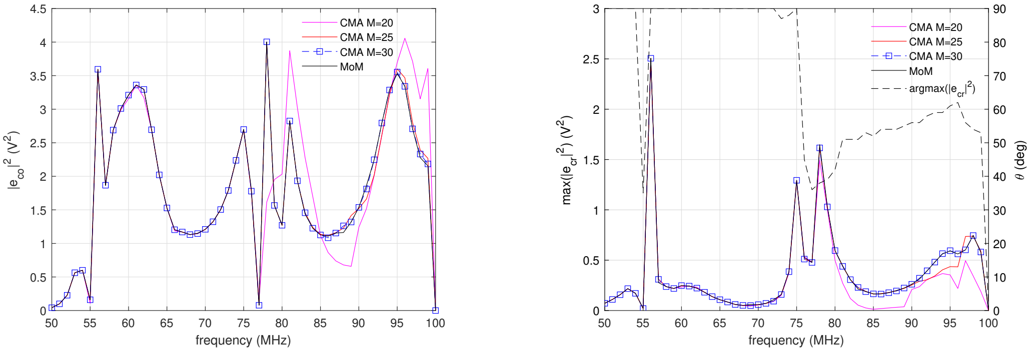

(a) **(b)**

Figure 5.5. (a): Magnitude of co-polarized electric far-field values at zenith across frequency, using MoM and CMA with $M = 20,\ 25$ and $M = 30$, (b): Magnitude of maximum cross-polarized electric far-field values across frequency, for the same CMA modes, where the elevation $\theta_{max} = \text{argmax}(|e_{cr}|^2)$ is indicated with a dashed curve and values on the right axis.

while the exact elevation is plotted with a dashed curve and values on the right axes. A rather high value of cross-polarized radiation is seen in the mutual coupling narrow-bands, which, as will further be explained, is responsible for the zenith anomalies of $|e_{co}|^2$. The reconstruction is again accurate for $M = 30$.

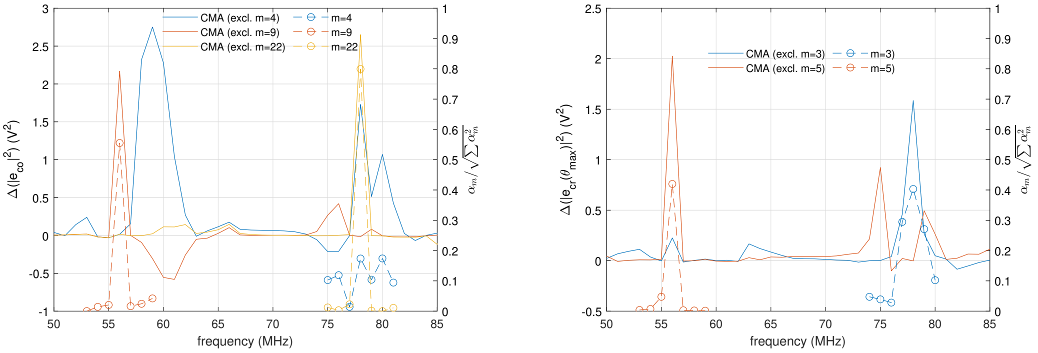

(a) **(b)**

Figure 5.6. (a): $|\Delta e_{co}|^2$ difference, at zenith, of CMA solution excluding modes $m = 4,\ m = 9,\ m = 22$ from full MoM solution using (left legend), and the respective excluded mode α_m properly normalized to ≤ 1 (right legend), (b): $|\Delta e_{cr}(\theta_{max})|^2$ difference of CMA solution excluding modes $m = 3,\ m = 5$ from full MoM and excluded mode α_m, where the θ_{max} is as in Fig. 5.5b.

Since the mutual coupling is narrow-band, we have tentatively adopted the tracked solutions as shown in Fig. 5.6a with circle-dashed lines and values on the right axis, which correspond to the $\alpha_m/\sqrt{\sum \alpha_m^2}$ (normalized to ≤ 1, in showing that those are the dominant modes in the respective narrow bands). These can be seen to correspond to spurious excitations in the respective narrow bands ($m = 4$

constituting an exception, as will be seen in the next section). To enhance the credibility of this result, we also show how the reconstructed CMA solution differs from the MoM reference solution, when these certain modes are omitted (i.e., in the sum of Eq. 2.15)). The resulting $|\Delta e_{co}|^2$ curves (labelled "excl. m=4", "excl. m=9", "excl. m=22") are presented with values on the left axis of Fig. 5.6a, resulting in better continuity of the curve at each narrow frequency band by omitting the respective mode. Since we already know that tracking outside of these bands might not be accurate, $|\Delta e_{co}|^2$ deviations outside these bands could either be artefacts or represent a contribution of the mode that does not interest us since it is obscured by all the others being summed up to a smooth curve.

Finally, in Fig. 5.6b, the $|\Delta e_{cr}(\theta_{max})|^2$ between CMA and MoM at the direction of maximum (θ_{max}) is presented, with a CMA reconstruction omitting modes $m = 3,\ m = 5$. These are the highest contributions to the $|e_{cr}|^2$ at frequencies 78 and 56 MHz, respectively, as also seen by their MWC's (the vicinity around those frequencies should again be cautiously treated due to tracking). It is apparent here that the modes describing the cross-polarized far-field glitches, are not the same as those of the co-polarized far-field. Since though the two polarizations have complementary spectral behaviour, when strong coupling is present, the pure inheritance from geometrically orthogonal parts of the antenna for these modes and in this specific case is set under question.

This work has appeared by the author and collaborators at the "European Conference on Antennas and Propagation (EuCap2023)" in [114].

5.2.2 First-order coupled modes

We will now present the connection between modes of the single antenna and modes of the system of two antennas, using the theory of coupled characteristic modes as outlined in [57]. We are going to assume the first-order approximation by considering the m-th coupled characteristic mode eigencurrent of interest as:

$$\bar{J}_m = \begin{bmatrix} \bar{J}_{m_1} \\ c\bar{J}_{m_2} \end{bmatrix} \tag{5.1}$$

where $\bar{J}_{m_1},\ \bar{J}_{m_2}$ are the interacting m_1-th, m_2-th eigencurrents of each single antenna, respectively, and c is a scalar coupling constant. It has to be emphasized that by using the coupling coefficient it is implicitly assumed that Ant. 1 exerts a perturbation on Ant. 2 [115]. This way, $c\alpha_{m_1}$ could be thought of as a new factor $\alpha_{m_2,\text{eff}}$, quantifying the first order effect as an effective MWC of mode m_2 on Ant. 2 by means of the applied excitation of mode m_1 of Ant. 1. Of course, the mutual coupling makes the interaction more complex; it cannot however result in c^2-factored excitation terms (with regard to amplitude). To better understand the far-field behavior which is closely related to the radiated power, as well as the dynamics of the system via the eigenvalues and eigencurrents, we will first focus our attention on a simple mathematical description of the phenomenon.

Let us write the m-th mode complex power as:

$$P_{rad,m}(1 + j\lambda_m) = \frac{1}{2}\begin{bmatrix} \bar{J}_{m_1}^T & c\bar{J}_{m_2}^T \end{bmatrix} \begin{bmatrix} \mathbf{Z}_{11} & \mathbf{Z}_{12} \\ \mathbf{Z}_{21} & \mathbf{Z}_{22} \end{bmatrix} \begin{bmatrix} \bar{J}_{m_1} \\ c\bar{J}_{m_2} \end{bmatrix} \tag{5.2}$$

where we have block-partitioned the MoM impedance matrix $\mathbf{Z}$ in 4 blocks considering the diagonal ones of Ant.1, Ant.2 ($\mathbf{Z}_{11}$, $\mathbf{Z}_{22}$), and the symmetric off-diagonal ones ($\mathbf{Z}_{12}^T = \mathbf{Z}_{21}$) corresponding to the antenna coupling[1]. The left hand side are all known quantities from simulation, for all m. One can develop the right hand side quadratic form and substitute for:

$$\frac{1}{2}\bar{J}^T_{m_{1(2)}}\mathbf{Z}_{11(22)}\bar{J}_{m_{1(2)}} = P_{rad,m_{1(2)}}(1+j\lambda_{m_{1(2)}}) \tag{5.3}$$

which are again known quantities for all m_1 or m_2. The unknown quantities in this formulation, with respect to readily available simulation results, are the quadratic forms:

$$\frac{1}{2}\bar{J}^T_{m_1}\mathbf{Z}_{12}\bar{J}_{m_2} = \frac{1}{2}\left(\bar{J}^T_{m_2}\mathbf{Z}_{21}\bar{J}_{m_1}\right)^T = \frac{1}{2}\bar{J}^T_{m_2}\mathbf{Z}_{21}\bar{J}_{m_1} \tag{5.4}$$

We will denote this term $P_{m_1m_2} = P_{rad;m_1,m_2} + jP_{st;m_1m_2}$, where we have named the real and imaginary parts as a coupled radiated (P_{rad,m_1m_2}) and stored (P_{st,m_1m_2}) power, respectively. The manipulation of FEKO results is quite lengthy to calculate these parameters. In essence, even when currents are requested to the simulator, those are tabulated in a form that corresponds to the total current on each triangle after summing the RWG contributions from each edge[2]. Some technical details on our method of retrieval of the RWG currents are given in App. A, in order to emphasize the possible limitations of such an analysis based on a commercial solver, but also how various numerical issues can be confronted.

The theoretical coupled system eigenvalue $\lambda_{CM;m}$ is derived from Eq. (5.2) (the same as [57, Eq. (19)] in our notation) and is expressed as:

$$\lambda_{CM;m_s} = \frac{\Im\{P_{m_s}\}}{\Re\{P_{m_s}\}} = \frac{\lambda_{m_1}P_{rad;m_1} + c_s^2\lambda_{m_2}P_{rad;m_2} + 2c_sP_{st;m_1m_2}}{P_{rad;m_1} + c_s^2P_{rad;m_2} + 2c_sP_{rad;m_1m_2}} \tag{5.5}$$

where $c_s = c_+$ or c_- defines the duality of the solution and is also given in a more complex expression [57, Eq. (17)]). We identify some special cases of this expression:

- When $c_s \ll 1$, then $\lambda_{CM;m_s} \approx \lambda_{m_1}$, so there is a dominant mode in the system which is almost the same as mode m_1 (weak coupling)
- when $c_s \gg 1$, then $\lambda_{CM;m_s} \approx \lambda_{m_2}$, so a single antenna mode is again dominating the system but it is excited in the passive antenna (weak coupling)
- when $c_s \lesssim 2P_{st;m_1m_2}/\sqrt{\lambda_{m_2}P_{rad;m_2}}$, where the square term c_s^2 can be omitted (strong coupling)

The first step in testing the first-order coupled modes theory is to pinpoint if there exist modes m_1, m_2 that are close to modes of the coupled system. These would cover the first two cases presented above and are mostly unaffected by the

---

[1] Instead of Hermitian matrices we can use transpose, since the eigencurrents are iso-phase and we can refer them to phase zero.

[2] It is reminded that now the size of the single antenna problem is 15100 BF, while that of the two-antenna problem is 30200 BF. In FEKO, it is impossible to get the full RWG vector $\bar{J}$ from the `.str` file, since it is not a supported option for CMA.

Table 5.1. Left table: eigenvalues of single-antenna mode, two-antenna mode and relative difference at 56 and 78 MHz, Right table: complex modal power of single-antenna mode, two-antenna mode and relative difference at 56 and 78 MHz

f (MHz)	λ_{m_1}	λ_m	$\left\|\frac{\lambda_{m_1}-\lambda_m}{\lambda_{m_1}}\right\|$	P_{m_1} (mW)	P_m (mW)	$\left\|\frac{P_{m_1}-P_m}{P_m}\right\|$
56	-0.489	-0.608	24.3%	0.13-j0.06	1.98-j1.2	93.7%
78	1.854	1.849	0.2%	4.86+j9.01	5.62+j10.41	13.4%
78	1.022	1.104	7.43%	4.92+j5.03	5.86+j6.47	19.7%

mutual coupling complex power (or equivalently the Z_{12} matrix), but rather are inherited from the single antenna. Examining the eigenvalues of both the single and the two-antenna system at frequencies 56 and 78 MHz, where modes $m(56\text{ MHz}) = 9$ and $m_+(78\text{ MHz}) = 4,\ m_-(78\text{ MHz}) = 22$ respectively have been seen to largely account for the coupling phenomenon, has resulted in the identification of the dominant modes $m_1(56\text{ MHz}) = 2$ and $m_{1+}(78\text{ MHz}) = 1,\ m_{1-}(78\text{ MHz}) = 5$ of Ant.1 perturbed in the presence of Ant.2. The single-antenna eigenvalue λ_{m_1} along with the two-antenna system eigenvalue λ_m and their percentage relative difference $|\lambda_{m_1} - \lambda_m|/|\lambda_{m_1}|$ for both the examined frequencies are listed in Tab. 5.1. At 56 MHz, the relative difference seems to be a quite larger perturbation of the single-antenna eigenvalue, while a more reasonable such value is calculated at 78 MHz.

The last two columns of Tab. 5.1 present the values for P_{m_1}, as well as the percentage relative difference $|P_{m_1} - P_m|/|P_m|$ to test how much of the coupled system mode complex power is "contained" in the power of the single antenna mode that is exciting the system. At 56 MHz, there is now a clear discrepancy with 93.7% of the power not being accounted for. This could mean that the perturbation of the eigenvalue and eigenpower does result in a high c (that of the third case examined above). We note a very high accuracy of 0.2% for the first eigenvalue at 78 MHz, and a 7.43% for the second one. The complex eigenpower errors remain also at reasonable values now, below 20%. The validity of the "weak coupling" was confirmed by also checking Eq. (5.2); calculations show insignificant $P_{m_1 m_2}$ values with respect to P_{m_s} for both $m_+ = 4,\ m_- = 22$ at 78 MHz (see App. A for calculation details).

For the modes identified above, some more results can be examined to characterize their behavior in a narrow-frequency band. In retrospect, even if it is not manifested in the electric far-field response due to a low MWC for the single antenna case, an “excited” mode might contribute to a strong coupling scenario with a proper coefficient c. We will focus our attention for this task around 78 MHz, due to the higher importance of that frequency [69] as well as the low errors with respect to single antenna modes; examining non weakly-coupled modes through single antenna results would be irrelevant. We have plotted $\|\bar{J}_{m_2}\|,\ \|\bar{J}_{m_1}\|$ in a frequency range from 72 to 82 MHz; in comparison the eigenvalue traces $\lambda_{m_1},\ \lambda_{m_2}$ are also shown with values on the right axis (the exact FEKO numbering $m_1 = 1,\ m_2 = 5$ is avoided since it is arbitrary). For mode m_1, there seems to be a tracking issue at 79 MHz which appears in both curves with a high magnitude of current. On the contrary, mode m_2 at 78 MHz presents a spurious current change that is not due to tracking issues. As mentioned before, the total response of the single antenna "suppresses" this feature owing to a low α_{m_2}.

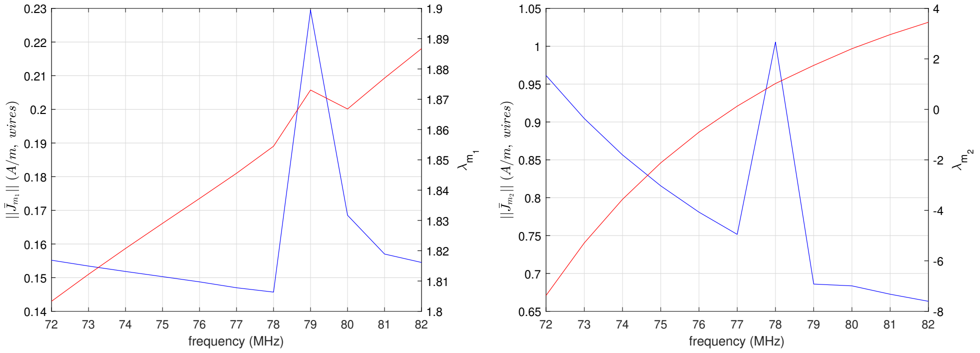

(a) **(b)**

Figure 5.7. (a): Vector norm $\|\bar{J}_{m_1}\|$, over all wires (in A/m), of modal current $m_1 = 1$ in the narrow frequency band 72-82 MHz. In comparison, with values on the right axis, the eigenvalue trace λ_{m_1} tracked in the same narrow band, (b) Same for mode $m_2 = 5$.

In order to further check the possibility of the strong coupling at this frequency, the comparison of simulated currents for one and two antennas can be performed, in a vector-norm sense. We have not checked though all possible cases of $m_1,\ m_2$ since, according to the coupled modes theory, c is given by [57, Eq. (17)] and the computational cost, along with normalization issues for calculating correctly all $P_{m_1 m_2}$ is still ongoing work. The straightforward approach is to try to minimize the relative error $\|\bar{J}_m - [c_1\bar{J}_{m_1}; c_2\bar{J}_{m_2}]\|/\|\bar{J}_m\|$ with all possible combinations of $m_1,\ m_2$, constrained by a unique normalization factor such that $\|\bar{J}_m\|^2 = c_1^2\|\bar{J}_{m_1}\|^2 + c_2^2\|\bar{J}_{m_2}\|^2$. This problem is solved using the Lagrange multiplier minimization technique and results in coefficients that achieve minimum when:

$$
\begin{aligned}
c_1 &= \sqrt{\frac{\|\bar{J}_m\|^2\|\bar{J}_{m_1}\|^2}{\|\bar{J}_{m_2}\|^2(\|\bar{J}_{m_1}\|^2 + (\gamma/\delta)^2\|\bar{J}_{m_2}\|^2)}} \\
c_2 &= \sqrt{\frac{\|\bar{J}_m\|^2\|\bar{J}_{m_2}\|^2}{\|\bar{J}_{m_1}\|^2(\|\bar{J}_{m_2}\|^2 + (\delta/\gamma)^2\|\bar{J}_{m_1}\|^2)}}
\end{aligned}
\tag{5.6}
$$

where $\gamma = \bar{J}_m^T(\Omega_1)\cdot\bar{J}_{m_1},\ \delta = \bar{J}_m^T(\Omega_2)\cdot\bar{J}_{m_2}$ and the argument $\Omega_{1(2)}$ means that we only take the vector components that belong to the Ant.1(2) geometry. The term $c_2/c_1 = (\gamma\|\bar{J}_{m_2}\|^2)/(\delta\|\bar{J}_{m_1}\|^2)$ is equivalent to the coupling coefficient c used previously [115].

This approach is taking into account the simulated current data but ignores the far-field transformation (by Eq. (2.9)). It turns out that mode $m = 3$, which is mostly responsible for the cross-polarized off-zenith radiation (see Fig. 5.6b), achieves the minimum error norm exactly for $m_1 = 1,\ m_2 = 5$ examined above with:

$$
c = \begin{cases} -0.88 & \text{at } f = 77 \text{ MHz} \\ -0.82 & \text{at } f = 78 \text{ MHz} \end{cases}
\tag{5.7}
$$

This minimum relative error though amounts to $\approx 70\%$ for both cases, which hints to more complex phenomena that would better describe the strong coupling. A possible explanation is offered in the next subsection; concluding that there is at least one mode per antenna that contributes to the cross-polarized field gives rise to the question of whether the dual-polarized nature of the SKALA4.1 antenna can add to this complexity.

Polarization partitioning of the first-order coupling

The potential implication of the single-antenna modes via the coupled-modes theory in describing mutual coupling has provided useful insights on the two-antenna system. We are going to expand the previous framework to show why the two antennas might present irregular polarization characteristics with respect to the single antenna.

If the strong coupling power formulation can initially be approximated by the first order coupling, with $m = 3,\ m_1 = 1,\ m_2 = 5$ as identified above, then the expression in Eq. (5.2) can be written as follows:

$$P_{rad;m}(1 + j\lambda_m) = \frac{1}{2}\left(\bar{V}_{m_1}^T \cdot \bar{J}_{m_1} + \bar{V}_{m_2}^T \cdot \bar{J}_{m_2} + 2c\bar{V}_{m_1 m_2}^T \cdot \bar{J}_{m_1}\right) \tag{5.8}$$

This equation is seen from the point of view of the active antenna. The excitation vector $\bar{V}_{m_1 m_2} = \bar{J}_{m_2}^T \mathbf{Z}_{21}$ can be thought of as the perturbation added to $\bar{V}_{m_1}$. The off-diagonal matrix $\mathbf{Z}_{21}$ though has a different structure with respect to the self matrices. Since a MoM impedance matrix is constructed by Eq. (2.8) taking into account pairs of basis functions, matrices $\mathbf{Z}_{11},\ \mathbf{Z}_{22}$ are also sparse when split into polarization components. That is because basis functions are symmetrically defined on the two dipole arms of a certain polarization, so their effect on the orthogonal polarization cancels out. On the other hand, matrix $\mathbf{Z}_{12}$ has polarization components which present no symmetry with respect to each other. This has already been observed in the equivalent current results in [67].

The schematic in Fig. 5.8 outlines this concept further by depicting the four entries of matrix $\mathbf{Z}_{12}$ when split into polarizations. When Ant.1X dipoles are active, both polarizations of the passive Ant.2 are affected in a non-symmetric way: the two arms of each polarization stand at dissimilar distances from each arm of Ant.1X. This means that the matrix $\mathbf{Z}_{1X2Y}$ will be comprised by elements of significant values, in contrast to the matrices $\mathbf{Z}_{1X1Y},\ \mathbf{Z}_{1Y2X}$ etc. which are all depicted as ϵ since they have resulted by symmetric operations[3]. In consequence, $\bar{V}_{m_1 m_2} = \bar{J}_{m_2}^T \mathbf{Z}_{21}$ will also lead to a non-trivial excitation term along Ant.1Y. What is more, the $\bar{V}_{m_1 m_2}(\Omega_{1X}),\ \bar{V}_{m_1 m_2}(\Omega_{1Y})$ parts of the vector might have different phasing, triggering a mutual coupling resonance that is pointing away from zenith. For completeness of the discussion, if polarization Ant.1Y was active, this would only happen for the Ant.2X (in a symmetric way as before with Ant.1X and Ant.2Y).

It is evident from this observation that the apparent discrepancies in our first-order coupling approach of Sec. 5.2.2 can be traced to polarization interactions. If a pair of dual polarized antennas has non-negligible cross-polarization, then the

---

[3] In reality, ϵ might not be of low values per se, but would result in such values when multiplied by a symmetric current vector with respect to two dipole arms, due to positive and negative contributions adding up to ≈ 0

orthogonal polarizations to those excited would present at least one significant mode that we would have to take into account to describe the interaction. In such a case, the first-order coupling of one dual-mode antenna to another, also treated in [115], could be harnessed, but we have not extended the scope of this section in such calculations.

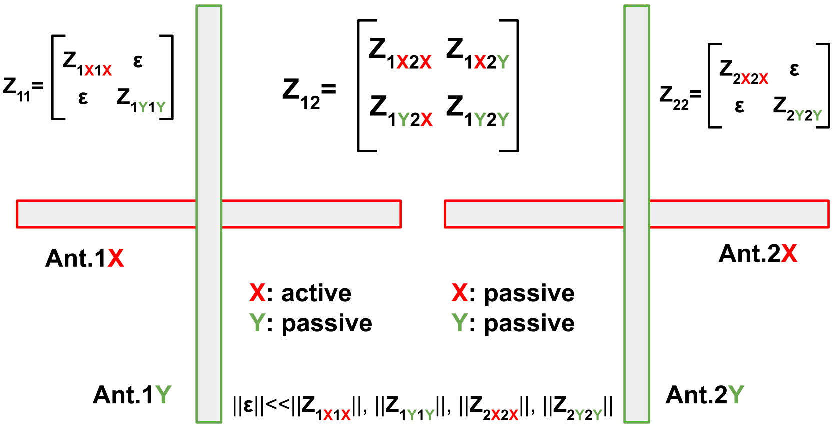

Figure 5.8. Schematic representation of the interactions between the various polarization components of Ant.1 and Ant.2, by inspection of its XY-split $\mathbf{Z}_{12}$ in conjuction with the geometric parts of X (red color) and Y (green color) of each antenna.

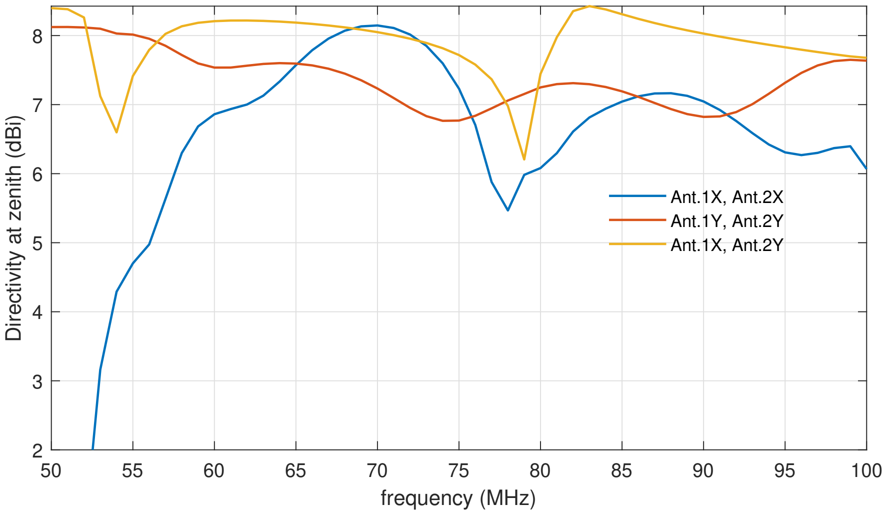

Figure 5.9. Directivity at zenith (in dBi) for a system of antennas truncated to one polarization component each. The combinations (X, X), (Y, Y) and (X, Y) are tested, where the first component refers to Ant.1 (active) and the second to Ant.2 (passive).

To quantify this in terms of far-field directivity of the two-antenna system, we have simulated various pairs of the X and Y polarization of SKALA4.1, whereby each antenna was reduced to one of them while all the geometric parts of the orthogonal polarization were removed. Fig. 5.9 shows the zenith-directivity curves (in dBi) for the 3 combinations of Ant. 1 and Ant. 2: (X, X), (Y, Y) and (X, Y), respectively. We observe that the previous break-down in terms of matrices is confirmed, in the sense that only the curve pertaining to Ant.1Y, Ant.2Y is free of spurious features, with a variation that is smoother. Both the combinations Ant.1X, Ant.2X and Ant.1X, Ant.1Y present a mutual coupling resonance at 78, 79 MHz respectively, of about the same magnitude (2.5 dB). At 54 MHz, the Ant.1X, Ant.2Y pair also presents the mutual coupling feature observed in previous plots.

5.3 Coupling mitigation strategies

In this section, attempted solutions to the problem of mutual coupling induced anomalies will be addressed, utilizing the observations of the previous sections. In particular, dipole loading with reactive elements will help in understanding whether the problem can be solved artificially by changing the radiation properties at the affected frequency narrow bands without geometrical modifications, while such modifications will then be applied for a more robust mitigation.

5.3.1 Dipole loading

As has generally been shown for log-periodic dipole antennas in [73], and for SKALA4.1 in previously in Sec. 2.3.2, both using the Characteristic Modes Analysis, such antennas have certain log-periodically spaced resonant features. For the SKALA4.1 antenna, three resonant features reside in the frequency range 50-100 MHz. Their mode tracking also hints to certain geometric characteristics independent of the excitation. It is known though [73] that a symmetric boom in any log-periodic antenna has little effect on its radiation properties, so these modes are due to single or coupled dipoles resonant radiation. To put these radiation peaks into perspective, we first examine the radiated power at zenith P_{rad} in the full operating frequency range of the antenna. A simulation using the FEKO software, and assuming a constant voltage excitation of $V_s = 1$ V, results in the 50-350 MHz for a SKALA4.1 antenna shown in Fig. 5.10. The first peak (59 MHz) is at least four times larger than the third (95 MHz), the second peak (75 MHz) at least two times the third, while all the others are diminished.

Another way to see this is that the reflection coefficient referenced at $Z_0 = 50\ \Omega$ has a high magnitude at lower frequencies. Graphically, we present these resonances on the Smith chart at the upper right of Fig. 5.10. The outermost starting point corresponds to 50 MHz, while the innermost ending point to 350 MHz. The 3 left crossings (< 1) of the horizontal axis indicate these 3 resonances and show that the input impedance is $Z_{in} = \Re\{Z_{in}\} < Z_0$, equivalent to the reflection coefficient being $S = \Re\{S\} < 0$ at the respective frequencies. From the definition of radiated power and using $Z_{in} = Z_0(1+S)/(1-S)$ after calculations we get:

$$P_{rad} = 1/2 V_s^2 \Re\{Z_{in}^{-1}\} = \frac{V_s^2}{2Z_0} \frac{1-|S|^2}{|1+S|^2} \tag{5.9}$$

Looking into the monotony of this function though, we have the following cases:

- when S is real and negative then $S = -|S|$ so: $P_{rad} = \frac{V_s^2}{2Z_0}\frac{(1-|S|)(1+|S|)}{(1-|S|)^2} = \frac{V_s^2}{2Z_0}\frac{1+|S|}{1-|S|}$. This function is ascending so when $|S|$ is maximum (or S minimum in the negative axis), P_{rad} is also maximum (*resonance*-red circles in Fig. 5.10).

- when S is real and positive then $S = |S|$ and $P_{rad} = \frac{V_s^2}{2Z_0}\frac{1-|S|}{1+|S|}$. This function is descending so the conclusion is the opposite (maximum $|S|$ means P_{rad} minimum or *anti-resonance*-purple circles in Fig. 5.10).

All higher frequency resonances can only be inferred as minima of $|S|$, since the reactive component seen by each excited dipole, geometrically below itself, is not cancelled (we do not have an exact self-resonance). The fact that at the first 3 resonances we have exactly $\Im\{Z_{in}\} = 0$ (or $\Im\{S\} = 0$) also explains their sharpness.

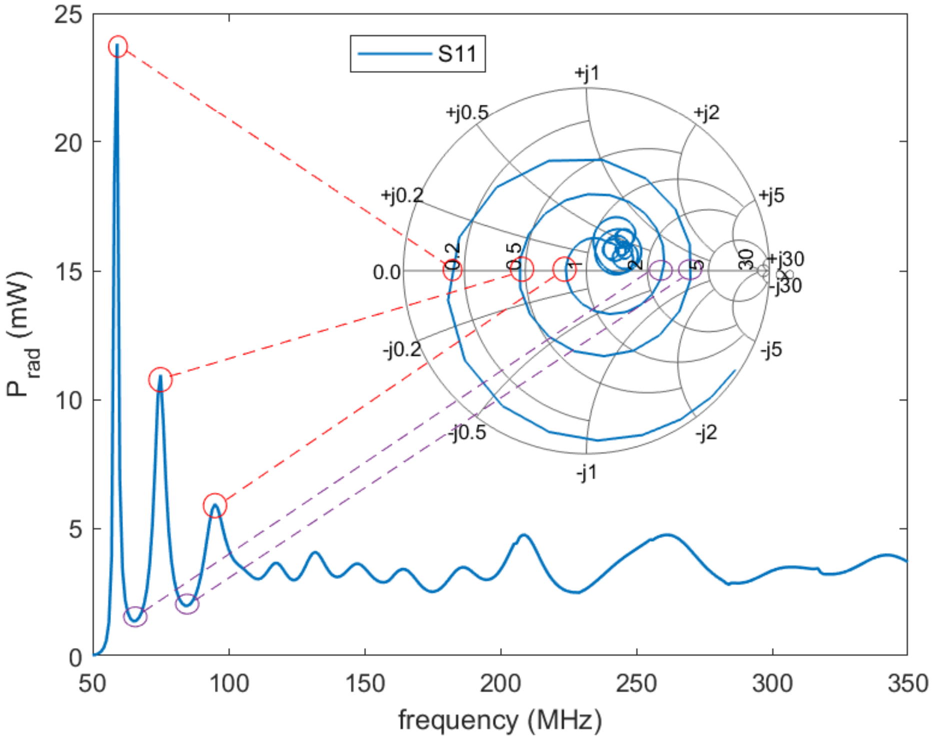

Figure 5.10. Zenith P_{rad} (mW) of a X-polarization excited SKALA4.1, over 50-350 MHz. Indented is a Smith chart of the transformation $S = (Z_{in} - Z_0)/(Z_{in} + Z_0)$, showing the SKALA4.1 reflection coefficient over the same frequency range (outer to inner points for increasing frequency). Red (purple) circles highlight the *(anti-)resonances*.

Both the radiation peaks and troughs therefore stem in a defined way from the S-parameters. The loading can better be understood by means of the S-parameters because, as practiced in [116], a perturbational matrix inversion can yield the new current vector MoM solution $\bar{I}_L$ as a function of the load value and the nominal solution $\bar{I}$, and then trivially $Z_{in;L} = Z_{in}I_m/I_{m;L}$ where $I_{m(L)}$ is the current at the port instance m of the mesh for the two cases (unloaded and loaded). If a reaction compononent X_L is used at port instance n, it can be further proven (via the Sherman-Woodward-Morrison formula) that:

$$\bar{I}_L = \left(\mathbf{I} - \frac{X_L}{1 + X_L[\mathbf{Z}^{-1}]_{nn}}\mathrm{col}_n^T\left(\mathbf{Z}^{-1}\right)\right)\bar{I} \tag{5.10}$$

Given only the mesh instance currents, we conclude that X_L, stemming from a complex relation involving the MoM admittance matrix column n, $\mathrm{col}_n\left(\mathbf{Z}^{-1}\right)$, cannot be directly solved in terms of their ratio $I_{m;L}/I_m$. Some heuristic approach towards its determination must therefore be employed.

The goal of the dipole loading strategy is to turn a resonance into an anti-resonance (or close to one), to then test how two such loaded antennas would perform in a *baseline* configuration. We must also note that, from a computational point of view, such a perturbation does not affect the MoM matrix $\mathbf{Z}_{12}$ of the two-antenna configuration. In formulations such that of Eq. (5.8), the terms related to the single antenna response perturb the right hand side more than those related to mutual coupling, which means the antenna loading has to affect the appearence of mutual coupling in a non-negligible way when we keep all other parameters of our *baseline* two-antenna configuration constant.

We have subsequently experimented with reactively loading the low-frequency resonant dipoles, to examine both the antenna matching and the electric field peak behaviour. We focus our analysis here on the electric field peak at 75 MHz. An examination of the antenna current distribution at this frequency reveals that the 3 longest dipoles (including the bow-tie) are in resonance or close to resonance. To achieve resonant features with $\Re\{S\} < 0$ and simultaneously non-zero $\Im\{S\}$, a reactive component on some of these dipoles can be placed on the wire position were the current has a high value. We choose this position to be at $l_d/4$ from the boom, where l_d is the semi-dipole length, since we would like to avoid directly loading the boom.

The choice of inductor or capacitor values is made by finding a desired reactance X_L at this frequency, both as sign and magnitude. After experimentation, we have chosen capacitors of $C_L = 6\ pF$, that result in $X_L = -353.6\ \Omega$ at 75 MHz. Such a large value is needed because of the lumped element implementation of C on only one mesh element, which is seen in that one column in the loaded inverted MoM Z-matrix accounts for the perturbation in Eq. (5.10)[4]. In Fig. 5.11a we present the electric field at zenith in the range of 50-100 MHz, for the case of loading the bow-tie and the next longest dipole with C_L. The real and imaginary parts of the reflection coefficient are seen in Fig. 5.11b.

We conclude that the first peak has been shifted to lower than 50 MHz with respect to the unloaded antenna, while the other 2 peaks shifted to lower frequencies by about 8-12 MHz, with their overall amplitude comparable to each other. It is also remarkable that the reflection coefficient seems to be almost the opposite sign that of the unloaded antenna. The electric field peaks still correspond to a negative real S, but at 75 MHz we now have a slightly positive $\Re\{S\}$ and non-zero $\Im\{S\}$. The directivity is shown with the dashed curve on Fig. 5.11a, and is mostly unaffected.

---

[4] If i is the loaded mesh element, then $Z_{ii;L} = Z_{ii} + Xl_i^2$, where l_i is the mesh element length. Using meshing data from FEKO, at 75 MHz we have $Xl_i^2/\mathrm{mean}(\Im\{Z(\mathrm{wires})\}) \approx -0.5$.

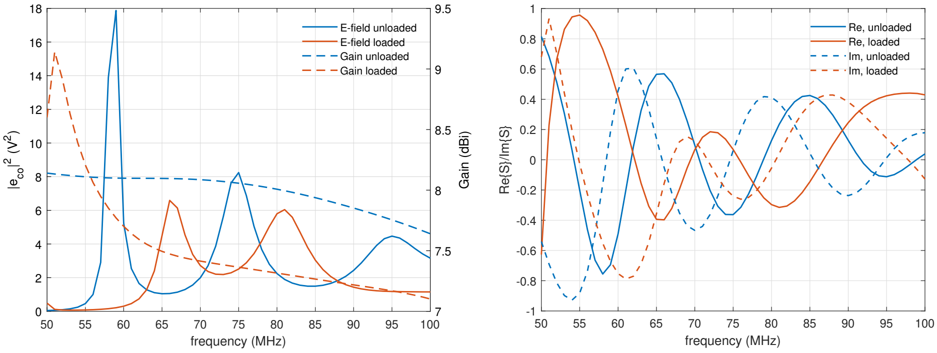

(a) **(b)**

Figure 5.11. (a): $|e_{co}|^2$ in (V^2) and gain in dBi, at zenith, over 50-100 MHz for unloaded and capacitevely loaded cases of SKALA4.1 (with $C_L = 6$ pF on dipoles 19, 20 and at $x = l_d/4$), (b): real and imaginary parts of S for both the above cases.

For two identical antennas, there is a susceptibility of the resonant region in any scattering from the passive antenna on the active. As it has been shown in [117] when S_{11} (the reflection coefficient of the active antenna) is real, there exists a maximum coupling mechanism. In our case, two SKALA4.1's present a spurious mutual coupling mode close to the radiation mode of the single antenna at 75 MHz. If we use the loaded antenna in our *baseline* two-antenna configuration of Sec. 5.1.2, in a pair of an active and a passive one, the electric field and gain results are shown in Fig. 5.12. The response is seen to have a more moderate null at 77-78 MHz for the loaded antennas, but a new null is apparent at 84 MHz, possibly due to a degeneracy of the loaded dipoles. The $|e_{co}|^2$ at zenith is seen to preserve the radiation peaks of the single loaded antenna, but is nonetheless affected by the mutual coupling perturbation, which appears to be inherent to the antenna characteristics as it is fixed at 77-78 MHz.

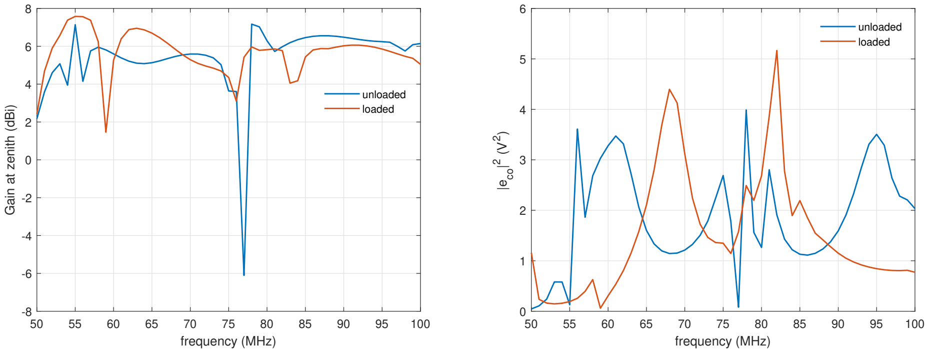

(a) **(b)**

Figure 5.12. (a): Gain at zenith in dBi for the *baseline* two-antenna system, when both antennas are unloaded and loaded with $C_L = 6$ pF on their dipoles 19, 20 (at $x = l_d/4$), (b) $|e_{co}|^2$ at zenith in V^2 for the same cases.

Part of this work has appeared in [118]; we were then led to consider geometric modifications of the antenna in order to tackle mutual coupling.

5.3.2 Geometric modifications

In this section, the analysis of a slightly modified version of the SKALA4.1 antenna is presented, such that the mutual coupling resulting by testing the two-antenna configuration is mitigated. It is important to note that in our pursuit of such modifications, we have to always make sure that the antenna performance be perturbed at the minimum possible way. That is because a log-periodic design might suffer from new unwanted phenomena if the progression of its resonances is interfered with, and the antenna has to cover a large fractional bandwidth.

The essential idea of the proposed modification is to distance the polarizations of the bow-tie dipoles, such that interaction of two adjacent antennas results in a better $|e_{cr}|^2$ (or IXR) at the frequencies of strong mutual coupling. As we have seen in Sec. 5.2.2, the two-antenna system scattering profits from the fact that the antennas' polarizations are aligned, by allowing significant interaction of the cross-polarized components of different antennas. In changing the shape of two orthogonal dipoles, the cross-polarized radiation according to the 3rd Ludwig definition [66] is biased according to the coordinate system chosen, which might not fully align with the new dipoles (for non-straight shapes). For that reason, we will rely on the IXR in order to assess the cross-polarization performance of the new antenna.

The new bow-tie dipole has the same principal length along each polarization, but its arms are stretched in the orthogonal direction by means of an added rectangular tube. The shape remains symmetric with respect to a 180° rotation. A screen capture from CADFEKO is shown in Fig. 5.13, where the new antenna shape has been parametrized by two new geometric lengths:

- the extension length l_e, across the $x,\ y$ direction for the $Y,\ X$ polarized dipoles, respectively. This is the critical parameter that can rearrange the polarization interactions by means of distancing the dipoles of adjacent antennas

- the taper width w_t, across the z direction, which describes the filling along the dipole shape of two horizontal cuts on the boom. This parameter can affect the matching of the antenna at lower frequencies, given that it connects the new bow-tie arms to the boom

A possible advantage of such a modification also appears to be of mechanical nature; using the same antenna pieces and only adding new rectangular tubes to connect them to a boom in a different way might be a readily applied solution, if standard tubes are used. If we consider such segments as electrically short at frequencies $f_u < 100$ MHz, setting an upper limit $l_e \lesssim \lambda_u/8 = 0.375$ m, then we can safely assume that this tube does not radiate on its own, but rather works as a transmission line for the radiation (seen as its termination) of the bow-tie dipole arms. This is a complicated analysis, and its validity is still an ongoing work.

Since this antenna design was identified as a good candidate for reducing the mutual coupling, initially with arbitrary parameters $l_e,\ w_t$, refining of those was directly probed with the *baseline* two-antenna configuration. Avoiding the alignment

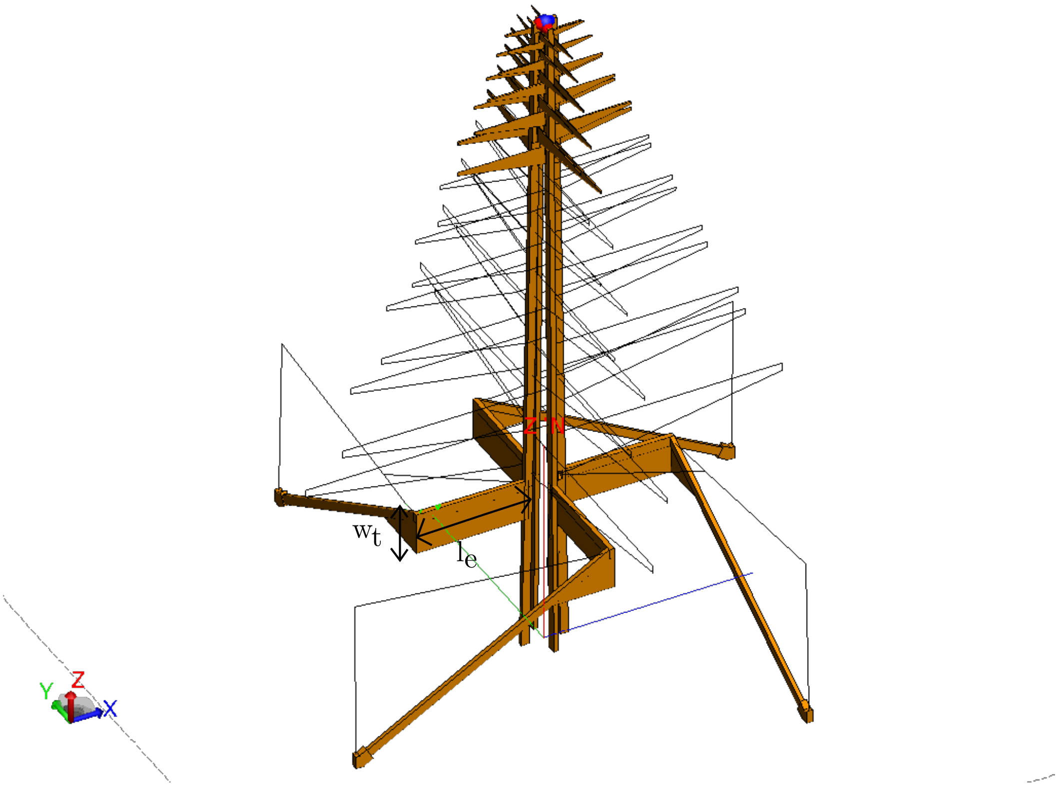

Figure 5.13. CADFEKO screen capture of a SKALA4.1 where its bow-tie dipoles have been modified to stretch across the direction orthogonal to their polarization.

of dipole arms on the coordinate system x axis raises the question of whether an offset $\phi_0 > 0^\circ$ might achieve a similar alignment between dipole arms. This actually happens when $\phi_0 = \arctan\left(\frac{2l_e}{D_0}\right)$, which is another configuration that we test in parallel, which we call *offset*; in this case, too, $D_0 = 1.5$ m. Fig. 5.14 presents the directivity at zenith for the *baseline* configuration when l_e is varied from 25 cm to 50 cm, while Fig. 5.15 presents the directivity at zenith for the same cases of l_e for the *offset* configuration.

We first comment on the shift of the mutual coupling glitch frequency, seen here centered at 72-73 MHz for the *baseline* configuration and around 68-69 MHz for the *offset* configuration. This effect is brought about by the change in the bow-tie geometry. It is also apparent that the distortion is now a drop of simpler profile (possibly fit by some analytical approximation) for the *baseline* configurations, rather than a more wideband and oscillating glitch. This more complex shape is the case for the *offset* configuration, where alignment of dipole arms induces more severe current imbalance. Interestingly, the exact position of the directivity minimum is dependent on the length l_e for the *offset* configuration.

The moderation of the amplitude loss is the most significant result of this antenna: a worst-case drop of ≈ 3.5 dB is singled out across the various curves. This is consistently observed for all possible lengths and the two configurations, indicating that sufficient distancing of the polarizations as well as the previously aligned co-polar dipole arms of the bow-tie has compensated for the previously

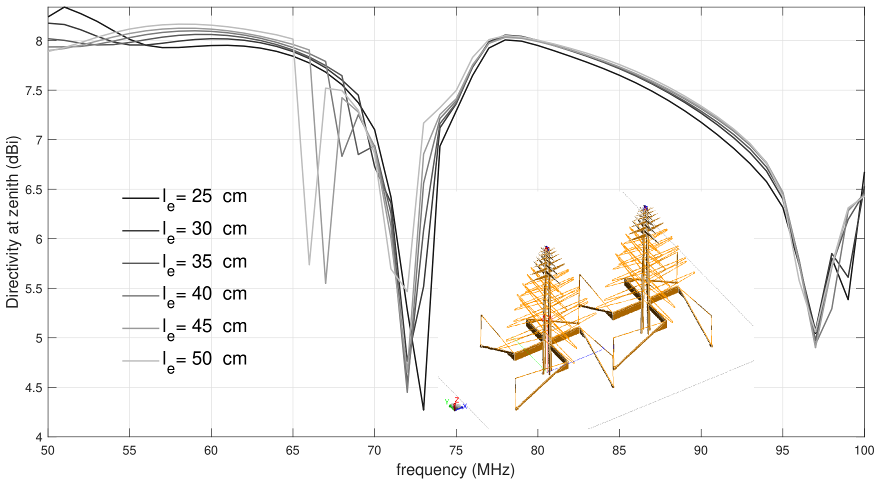

Figure 5.14. Directivity at zenith (dBi) in the frequency range 50-100 MHz, of two SKALA4.1 antennas with the modified bow-tie dipole design and varying l_e from 25 cm to 50 cm. The configuration is *baseline*, shown in an indented image.

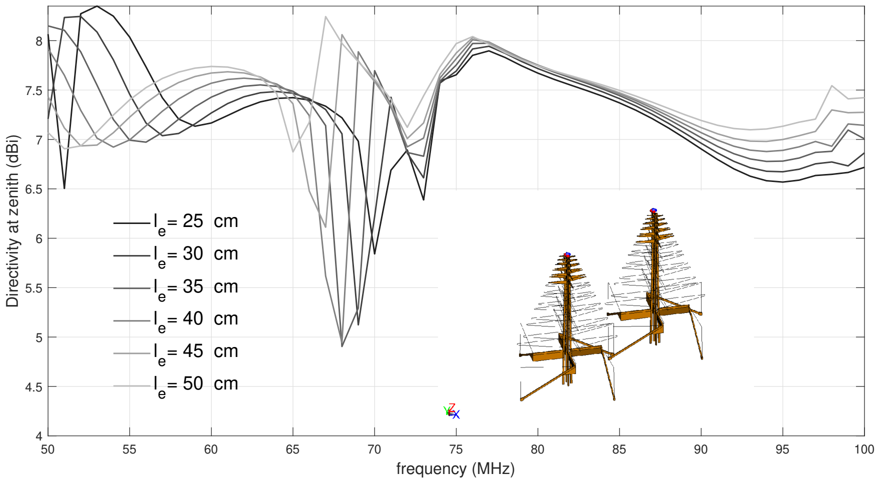

Figure 5.15. Directivity at zenith (dBi) in the frequency range 50-100 MHz, of two SKALA4.1 antennas with the modified bow-tie dipole design and varying l_e from 25 cm to 50 cm. The configuration is *offset*, shown in an indented image.

greater intensity of the phenomenon. Apart from the mutual coupling in the center of this band, we can also observe the following facts:

- the lower frequency glitch at 55 MHz is now out of band. All of the curves verify this finding, with the exception of that of $l_e = 25$ cm
- the higher frequency glitch, previously seen at around 95 MHz in Fig. 5.3a, is more pronounced in the *baseline* configuration; a drop of 1.5-2 dB is observed in all of the curves

The parametric analysis of the two figures leads us to choose the length l_e of a new, nominal design. It can be seen in Fig. 5.14 that adjacent frequencies, lower than 70 MHz, are affected by a new glitch when excessively increasing l_e (>30 cm), due to radiation of the new rectangular tubes. The best value for which we see a mostly clear profile of the gain drop seems to be at exactly $l_e = 30$ cm. Various array configurations, only instances of which will coincide with our two 'worst-case' configurations, might now be able to further render mutual coupling mostly or completely obsolete in the formed beam and thus aperture efficiency of a SKA-Low station.

We are next going to compare the performance of this antenna to that of the original SKALA4.1 design. In Fig. 5.16, the parameters are fixed at the values $l_e = 30$ cm, $w_t = 10$ cm. The gain response at zenith is shown, as well as that of $|e_{co}|^2$ for the Y-polarized dipoles. The co-polarized field $|e_{co}|^2$ is shown up to 125 MHz, where the resonances of the antenna are seen to be affected by the modification. It is clear that the bow-tie resonance has shifted lower at 54 MHz, while the resonance at 75 MHz has increased in intensity; this explains the extra spectral ripple present in the gain response, since no other spurious electric field features appear. In having kept that resonance constant in frequency while changing the geometry of the antenna, we are now effectively testing the alternate scenario of the mutual coupling formalism of Eq. (5.8): that of mostly unperturbed single antenna terms (except for maybe a scale factor), while the mutual coupling terms are now altered due to a new $\mathbf{Z}_{12}$.

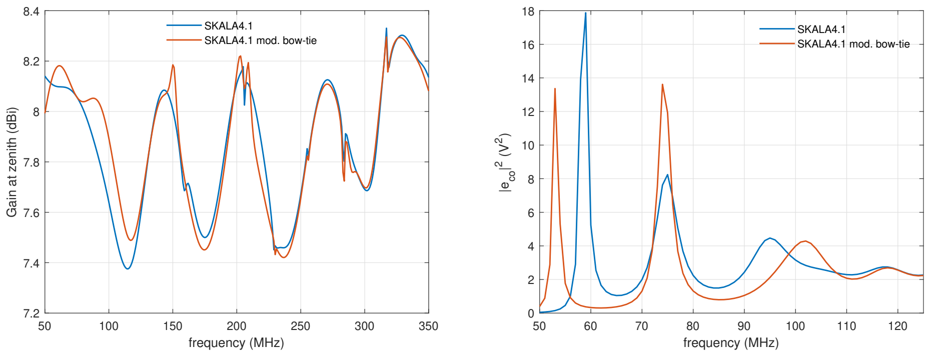

(a) **(b)**

Figure 5.16. (a): Directivity at zenith in dBi for the SKALA4.1 with its bow-tie modified in a new geometry as in Fig. 5.13, compared to that of the original SKALA4.1 antenna (b) $|e_{co}|^2$ (V^2) for the same antenna cases.

The reflection coefficient is presented in Fig. 5.17b and is also different at the lower frequencies, while better matched at the lowest extreme of 50 MHz. The antenna resonance at 75 MHz is now matched at a lower level to 50 Ω, as seen by the peak of Fig. 5.16b combined with Eq. (5.9). The resonance at 95 MHz has shifted to 102 MHz, while all others are closely following the original SKALA4.1.

Fig. 5.17a presents the minimum, maximum, and average IXR for the original and modified antenna design, within a field of view defined by $0 \leq \theta \leq 45°$ and

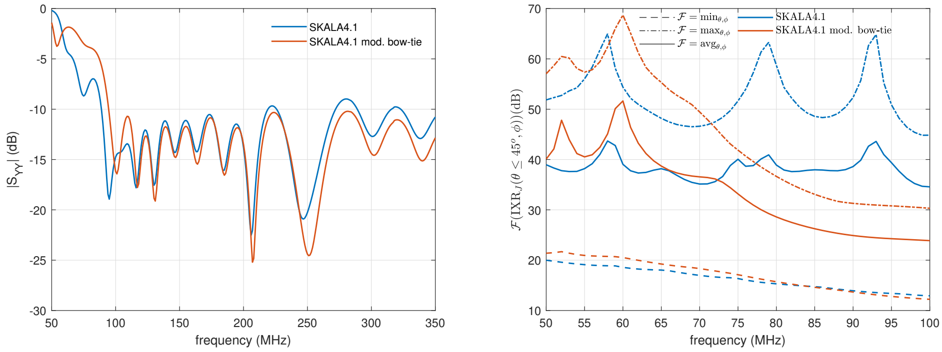

(a) **(b)**

Figure 5.17. (a): $|S_{YY}|^2$ in dB for the same cases, (b) Minimum, maximum and average of the IXR frequency response in dB, over the spherical field of view $\Omega = \{0° \leq \theta \leq 45°,\ 0° \leq \phi \leq 360°\}$, for the same antenna cases.

for frequencies lower than 100 MHz. There are some differences now between the two antenna versions: while the minimum IXR is largely similar, the average and maximum IXR present a smoother response less concurrent with the antenna resonances. Apparently, the differences in dipole modes among the two polarizations, which are geometrically slightly displaced (higher port along z for the X-polarized dipoles), are in this new antenna more significant. We conclude though that the IXR is still within the acceptable limits for polarimetry.

Lastly, for the antenna using $l_e = 30$ cm and $w_t = 10$ cm, we return to the two antenna *baseline* configuration to examine the full-sphere patterns at distinct frequencies, as well as the IXR. Fig. 5.18 presents the directivity in dBi for 8 consecutive frequencies, while Fig. 5.19 presents the IXR in dB for the same frequencies. These are uv maps of the respective patterns, where $u = \sin(\theta)\cos(\phi),\ v = \sin(\theta)\sin(\phi)$ the orthographic projections from spherical coordinates. A common color scale is used for all subplots, while black circles indicate the $\theta = 45°$ boundary.

We now see that apart from the zenith, the "inclination" of the beam lobe results in lower directivity values in more areas of the field of view. At 72 and 73 MHz, the whole area $90° \leq \phi \leq 270°$ has lower directivity values, while in subsequent frequencies up to 77 MHz a null seems to enter the field of view at $\phi \approx 32°$. The beam remains though directive, in the sense that all dBi values apart from this null are positive. As far as the IXR is concerned, the maps now show some degradation of the polarization purity with the introduction of the second antenna at close proximity, as has also been the case with the original SKALA4.1 antenna; significant angular extents close to zenith though remain of high IXR. The rest of the structure of this polarization performance leads to interesting conclusions: the most affected frequency (73 MHz) has the most extensive spherical area of low values but retains high IXR in a small patch around $\theta \approx 35°$, whereas in the case of the nominal SKALA4.1, the antenna pair had its worst Ludwig-III cross-polarization (see Sec. 5.2.1). The asymmetry though propagates as low IXR to the higher frequencies with a ring-like structure ($-90° \leq \phi \leq 90°$, where the gain is higher) presenting significantly entangled polarization components. More direct comparisons would need to be made in order to assess whether this level of IXR is an improvement, for this type of *baseline* configuration, to the same one employing the original SKALA4.1 antenna.

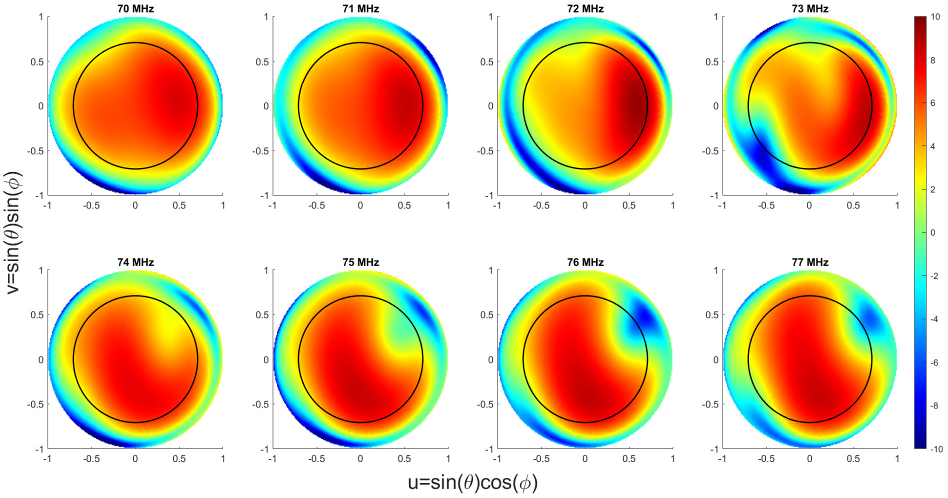

Figure 5.18. Directivity (dBi) across 70-77 MHz, as a uv map of the full upper hemisphere, of two SKALA4.1 antennas with the modified bow-tie dipole design featuring $l_e = 30$ cm, $w_t = 10$ cm. Black circles indicate the $\theta = 45°$ boundary. The configuration is *baseline*.

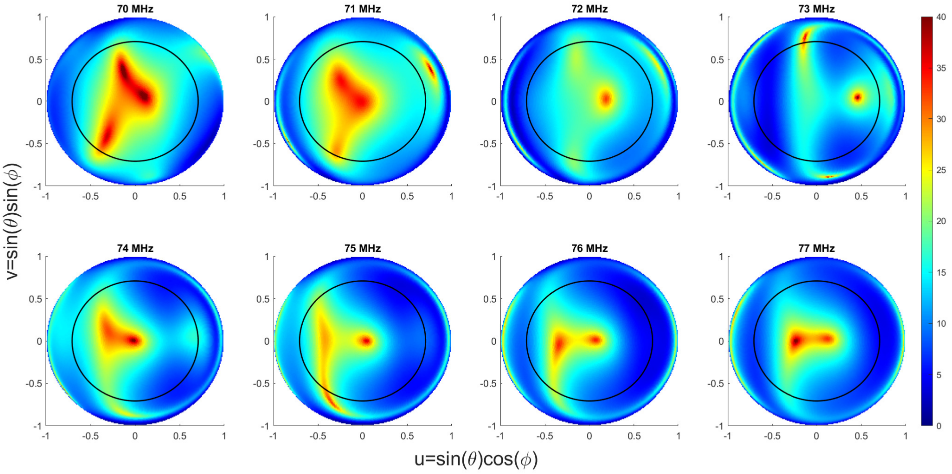

Figure 5.19. IXR (dB) across 70-77 MHz, as a uv map of the full upper hemisphere, of two SKALA4.1 antennas with the modified bow-tie dipole design featuring $l_e = 30$ cm, $w_t = 10$ cm. Black circles indicate the $\theta = 45°$ boundary. The configuration is *baseline*.

Chapter 6

Conclusions and future perspectives on SKA-Low electromagnetic modelling

As it has been seen in the preceding chapters, electromagnetic analysis for low-frequency arrays is a key tool in understanding both the performance of the isolated element to be used in an array environment, as well as features emerging from the array structure and its platform. Mutual coupling and ground plane diffraction, respectively, are the main issues examined here.

In Ch. 2, an outline of the numerical methods used throughout the thesis is presented with an emphasis on their challenges for analysis of large arrays. The Method of Moments and Characteristic Modes Analysis are both used in the computation of the SKALA4.1 antenna properties such as Far-Field gain, S-parameters, Internal Cross-Polarization Ratio as well as the Electric-Field intensity (co-polarized and cross-polarized). Comparison with two commercial solvers reveals a good level of agreement for these parameters, while the CMA decomposition points to the dipole-mode properties of the antenna radiation, that will later be of interest in the mutual coupling of two antennas. Finally, a simplified model of SKALA4.1 by substituting the boom with passive transmission line segments is shown to well reproduce some of the resonant behaviour of the antenna by fine-tuning the characteristic impedance of such segments; use of this model is principally made to test antenna lumped loading scenarios.

In Ch. 3, we have presented a new way of tackling the problem of spurious radiation by a log-periodic dipole antenna owing to secondary modes of the constituent dipoles. The addition of a properly placed RLC parallel load at the maximum current position of these modes, has led to the dissipation of their energy on the resistor R, with a subsequent reduction of the total Q-factor at the resonant frequencies. For a full log-periodic antenna, the cost on radiation efficiency is negligible, since their modal amplitude is already quite low. Application on a SKALA4.1 antenna led to the dipole glitches being eradicated in the sense of achieving gain smoothness. Experimental verification of the method by means of anechoic chamber measurements of the S-parameters of a two-antenna system with a VHF antenna and a SKALA4.1 as its 2 ports also strengthened this result. Our prototypes could in the future be optimized for industrial production of such dipole elements by implementing the RLC loads integrated on the PCB screwable connecting piece.

A 256-antenna SKA-Low station presents certain spectral characteristics in the 50-100 MHz band owing to the 42 m circular ground plane placed under the antennas. In Ch. 4, we identified and characterized this effect for isolated as well as embedded antennas into a station of the AAVS2.0 layout, as being related to the principal Hankel transform wavenumber of the radiating circular plane or certain multiples of it. Both solvers used, FEKO and Galileo, are shown to agree and a numerical approximation method by Galileo speeds up the simulation time for the array. We also report the intertwining of this effect with the mutual coupling spectral glitches already known to appear in certain frequencies using a DFT transform to identify the fundamental length for isolated and embedded antenna gain pattern ratios, and the ECC to quantify the level of the combined effect. For the EEPs, the DFT components peak at different values of the sampled space of lengths, which are generally lower the closer an antenna approaches the edge of the ground plane, while their ECC penalty when calculated with respect to the infinite ground plane EEPs is always less than 4% in the examined frequency range. For the station beam patterns, the normalized difference between infinite and finite ground plane solution is limited to 1% for uniform beamforming. The appearence of this diffraction phenomenon in measured sky spectra is an expected future activity, using SKA-Low prototype stations, in order to further verify its impact on real astronomical data.

In Ch. 5, antenna mutual coupling in pairs of antennas is tested with a baseline, maximum coupling configuration. After presentation of some recent experimental measurement of the phenomenon, we use the Characteristic Modes analysis: the size of the our problem is challenging with respect to the interpretation of its results, as tracking issues prevent us from fully understanding the behaviour of each mode across the examined frequency range, but narrow-band mutual coupling glitches are sufficiently localized at certain modal components. The theory of coupled characteristic modes is used to connect the mutual coupling radiation modes identified in the two-antenna system with a dominant mode of the active, single antenna, while the strong coupling scenario is also probed. In order to ameliorate the mutual coupling phenomena, an antenna loading strategy shifts the electric field resonances away from the affected frequencies; although effective in reducing the loss of sensitivity, the change in dipole reactance triggers new anomalies. More effective is the modification of the bow-tie dipoles to further disentangle the two orthogonal components, an ongoing work which shall be verified in (sub-)station simulations in the future.

Other directions of future work in electromagnetic modelling of the SKA-Low antennas include the inter-stational coupling between antennas of adjacent stations in the core of SKA-Low. When some of the core SKA-Low stations need to be characterized in terms of their EEPs, array simulations taking into accounts antennas, and possibly the ground planes of more than one SKA-Low station are deemed necessary to quantify unwanted effects due to mutual coupling. Such approaches, due to the size of the problem, require either some geometrically driven reduction of the model, and/or advanced acceleration methods to yield results in reasonable simulation times.

Addendum: The importance of antenna platform and mutual coupling effects on global 21cm signal cosmology experiments

Cosmic Dawn, the onset of star formation in the early universe, can theoretically be detected via the 21cm transition of neutral hydrogen, for which an absorption signal, shifted down to the MHz frequencies, can be extracted from all-sky observations averaged in radiometer data. This signal, in antenna temperature scales, is predicted to be in the order of $10^1 - 10^2$ mK. Any detection attempt therefore requires separation of the 21cm signal from extremely bright and spectrally diverse foreground emission due to our Galactic structure (reaching orders of $10^5 - 10^6$ K, as well as characterisation of how this signal couples to the instrumental response, which can also be spectrally "chromatic".

The critical challenge of subtraction of the bright foregrounds from radiometric data is normally attempted by modelling the spectrally smooth emission with an N-term log-polynomial and performing Bayesian inference for both foreground and background signals (e.g., [119], [120], [121]; [122]). The so-called "chromaticity", quantified by different figures of merit is a key factor in antenna design (e.g., [123]; [124]; [125]) and these beam effects can limit the effectiveness of foreground subtraction (e.g. [126]). Accurate antenna beam pattern simulations, including realistic ground plane and soil descriptions, are thus fundamental to process radiometric data. Moreover, these models have to be tested in Bayesian-inference signal extraction pipelines, since the eventual criterion of success is the bayesian evidence, which can suffer from multiple factors relating to both the sky and the beam models.

Mahesh et al. [127] explored antenna beam modelling as a source of uncertainty in global signal measurement, checking the stability of the signal reported by EDGES [121] with respect to choice of numerical electromagnetic solver code. Bradley et al. [128] instead investigated how a possible systematic artefact within the antenna ground plane may produce broad absorption features in the spectra. Raghunathan et al. [90] have described a conical monopole antenna with a high degree of spectral clearness, which they use in their SARAS3 experiment placed on the surface of a lake, in order to reduce the soil induced uncertainties. Recently collected and analysed data have discredited the EDGES detection [129]; the detection of this signal is, therefore, a hotly debated topic.

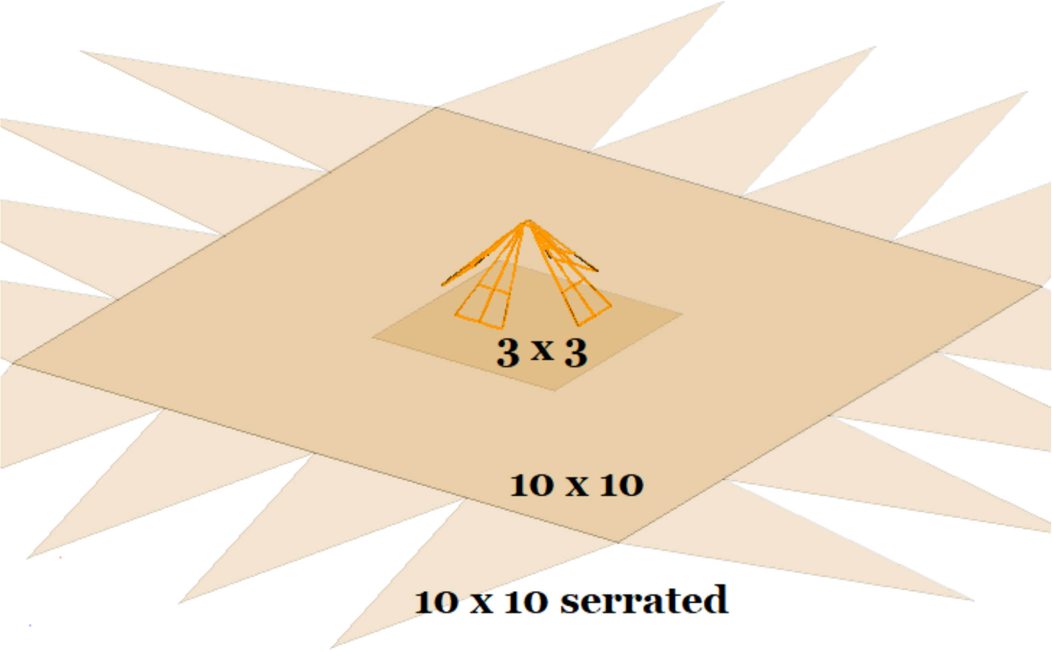

Figure 6.1. LEDA antenna 3D view of geometry with the ground planes to be used in the analysis. Dimensions are shown in meters.

I The case of LEDA

In this section we present an electromagnetic analysis and chromaticity calculations for the antenna used in the Large-aperture Experiment to Detect the dark Ages (LEDA). The experiment consists of an ensemble of two to five dual polarisation dipole antennas within the Owens Valley Radio Observatory Long Wavelength Array station (OVRO-LWA) and is deployed for precise radiometry, using custom RF and digital signal processing to match the timing, calibration, and stability requirements. It aims at the detection of the 21cm global cosmological signal by using all-sky drift scan data and has started collecting data in 2018.

Driven by science requirements, the frequency range of interest is between 50 and 87 MHz (although some of the simulation results are shown in a larger frequency range). We first present the antenna geometry, as-built, and the ground planes we have considered, as well as an older beam approximation model. In Sec. I.I, we review the analytic beam model used in previous analyses of LEDA data, while the focus of Sec. I.II is incorporation of the soil permittivty data and alternate ground-plane geometries.

I.I Antenna and ground plane description

We outline here the basic geometrical properties of the antennas used by LEDA for radiometry, which excluding the ground plane are similar to those used in general for construction of Long Wavelength Array stations ([130] and references therein) and OVRO-LWA specifically.

Table 6.1. Soil parameters for the one-layer and the multi-layer model, extracted from measurements of soil at the LWA site during both dry and wet conditions at depths $z_i,\ i = 1, 2, 3$.

Soil layer parameters (σ in S/m, ϵ_r dimensionless)				
	σ_{dry}	σ_{wet}	$\epsilon_{r,\text{dry}}$	$\epsilon_{r,\text{wet}}$
one layer	0.004	0.01	4.4	6.5
$z_1 = 10.16$ cm	0.0013	0.005	3.73	8.09
$z_2 = 35.56$ cm	0.004	0.0068	4.25	6.45
$z_3 = 53.34$ cm	0.0187	0.0388	7.58	20.56

Each antenna comprises two pairs of triangular dipole arms 1.50 m long, angled downward by 45° (Fig. 6.1). We focus our analysis on the east-west orientation. The default OVRO-LWA antenna ground plane [131], [132] is a 3 m × 3 m galvanized welded steel mesh with 2.51 mm wire diameter (12.5 gauge) and 10.2 cm spacing. In this analysis, we modelled the beam for one antenna, numbered 252 [133], with three ground plane configurations that corresponded to a series of test modifications made in the field [134]. The 3 m × 3 m ground plane was replaced first by a 10 m × 10 m patch of mesh comprising the same material but with a 3.06 mm wire diameter (11 gauge), and later by the same but with serrations as represented by four 5 m long, 1.25 m wide isosceles triangles positioned on each side (referred to as the serrated ground plane). The arrangement is shown schematically in Fig. 6.1. As in [121], peripheral serrations are sometimes added to ground planes to reduce coherence among currents proximate to the edge discontinuity.

We summarise now the analytical beam model of the LWA dipole used in previous works. For a more extensive description see [135], [130], [136]. Previous LEDA studies [119], [137] used this beam modelling. This model allows the reconstruction of the antenna beam pattern in every azimuth direction, using two principle antenna planes (E and H, effectively taking into account the antenna symmetries) and is described by:

$$A(\theta, \phi, f) = \sqrt{[p_E(\theta, f)\cos\phi]^2 + [p_H(\theta, f)\sin\phi]^2}.$$

The pattern in the E- and H-plane is given by:

$$p_i(f, \theta) = \left[1 - \left(\frac{\theta}{\pi/2}\right)^{\alpha_i(f)}\right](\cos\theta)^{\beta_i(f)} + \gamma_i(f)\left(\frac{\theta}{\pi/2}\right)(\cos\theta)^{\delta_i(f)} \tag{6.1}$$

where $i = E, H$ and θ is the elevation angle. The behavior of the coefficients $[\alpha_i, \beta_i, \gamma_i, \delta_i]$ with respect to frequency is fitted with a polynomial of n^{th}-order[1] to NEC4 simulations [138]. Note that for this simulation only the 3×3 ground plane case is available. It should be noted that the normalized patterns were the ones to be analytically fitted, whereas absolute gain values are sparse in the existing literature, which prompted the re-simulation of the NEC4 pattern in absolute values and re-examination of its correct normalization.

---

[1] Different works throughout the years have used different values for the polynomial order. [120, 137] used a 3rd order polynomial while [134] used a 13th order polynomial.

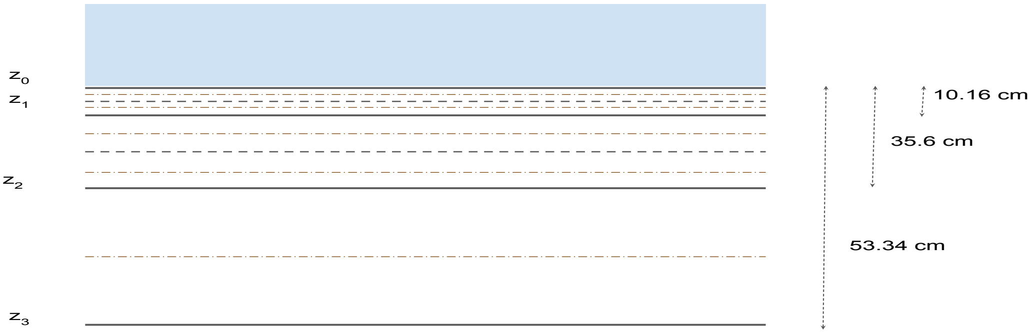

Figure 6.2. A 2D schematic view of the multi-layer splitting of soil half-infinite space z < 0, described this section. A number of different measurements were made at 3 specific depths z_i (10.16 cm, 35.56 cm and 53.34 cm) and then ensemble averaged. A numerical EM driven multi-layer modelling is then constructed with an iterative sub-layering scheme. See text and Alg. 1 for details.

I.II Improving the beam model

In this section, we incorporate the soil properties measured in-situ, describing more realistically the environmental conditions in which the data have been collected. Although not previously explored for the LEDA antennas, there are examples in the literature of similar studies where the soil is analysed as an homogeneous dielectric semi-infinite volume, discriminating only between dry and wet soil conditions [98], or a combination of both, as in [128].

One layer baseline model. For our new simulation we use FEKO[2]. We model the soil as a single half-infinite layer of constant complex permittivity and conductivity, namely:

$$\epsilon = \epsilon_0 \left(\epsilon_r + j \frac{\sigma}{2\pi f \epsilon_0} \right) \tag{6.2}$$

where ϵ_0 is the electrical permittivity of vacuum, ϵ_r is the dimensionless relative permittivity, σ is the conductivity in S/m, and f is the frequency in Hz. This quantity had been measured on site for different soil moisture condition corresponding to both dry and wet soil (see Tab. 6.1). We use this one-layer model as our baseline one since it is simple and relatively immune to numerical artefacts. We simulate the three different ground planes - 3×3, 10×10 and serrated as seen in Fig. 6.1.

Measurement driven three-layer modelling. We update the modelling just described adding the new available measurements for the soil complex permittivity. In constructing our first layered geometrical model, we adopted values at the nominal depths of Tab. 6.1. A thickness was also chosen for the simulated layers according to the measurement depths, and we ensemble averaged the permittivities of the available measurements. A full description of the measurement setup and campaign conducted by L. Greenhill is included in [139].

Note that the thickness of these three consecutive layers does not match with standard numerical accuracy criteria required by EM solvers. Despite this, we use

---

[2] `https://altairhyperworks.com/feko/`

these measurements to construct a three-layer soil model for the FEKO simulation ("measurements" column of Tab. 6.2).

Numerical EM driven multi-layer modelling. The thicknesses of the three-layer model are imposed by the depth of the available measurements and might not be sufficient for accurately representing a varying soil permittivity gradient. In order to solve the possible numerical issues connected to the thicknesses of the three-layer model we refine our electromagnetic simulations using more layers. Although the separation between two consecutive layers is subject to different discretisation rules according to each method, requesting a separation smaller than $\lambda/10$ is a widely used criterion. The standard FEKO method for any multi-layer substrate is a planar Green's function analytical solution embedded in the MoM formalism. A continuously varying permittivity is treated by means of properly discretising in layers, and a Transmission Line Green's Function (TLGF) approach is used by the solver. Details for this can be found in [140].

When considering the $\lambda/10$ rule to discretise the half-infinite space, we have to take into account the different phase velocity which implies a different wavelength in each layer. For a low-loss medium, such as soil ($\sigma \ll 2\pi f \epsilon_0$ when considering our available measurements), the phase velocity is $c_p = c_0/\epsilon_r$, where c_0 is the speed of light in vacuum. We shall split each of the previous three layers into sub-layers such that their thickness is less than or equal to $\lambda_p/10$, and then double these layers iteratively until a certain convergence criterion is satisfied. The algorithm which implements this iteration is presented in Alg. 1. In each iteration, we interpolate linearly to compute the new values of complex permittivity (`linInterp`), we merge them with the values of the previous iteration (`merge`), and we run a new FEKO simulation to calculate the gain pattern (`Gain`).

This iteration is applied both for relative permittivity and for conductivity in a square lattice fashion, and a maximum frequency $f_{\max} = 100$ MHz is used which provides a strong bound. By performing the first step of discretization, we conclude that each of the previous three layers of the dry soil should be divided into one or two sub-layers (see the grey dashed lines in Fig. 6.2). We then follow an iterative splitting by doubling these sub-layers (red dotted-dash lines in Fig. 6.2), in order to make an ever finer discretization. Wet soil conditions require a slightly finer splitting and are not reported in the schematic figure. The number of sub-layers used in the first iteration is reported in Tab. 6.2.

The iterative algorithm stops when a convergence threshold for the value of the gain at zenith is satisfied. We choose 0.1 dB which should be roughly similar to the numerical accuracy of FEKO. The number of layers needed for convergence are 40 and 56 layers for dry and wet conditions, respectively. The high number of layers to reach convergence is needed only for the serrated case but we assume it for all ground planes for convenience. We refer to this implementation as the converged model. Fig. 6.2 summarises the different multi-layer approaches listing their number of layers.

Fig. 6.3 shows the gain differences (in dB) between the converged case and the solution obtained with a smaller number of layers at all previous iterations. The analysis is repeated for all three different ground planes. We note the existence

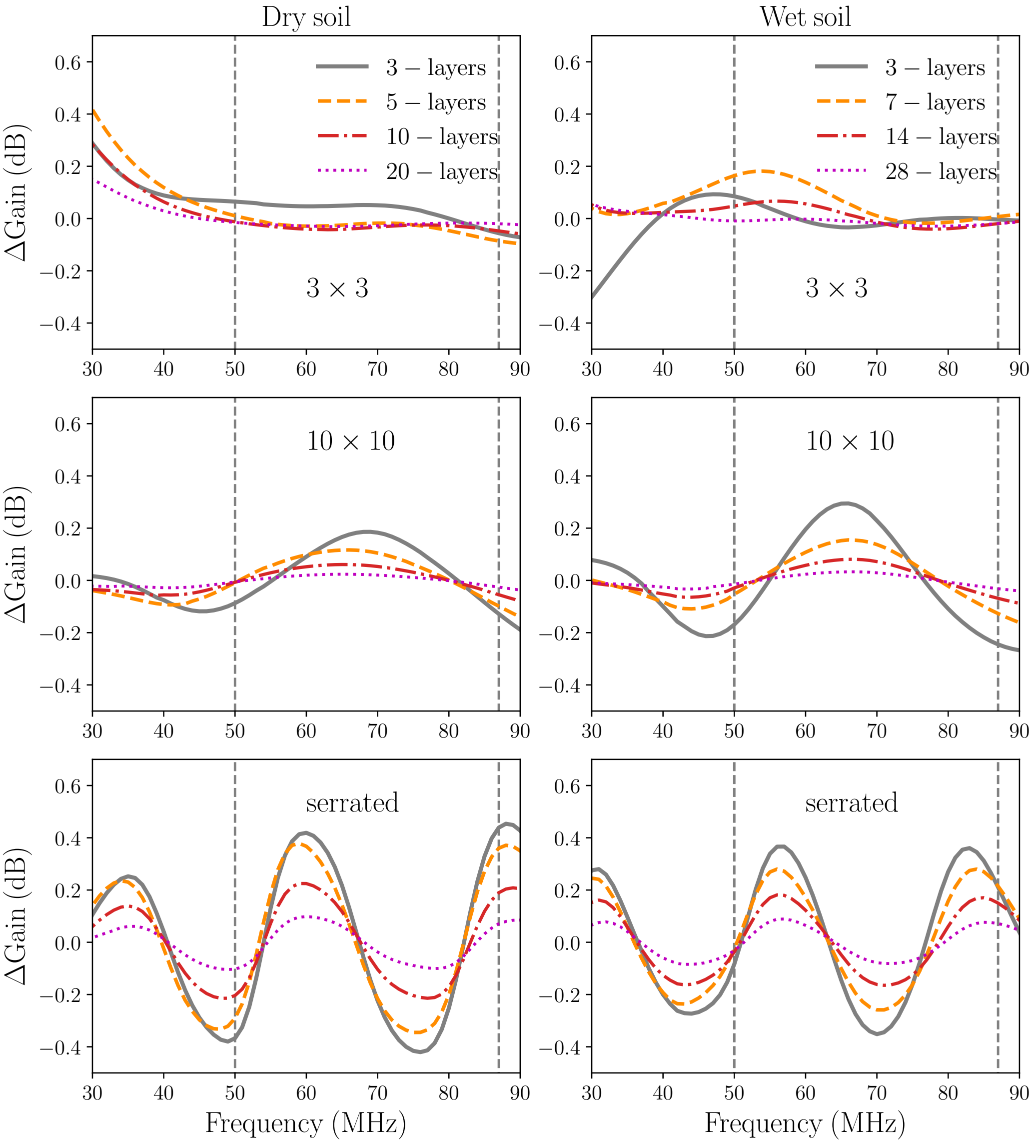

Figure 6.3. Gain at zenith dB difference of multi-layer implementations, calculated between the converged solution with 40 and 56 layers for dry and wet soil conditions, respectively, and solutions with fewer layers. Six cases are examined: different types of soil conditions (dry, wet) and different types of ground plane 3 × 3,10 × 10, serrated). The vertical dashed lines highlight the region where LEDA data are available.

```
$[\epsilon] \leftarrow [\epsilon_1, \epsilon_2, \epsilon_3]$;
$[\lambda_p] \leftarrow \frac{c_0 \epsilon_0}{f_{\max} \Re\{[\epsilon]\}}$;
$[\Delta\epsilon] \leftarrow [\epsilon_1, \epsilon_2 - \epsilon_1, \epsilon_3 - \epsilon_2]$;
$[N] \leftarrow [1, 1, 1]$;
$G_0 \leftarrow \mathrm{Gain}([\epsilon])$;
for $i = 0, 1, 2$ do
    $N_{init} \leftarrow \left\lceil \frac{|z_{i+1} - z_i|}{[\lambda_p]_{i+1}/10} \right\rceil$;
    $[\Delta\epsilon]_{i+1} \leftarrow \frac{[\Delta\epsilon]_{i+1}}{N_{init}}$;
    $[N]_{i+1} \leftarrow N_{init}$;
    $[\epsilon] \leftarrow \mathrm{merge}([\epsilon]_{1:i}, \mathrm{linInterp}([\epsilon]_{i+1}, [N]_{i+1}, [\Delta\epsilon]_{i+1})$;
end
$G_1 \leftarrow \mathrm{Gain}([\epsilon])$;
while $|G_1 - G_0| > 0.1 \ dBi$ do
    $G_0 \leftarrow G_1$;
    for $i = 0, 1, 2$ do
        $[\epsilon] \leftarrow \mathrm{merge}([\epsilon]_{1:[N]_i - 1}, \ldots$
            $\mathrm{linInterp}([\epsilon]_{[N]_i:[N]_{i+1}-1}, 2[N]_{i+1}, [\Delta\epsilon]_{i+1}/2))$;
    end
    $[\Delta\epsilon] \leftarrow \frac{[\Delta\epsilon]}{2}$;
    $[N] \leftarrow 2[N]$;
    $G_1 \leftarrow \mathrm{Gain}([\epsilon])$
end
```

Algorithm 1: Sub-layer splitting algorithm (see also Fig. 6.2) to achieve gain at zenith convergence of 0.1 dBi. [arg] indicates a vector-valued argument, while a subscript is used to index these values ($i_1 : i_2$ also indicates parsing from initial index i_1 to final index i_2). See text and appendix for details.

number of soil layers for multi-layer schemes			
	measurements	$\lambda_p/10$	converged
dry	3	5	40
wet	3	7	56

Table 6.2. Number of soil layers that were used in each of our 3 multi-layer models: $\lambda_p/10$ is for the first iteration of the algorithm, and converged is the final step of doubling that allows gain convergence to 0.1dB.

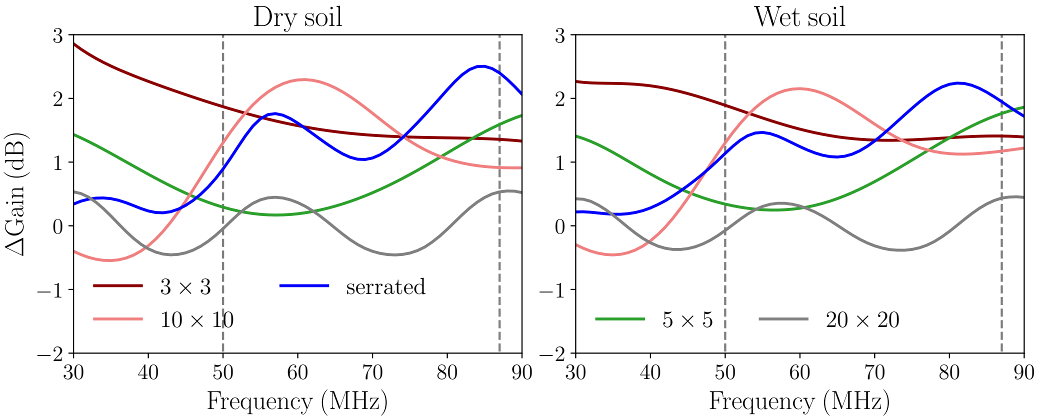

Figure 6.4. Gain at zenith dB difference of ground plane implementations, calculated between a reference model of an infinite PEC plane and the converged model of each ground plane as reported in the legend, for dry and wet soil conditions, respectively. An intermediate case of a 5 × 5 ground plane and a large 20 × 20 one, not examined elsewhere, are also shown. The vertical dashed lines in each panel highlight the region where LEDA data are available.

of periodic oscillations for the case of the 10 × 10 ground plane, with or without serrations. This fact highlights that successive implementations of sub-layers differ roughly by sinusoidal factors, which are still present when the ground plane gets bigger. This is a counter-intuitive conclusion, which might originate from sharp permittivity value transitions between consecutive layers (expressed in boundary conditions of the TLGF). The 3 × 3 ground plane performs better with respect to the oscillation, apart from a low-frequency drift off.

Finite size of the ground plane. Oscillation effects are also observed when comparing all finite sized ground planes with respect to an infinite Perfect Electric Conductor (PEC) plane solution. To demonstrate this, in Fig. 6.4 we subtract from the converged case the solution for an infinite PEC plane, for each of the considered ground planes. We also include a 5×5 and a 20×20 ground plane, as an intermediate and extreme case. The sinusoidal variations that can be seen imply that there are finite-size truncation/diffraction effects which need long electrical distances (i.e., distances as multiples of λ) to diminish. The amplitude and periodicity of these oscillations are different for each ground plane and depend on their size.

Having examined the effect of different ground planes, soil conditions as well as soil layering options, a comparative plot of zenith gain can best illustrate their effects before any chromaticity correction is calculated. For each ground plane and soil conditions, we present in Fig. 6.6 the baseline one-layer, the three-layer, and the converged multi-layer FEKO model. As expected, the 3x3 ground plane provides in most cases a lower gain, since there are more losses related to the part of the soil not covered by the ground plane. It is, however, the best one in terms of ground plane induced ripple, which has a lower frequency due to its smaller dimension. Note that concerns over the spectral structure of an underlying ground plane have already been addressed in other experiments such as SARAS3 [141, 122] that moved the antenna on a lake to minimise the chromatic response. The MIST experiment has opted instead for not deploying a ground plane and carefully characterise the ground properties. For an antenna configuration less sensitive to the ground properties than LEDA (which is facing downwards and is more coupled to any underlying structure), a larger ground plane is also expected to alleviate the problem. The EDGES team, for example, has used a 30 × 30 ground plane for their results [121].

We include in Fig. 6.6 for comparison the 3 × 3 ground plane solution obtained with the NEC4 pattern used in previous analysis. The NEC4 patterns have been scaled down using the radiation efficiency as calculated with FEKO data (see the next paragraph) since the NEC4 model was overestimating the gain by omitting the inclusion of soil losses in its gain calculation [142]. Despite this correction, the FEKO and NEC4 models differ by a factor of up to 1 dB across the frequency range of interest, a result that showcases the differences between numerical solvers.

Radiation efficiency. We present here the radiation efficiency $\eta_{\rm rad}$ as a function of frequency, which takes into account losses over all of the 3D antenna pattern. The radiation efficiency is calculated using the integral of the upper hemisphere far field patterns and the input power at the antenna port, given by FEKO. In Fig. 6.5, $\eta_{\rm rad}$ is shown for the three examined ground planes.

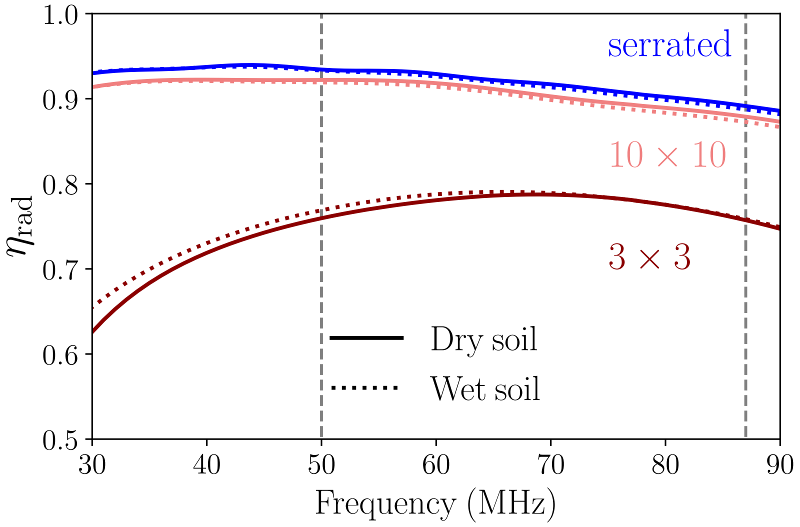

Figure 6.5. Radiation efficiency over frequency calculated for the three different cases of ground plane, using the FEKO solution outputs. Dry (solid lines) and wet (dotted lines) conditions for the baseline one-layer model are presented. The vertical dashed lines highlight the region where LEDA data are available.

As expected, the 3 × 3 ground plane presents more losses, with a clearer frequency dependence as well, since the efficiency is poorer at lower frequencies. A 10 × 10 ground plane with or without serrations is more appropriate to keep losses smaller than 10% in most of the frequency band, and quite more stable at the extremes, as they have a larger extent and allow for more power radiated below the horizon (> 90°) to be reflected back, contributing to the gain. The radiation efficiency is not constant and this affects the gain integral which is not 4π and varies with frequency. The beam integral is expected to vary significantly in the case of 3×3 ground planes, such that any normalisation of the beam pattern should be made separately for each frequency.

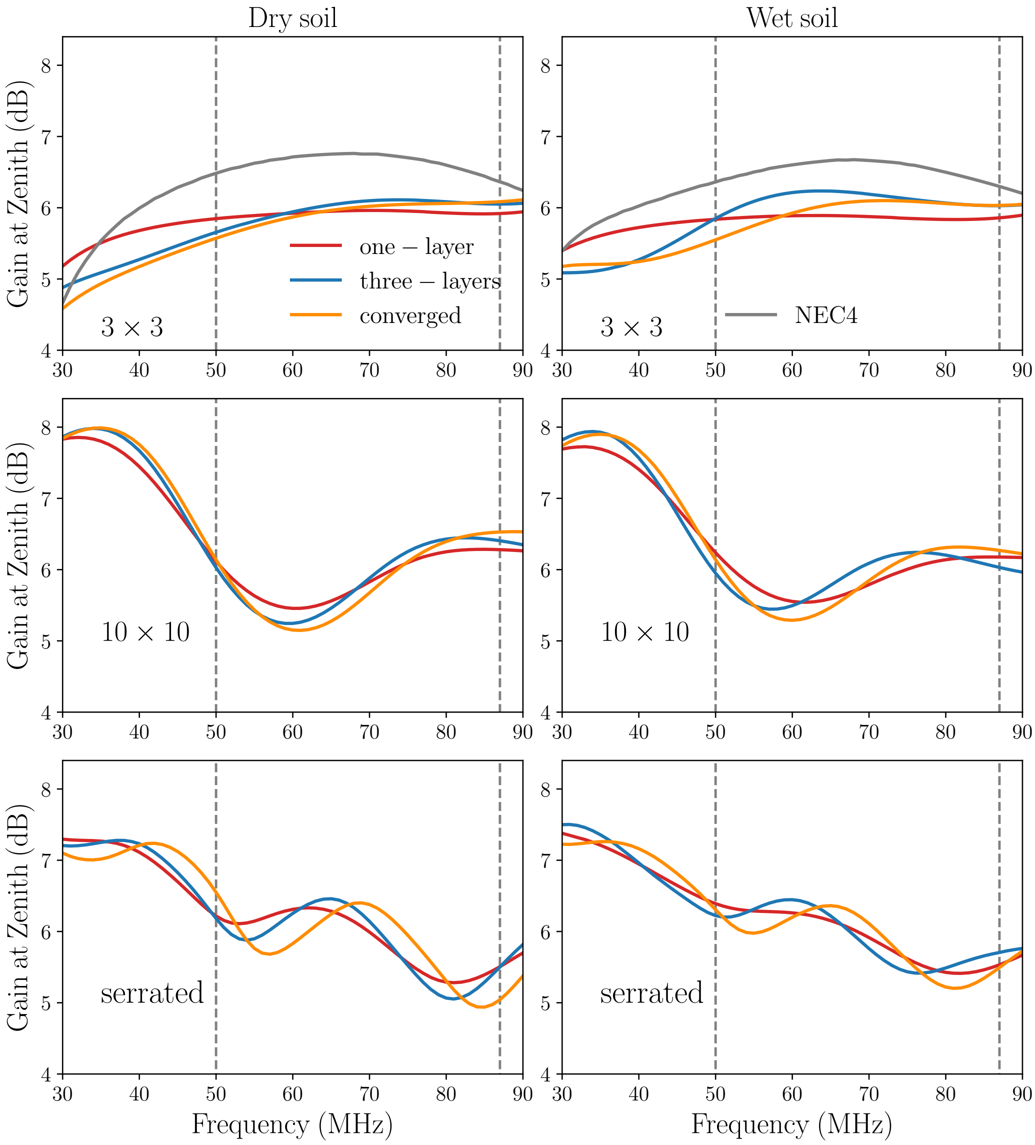

Figure 6.6. Gain at zenith of different multi-layer implementations, including the baseline model, a three-layer model, and the converged multi-layer model (40 and 56 layers for dry and wet soil conditions, respectively). Six cases are examined, as in Fig. 6.4. For the 3×3 ground plane, the NEC4 simulated model is also shown. The vertical dashed lines in each panel highlight the region where LEDA data are available.

Beam gain variation. As another assessment of the radiation pattern spectral robustness, we present a number of 2D colour-maps of the beam dB change in gain with respect to frequency in Fig. 6.7, for 4 azimuth angles $\phi = 0°$, $30°$, $60°$,$90°$, a criterion similar to that evaluated by [127]. This kind of plot is useful not only to confirm the sinusoidal-factor spectral periodicity due to the ground plane structure, but any other spatial effects which predominantly appear across zenith angle θ. It can be seen from the figure that these spatial variations are significant even for $\theta < 40°$, which compares with the Half-Power Beam Width of the antenna. Another interesting phenomenon is that the "phase" of this sinusoidal-factor variation is different for each elevation, which means that any analytic approach such as that of Eq. (6.1) with $\theta \times \cos(\theta)$ polynomial terms is not adequate to describe the complexity of the beam pattern.

The amplitude in azimuth angle diminishes when we cross from the E-plane ($\phi = 0°$) to the H-plane ($\phi = 90°$). The greatest variation both in terms of amplitude and number of complete cycles in the frequency range of interest is found for the serrated ground plane, which reaches as high as 0.2 dB/MHz in many $f - \theta$ sample points.

Beam chromaticity correction factor. Assuming a well-behaved beam with a small degree of chromaticity, the resulting spectra are expected to be smooth in frequency. Although not visible by eye in observed T_{ant} spectra, realistic beam shapes induce a non-smooth frequency structure in the measured sky temperature that complicates the signal reconstruction. As discussed in other works [143, 144, 145] a possible approach to alleviate the effect of the chromatic beam on the measured spectra is to correct the original spectra using the following factor:

$$B_{\mathrm{c}}(f, \mathrm{LST}) = \frac{\int_\Omega T_{\mathrm{sky}}(f_0, \mathrm{LST}, \hat{\mathbf{n}}')B(f, \hat{\mathbf{n}}')d\hat{\mathbf{n}}'}{\int_\Omega T_{\mathrm{sky}}(f_0, \mathrm{LST}, \hat{\mathbf{n}}')B(f_0, \hat{\mathbf{n}}')d\hat{\mathbf{n}}'} \frac{\int_\Omega B(f_0, \hat{\mathbf{n}}')d\hat{\mathbf{n}}'}{\int_\Omega B(f, \hat{\mathbf{n}}')d\hat{\mathbf{n}}'} \tag{6.3}$$

where $T_{\mathrm{sky}}(f, \mathrm{LST}, \hat{\mathbf{n}}')$ is a function of frequency f, LST and solid angle normal $\hat{\mathbf{n}}'$ representing the sky brightness temperature drifting with time over the antenna. We choose $f_0 = 75$ MHz as a reference frequency [143] since it is approximately central in our range. In this formulation the beam pattern $B(f, \hat{\mathbf{n}}')$ used is gain, so the second term on the right hand side of the equation can be proven to equal $\eta_{\mathrm{rad}}(f)/\eta_{\mathrm{rad}}(f_0)$.

We compute the beam chromaticity correction using the various beam models presented throughout Sec. I.II. In this computation, the Haslam 408 MHz full-sky map $T_{\mathrm{H}}(\hat{\mathbf{n}})$ [146] is used and scaled to different frequencies assuming a constant spectral index β:

$$T_{\mathrm{H;sky}}(f, \hat{\mathbf{n}}) = [T_{\mathrm{H}}(\hat{\mathbf{n}}) - T_{\mathrm{cmb}}] \left(\frac{f}{408\ \mathrm{MHz}}\right)^\beta + T_{\mathrm{cmb}}. \tag{6.4}$$

where $T_{\mathrm{cmb}} = 2.725$ K and $\beta = -2.5$. We also consider LST bins of 10 minutes and the full 24 h range for completeness when computing the correction.

It is interesting to first evaluate, as shown in Fig. 6.6, the difference between the analytic beam model previously used and the new FEKO baseline simulation, computing the chromaticity correction. This is reported in Fig. 6.8a. Differences reach a few percent especially around LST$\sim$ 18 when the Galactic center is transiting.

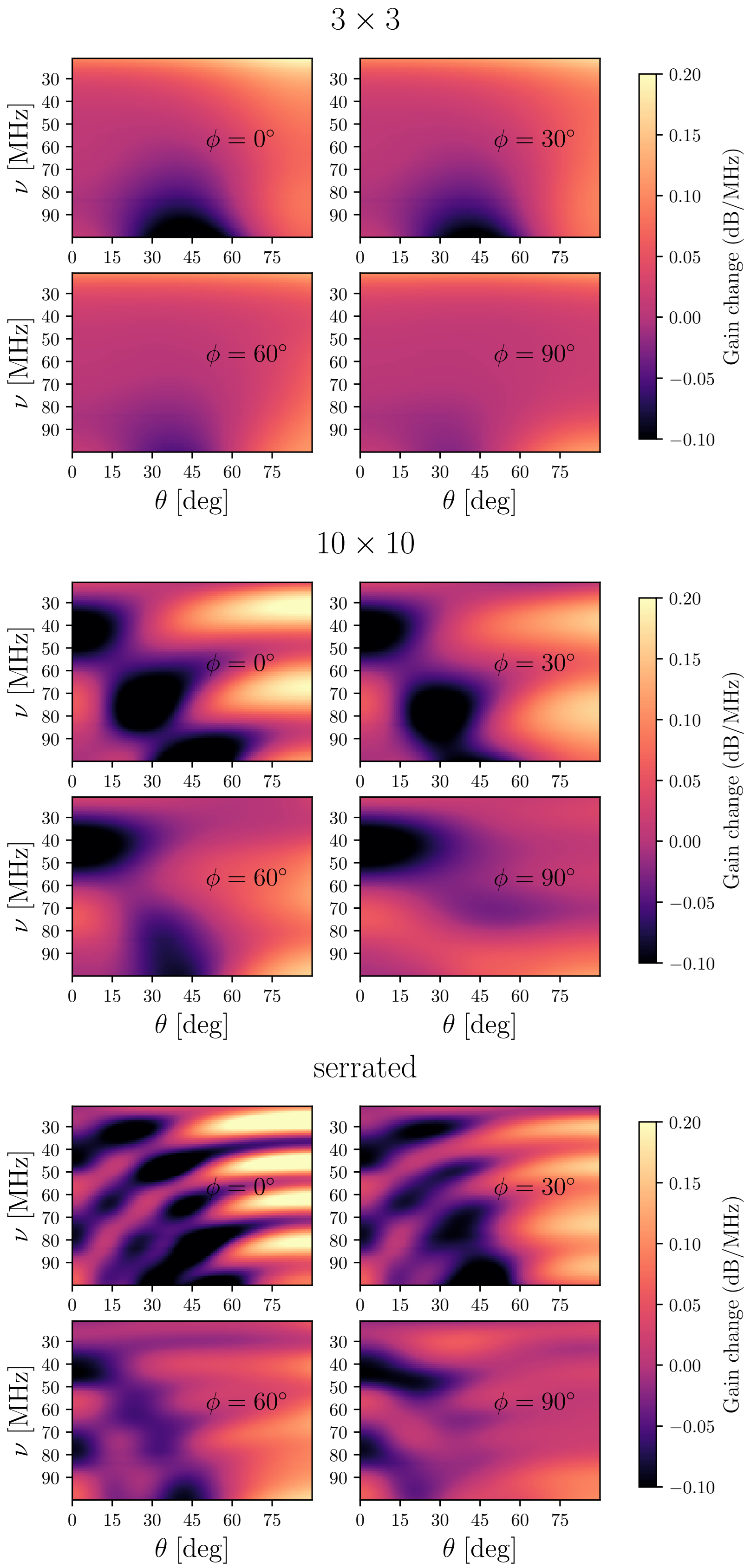

Figure 6.7. Beam gain change per unit frequency as a function of the angle θ and for four selected ϕ values (0, 30,60 and 90 degrees). We show here the one-layer model for dry soil condition.

We repeat the same exercise for the various FEKO beam models computed for this analysis. We show in Fig. 6.8 b-d, the difference between the dry and wet soil conditions for the three different ground planes. Differences are a fractional of percent but their structure presents different patterns for different ground plane shapes (see Fig. 6.3 and Fig. 6.6). The same structure of periodic peaks/troughs across frequency is seen in each constant LST line, as was observed for the dry/wet layer simulation, as well as the sub-layer convergence study. There is additionally a variation along LSTs in constant frequency lines that has to do with the beam coupling to a fainter/brighter sky.

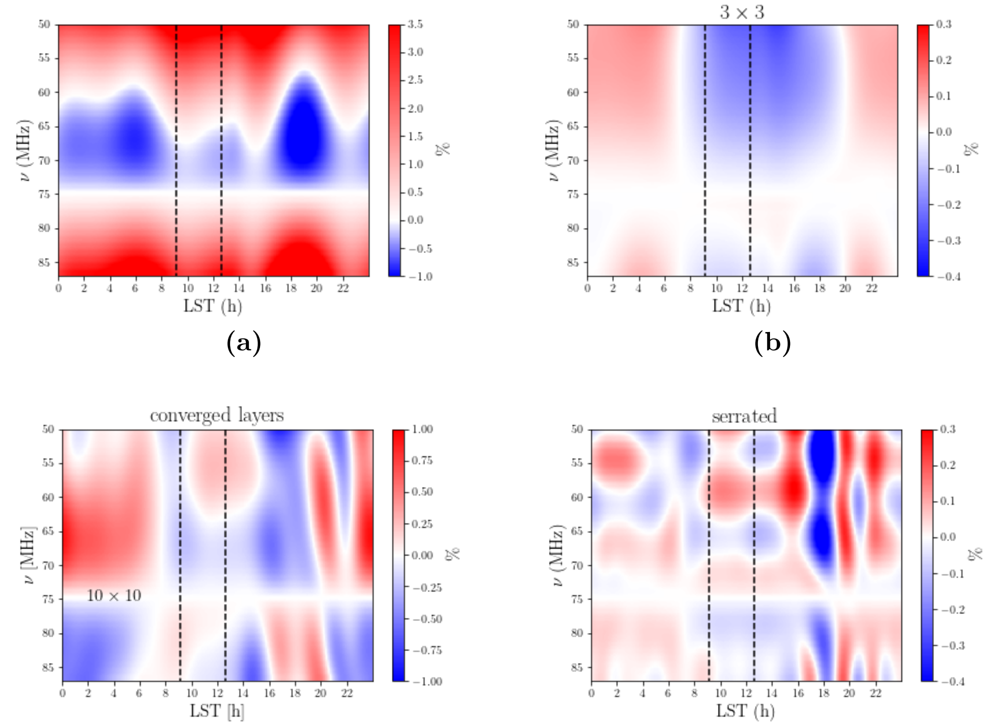

(a) **(b)**

(c) **(d)**

Figure 6.8. Percentage difference between the chromaticity correction factor B_c (Eq.(6.3)) computed for (a): the new baseline beam model and the analytic beam used in previous analyses, (b): for dry and wet soil conditions where we consider the one-layer FEKO model and the 3 m × 3 m ground plane, (c) the 10 m × 10 m ground plane and (d) the serrated ground plane. The dashed vertical lines highlight the LST range preferred for LEDA data analysis.

The continuation of this analysis included applying the chromaticity correction factor to mock-generated observational sky brightness temperature data which have certain levels of noise, and test the pipeline of bayesian signal extraction with respect to its accuracy, both in the foreground log-polynomial representation as well as finding the signal statistical characteristics. This further analysis was carried by collaborators of the author of this thesis and is included in a joint publication at the Monthly Notices of the Royal Astronomic Society [139].

The case of LWA

The detection of the aforementioned 21 cm global signal is not only possible with simple radiometer antennas, but also with arrays of such antennas using proper beamforming techniques. As outlined in [147], an important issue to be addressed in such approaches is the correct characterization of both the primary beam and the sidelobes of a beamforming array, so as to result in more realistic priors. We are going to explore in this section the spectral response of the LWA-OVRO station employing full-wave simulations, both at EEP level and at station beam. The results of previous analyses are corroborated, while some mutual coupling effects of the beam are shown. These results are preliminary but still show the importance of incorporating full-scattering into the signal extraction pipelines.

The Long Wavelength Array 1 (LWA1), located at the OVRO Valley in New Mexico, in USA, is a low-frequency radiotelescope operating at approximately 10-88 MHz, and is comprised of 256+2 antennas pseudorandomly distributed within a circular area of a 55 m radius. The antennas are the same ones examined in Sec. I, while the 2 extra antennas are outrigger ones, outside the station radius. Details on the operation of LWA can be found in [148], [136]; even though the shape of the antenna is the same, a different and simpler front-end is used for these antennas with respect to the outrigger ones used for LEDA.

A 256 LWA element array was simulated exciting the X-polarized port of each antenna and terminating the Y-polarized port with a 100 Ω load. All inactive elements were also loaded with 100 Ω in their X- and Y-polarized ports, so the Embedded Element Patterns (EEPs) computed have a Z_g reference. We also computed the antenna S-parameters of the full array. The ground plane of each antenna was modelled as a 3 m × 3 m solid rectangle. It is important in this case to model the soil, since the antenna ground planes sparsely cover the area in-between and so soil effects should not only affect the lateral antennas (as in the case of SKA-Low); this was modelled using the one-layer, dry condition parameters reported in Sec. I.II. The configuration of the array is shown in Fig. 6.9.

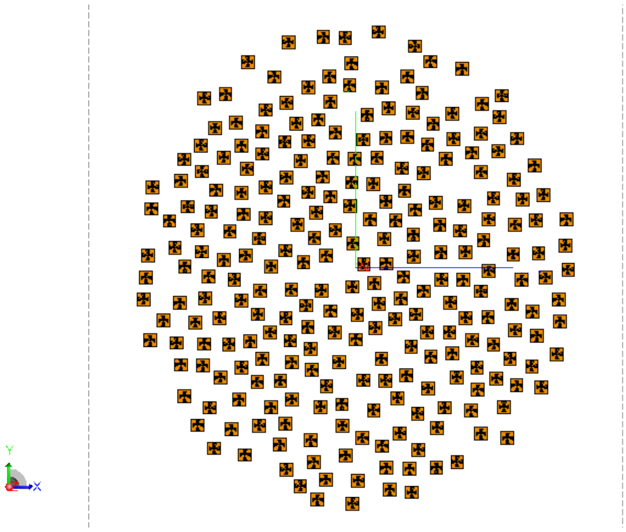

Figure 6.9. LWA array geometry configuration on the XY plane

Embedded Element Patterns. The array was simulated in FEKO using a 32-core processor system in parallel, with 503GB of RAM. Low-frequency MoM stabilisation was also enabled in FEKO, since there were warnings issued concerning the loss power calculated on the passive terminations being higher than the input power. Some further investigation confirmed that this was the effect of some pairs of antennas approaching a parallel configuration from their parallel-in-echelon, which ensues from the random nature of their distribution. Some details of our computation and handling of data are also provided in Appendix B.

We first present some plots of the Z_g-EEPs as directivity at zenith (in dB), in a number of frequencies: 20, 38 and 74 MHz, in a scatter form (all data points shown). As a reference, an isolated element pattern and the mean of all EEPs are also plotted, with dashed lines and rectangles respectively. We notice that the mean values are lower, higher and almost equal to the isolated element pattern, the higher the frequency goes. The scatter around this mean is higher at 38 MHz, lower at 20 MHz and somewhat skewed at 74 MHz.

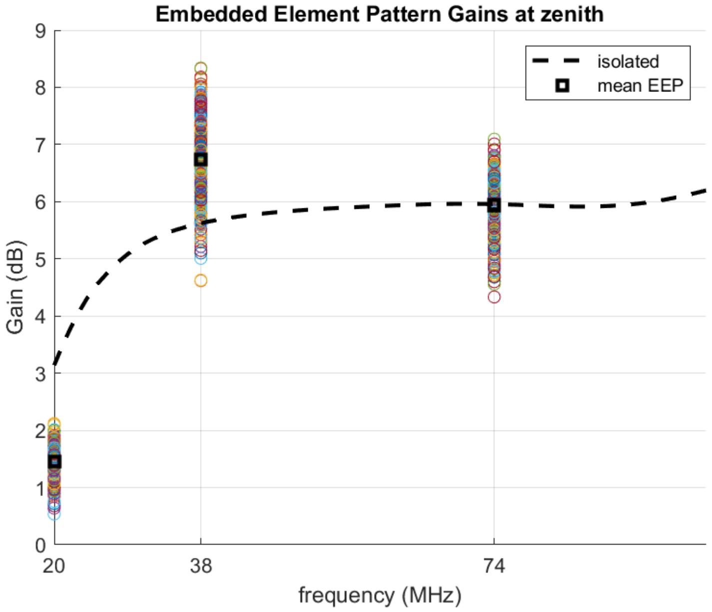

Figure 6.10. Z_g-EEP Gain scatter plot (3 frequencies)

Next we present the Z_g-EEPs as directivities, normalized by the directivity of the isolated element pattern (in dB), as a function of elevation angle θ, at the same frequencies, along with the mean EEP. Both H-plane ($\phi = 0°$) as well as E-plane ($\phi = 90°$) are presented. Our findings here agree qualitatively with previously reported results by Ellingson [148]. More specifically:

- at 20 MHz the behaviour across elevation seems to fall off for the E-plane, while it is relatively constant for the H-plane. Too high or low values close to the horizon (practically when $\theta > 60°$) are unreliable since both the nominator and denominator are low.
- at 38 MHz the E-plane the results are similar, with a more rapid fall-off of the

E-plane curve and less numerical artefacts close to the horizon. The *H*-plane is also similar but the scattering of EEPs seems to have more outliers.

- at 74 MHz the mean value changes behaviour in both planes, and it does not present a maximum at zenith. Low elevation angles seem to have a smaller dynamic range of scattering, especially in the *H*-plane, while it becomes more unpredictable at higher elevations.

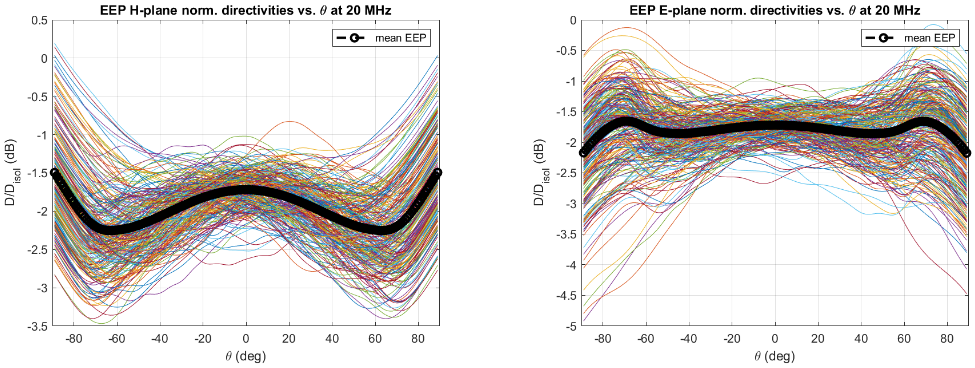

(a) 20 MHz E-plane **(b)** 20 MHz H-plane

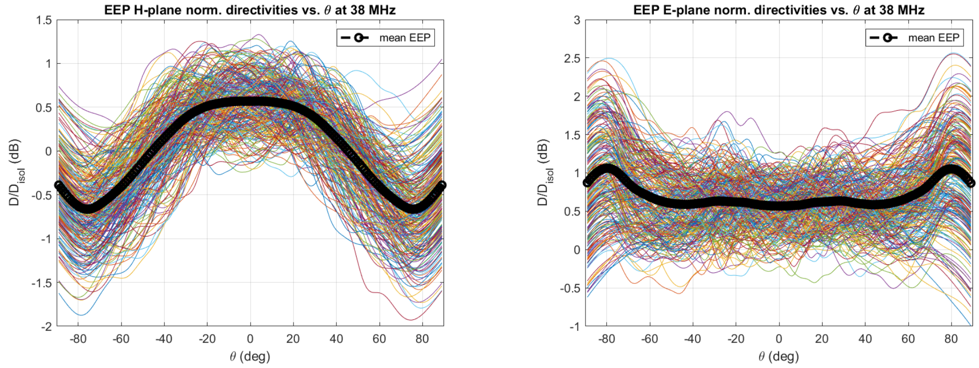

(c) 38 MHz E-plane **(d)** 38 MHz H-plane

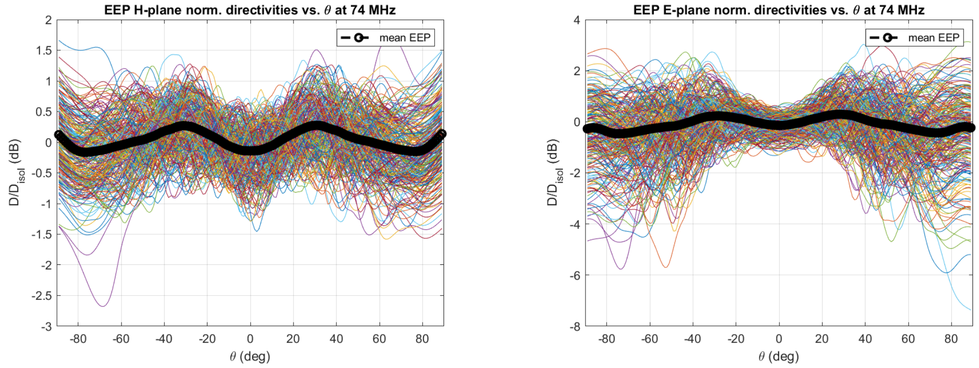

(e) 74 MHz E-plane **(f)** 74 MHz H-plane

Figure 6.11. Normalized gain *E*-plane (left) and *H*-plane (right) scatter across θ

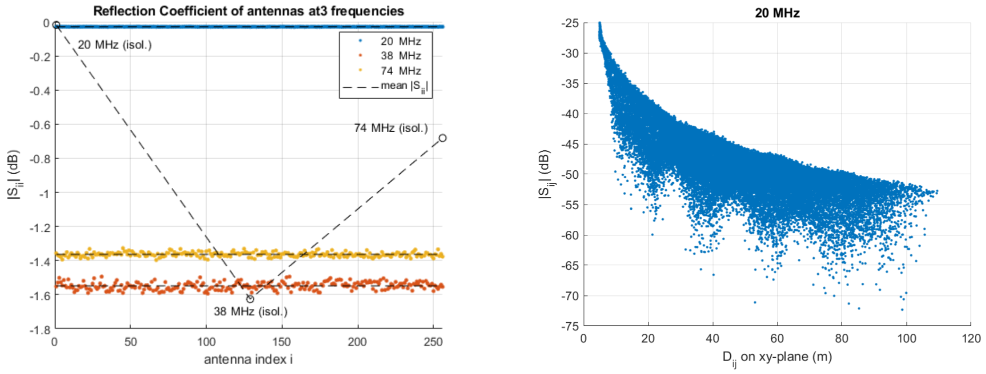

(a) $|S_{ii}|$ of all 256 antennas **(b)** $|S_{ij}(D_{ij})|$ at 20 MHz

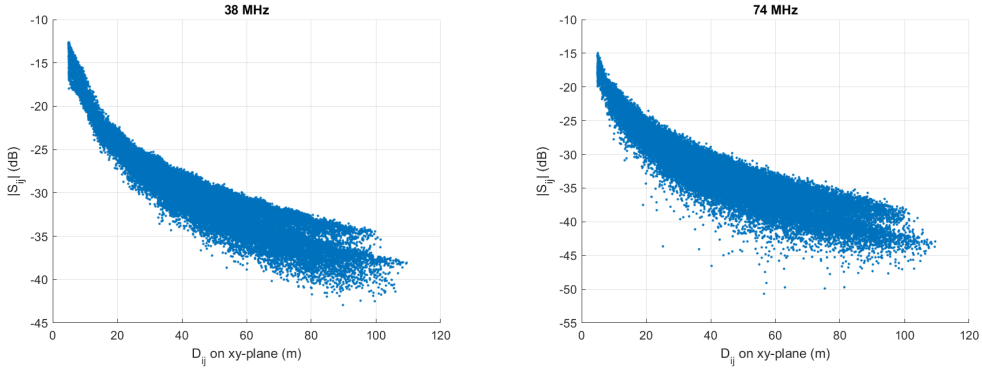

(c) $|S_{ij}(D_{ij})|$ at 38 MHz **(d)** $|S_{ij}(D_{ij})|$ at 74 MHz

Figure 6.12. S-parameters (dB) of a full X-polarized LWA array

S parameters of a full array and EEP transformation. In this section we present the S-parameter results for a full X-polarized LWA array. At every iteration the Y-polarized ports were terminated at 100 Ω. The reflection coefficients $|S_{ii}|$, $i \in \{1, \ldots, 256\}$, in dB, are presented in Fig. 6.12a, at the 3 examined frequencies, along with their mean value and the isolated element reflection values (annotated). All the other 3 subfigures are scatter plots of all the $256 \cdot (256 - 1)/2$ transmission coefficients $|S_{ij}|$, $i < j$, at the 3 same frequencies, as functions of the distance D_{ij} between the 2 elements i, j. As expected, as the distance increases, the mutual coupling and thus the $|S_{ij}|$ drops. It is also interesting to confirm the stronger mutual coupling at 38 MHz, which for small distances can reach around -12 dB. Same values are also visible for 74 MHz, where the electric distance (distance/wavelength) is higher for the same distance values. In general, the closer the examined frequency is to the resonances of the LWA antenna [138], the more susceptible it is to mutual coupling phenomena. As for the reflections, we note a larger deviation from the isolated pattern at 74 MHz. The poor matching at 20 MHz explains the unstable results of EEPs at that frequency; we again deem these results unreliable. The extremes of the $|S_{ij}|$ values serve as useful bounds in array reception models which include mutual coupling, such as [103],[101].

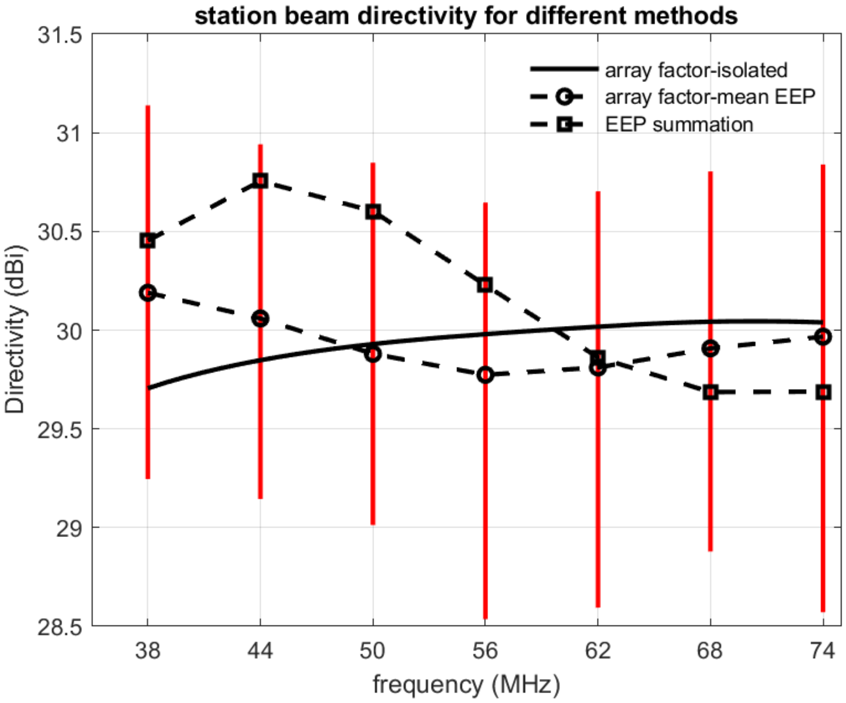

Figure 6.13. Station beam zenith directivity over a 6 MHz sampled range of 7 points, comparing 3 different methods.

Station beam. In this paragraph, a calculation of the station beam is performed using the Z_g-EEPs and the S-parameter results. We are going to use the $Z_g = 100\ \Omega$ terminated ports, and a unit excitation for all ports without phasing, that is $\bar{V}_g = \begin{pmatrix} 1 \cdots 1 \end{pmatrix}^T$. Then the station beam electric field pattern is for this excitation:

$$\begin{pmatrix} \vec{E}^{Z_g}_{st,\theta} & \vec{E}^{Z_g}_{st,\phi} \end{pmatrix} = \sum_k \begin{pmatrix} \vec{E}^{Z_g}_{k,\theta} & \vec{E}^{Z_g}_{k,\phi} \end{pmatrix} \tag{6.5}$$

Note that in this formulation the phasing factor $e^{j2\pi\left(\frac{x_k}{\lambda}\cos\theta\cos\phi+\frac{y_k}{\lambda}\cos\theta\sin\phi\right)}$ is embedded in the EEPs. We will also consider a simpler approach using the array factor, which is just summing all these exponentials and multiplying the absolute value of the sum with the isolated element electric field pattern.

First, and similar to Fig. 6.10, a frequency response of the station beam in more sampled points, with a frequency step of 6 MHz, between 38 and 74 MHz, is presented in Fig. 6.13. The curve of the EEP calculated station beam is compared with the array factor method using the isolated element pattern (dashed line), as well as using the mean of the EEPs, while the extremes are added as red bars on the EEP-calculated station beam points. These extremes are again an array factor approach using the EEP minimum and maximum. Importantly, the spectral smoothness of the zenith beam response is altered by taking into account all the mutual coupling phenomena, and is not well captured by the mean-EEP array factor approach which is also a complex spectral variation. Such spectral variations can also be quantified by the joint foreground and 21 cm bayesian estimation techniques we have used in [139].

Finally, Fig. 6.14 shows the *H*-plane and *E*-plane cuts of the station beam at the 3 chosen frequencies. We also include here a direct simulation of the station beam using FEKO and defining unit sources in all of the X-polarized ports, to confirm the computed results using the EEPs. We notice that the EEP summation and direct FEKO simulation agree excellently at all frequencies. Apart from confirming the zenith trend observed in Fig. 6.10, the sidelobe structure seems to be well approximated by the array factor technique, even though mutual coupling effects are ignored. Differences in the sidelobe maximum level are important to determine whether excess noise can impact on the 21 cm signal detection.

Discussion and future work. The beamforming technique of detecting the *global* 21 cm cosmological signal is a topic under recent investigation. It is important that the uncertainty here comes from the spectral contamination induced by means of the sidelobe noisy reception of the sky signal, while the primary beam can be modelled with good accuracy by a gaussian [147], [149]. The added advantage of this approach is that the system is more versatile in drift-scan observations, since steering the beam can lead to different patches of the sky accounting for the signal integration at a specified LST range. Redundant elements can also be considered dormant in steering the beam and deciding its optimal shape.

Quite an interesting topic for future studies is the inclusion of priors known from the accurate beam modelling of such arrays, using full-wave solvers. In this framework, our presented results could be used in order to approximate the beam with parametrized analytic models, whereby the parameters can be extracted by optimization strategies [149], [150]. Furthermore, the calculated set of EEPs is also used in novel beamforming techniques, such as in [150], [21, Ch. 10], [27]. This means that the optimization problem of controlling both the primary beam and the sidelobes can accurately be solved by setting certain constraints and calculating the desired weights. For example, the Minimum Variance Distortionless Response (MVDR) with linear constraints (LC) is a promising method of creating low-sidelobe, spectrally pure beams. Interesting work has also been done by Di Lullo et al. in [151], [152] to create an achromatic beamforming in a custom way for the LWA-SV array.

Finally, the bayesian framework of detection can also be revisited to account for the complexity of the different parameters affecting the spectral response of the observational data. In preparation for future data analysis, the REACH project has developed a software pipeline that incorporates the beam effects more thoroughly, coupled with a non-trivial scaling in frequency of the foreground [145]. This strategy, although computationally costly, leads to robust 21 cm global signal extraction in simulations and can thus enable better informed optimisation of antenna design [125], [153].

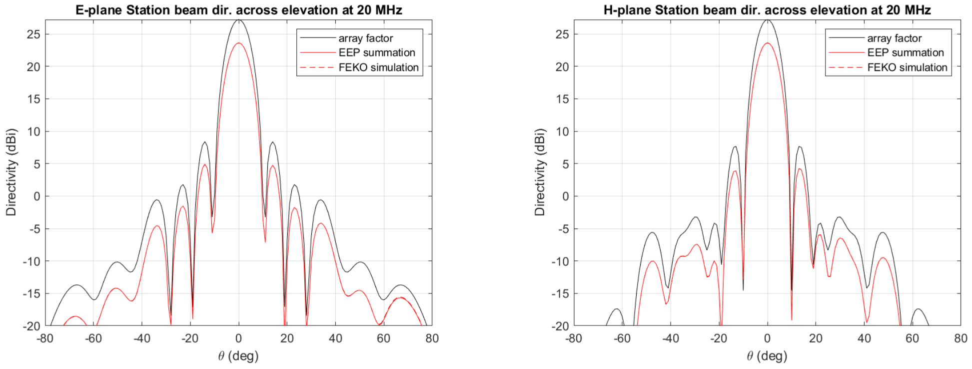

(a) E-plane G_{st} $-$ θ at 20 MHz **(b)** H-plane G_{st} $-$ θ at 20 MHz

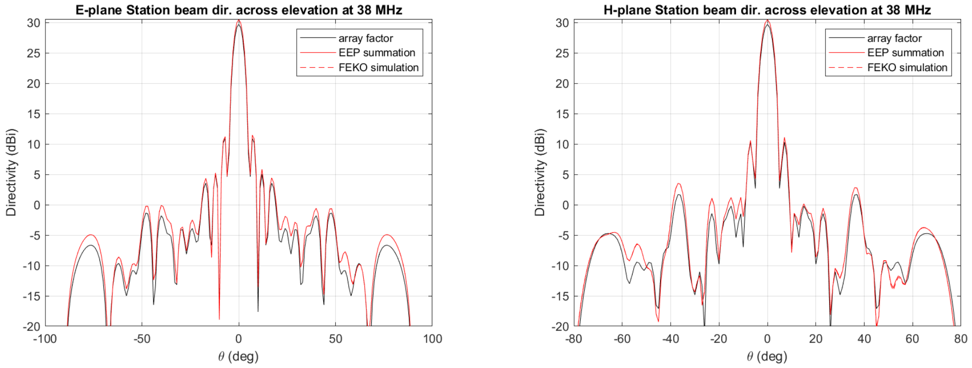

(c) E-plane G_{st} $-$ θ at 38 MHz **(d)** H-plane G_{st} $-$ θ at 38 MHz

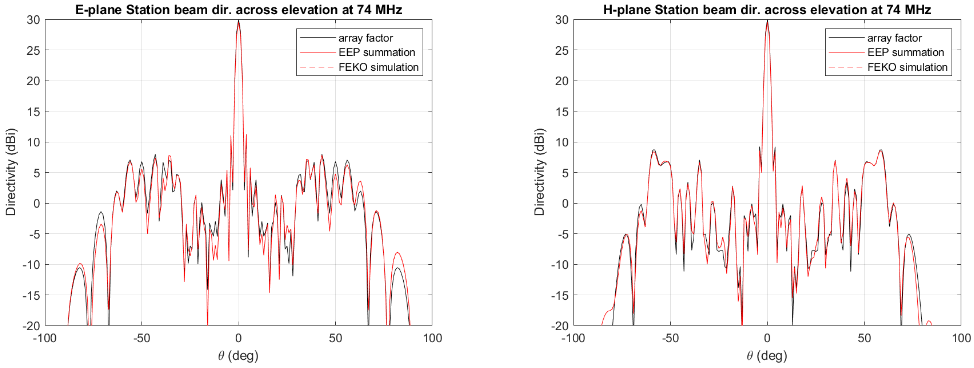

(e) E-plane G_{st} $-$ θ at 74 MHz **(f)** H-plane G_{st} $-$ θ at 74 MHz

Figure 6.14. Station beam gain across across elevation for 3 frequencies, in the E-plane (left) and H-plane (right), for the case of synthesis using the array pattern, summing the Z_g-EEPs, and direct simulation with FEKO.

Bibliography

[1] H. C. Ko. On the reception of quasi-monochromatic, partially polarized radio waves. *Proceedings of the IRE*, 50(9):1950–1957, 1962.

[2] T.L. Wilson and S. Hüttemeister. *Tools of Radio Astronomy - Problems and Solutions*. Astronomy and Astrophysics Library. Springer International Publishing, 2018.

[3] J.J. Condon and S.M. Ransom. *Essential Radio Astronomy*. Princeton Series in Modern Observational Astronomy. Princeton University Press, 2016.

[4] R.E. Collin. *Antennas and Radiowave Propagation*. International student edition. McGraw-Hill, 1985.

[5] A.R. Thompson, J.M. Moran, and G.W. Swenson. *Interferometry and Synthesis in Radio Astronomy*. Astronomy and Astrophysics Library. Springer International Publishing, 2017.

[6] Peter E. Dewdney, Peter J. Hall, Richard T. Schilizzi, and T. Joseph L. W. Lazio. The square kilometre array. *Proceedings of the IEEE*, 97(8):1482–1496, 2009.

[7] R. Braun, T. Bourke, J. A. Green, E. Keane, and J. Wagg. Advancing Astrophysics with the Square Kilometre Array. In *Advancing Astrophysics with the Square Kilometre Array (AASKA14)*, page 174, April 2015.

[8] Julián Garrido, Laura Darriba, Susana Sánchez-Expósito, Manuel Parra-Royón, Javier Moldón, María Á. Mendoza, Sebastián Luna-Valero, Antxón Alberdi, Isabel Márquez, and Lourdes Verdes-Montenegro. Toward a Spanish SKA Regional Centre fully engaged with open science. *Journal of Astronomical Telescopes, Instruments, and Systems*, 8(1):011004, 2021.

[9] Pietro Bolli, Lorenzo Mezzadrelli, Jader Monari, Federico Perini, Alberto Tibaldi, Giuseppe Virone, Mirko Bercigli, Lorenzo Ciorba, Paola Di Ninni, Maria Grazia Labate, Vittorio Giuseppe Loi, Andrea Mattana, Fabio Paonessa, Simone Rusticelli, and Marco Schiaffino. Test-driven design of an active dual-polarized log-periodic antenna for the square kilometre array. *IEEE Open Journal of Antennas and Propagation*, 1:253–263, 2020.

[10] Eloy de Lera Acedo, Nima Razavi-Ghods, N Troop, N Drought, and A J Faulkner. Skala, a log-periodic array antenna for the ska-low instrument:

design, simulations, tests and system considerations. *Experimental Astronomy*, 39:567–594, 2015.

[11] Eloy de Lera Acedo and B Wackley. Skala3: An optimized antenna and lna design for enhanced ska1-low passband calibratability. 2017.

[12] P Benthem, R Wayth, E de Lera Acedo, K Zarb Adami, MONICA Alderighi, Carolina Belli, Pietro Bolli, T Booler, Josef Borg, JW Broderick, et al. The aperture array verification system 1: system overview and early commissioning results. *Astronomy & Astrophysics*, 655:A5, 2021.

[13] Giulia Macario, Giuseppe Pupillo, Gianni Bernardi, Pietro Bolli, Paola Di Ninni, Giovanni Comoretto, Andrea Mattana, Jader Monari, Federico Perini, Marco Schiaffino, Marcin Sokolowski, Randall Wayth, Jess Broderick, Mark Waterson, Maria Grazia Labate, Riccardo Chiello, Alessio Magro, Tom Booler, Andrew McPhail, Dave Minchin, and Raunaq Bhushan. Characterization of the SKA1-Low prototype station Aperture Array Verification System 2. *Journal of Astronomical Telescopes, Instruments, and Systems*, 8(1):011014, 2022.

[14] Maria G. Labate, Mark Waterson, Bassem Alachkar, Aniket Hendre, Peter Lewis, Marco Bartolini, and Peter Dewdney. Highlights of the Square Kilometre Array Low Frequency (SKA-LOW) Telescope. *Journal of Astronomical Telescopes, Instruments, and Systems*, 8(1):011024, 2022.

[15] Pietro Bolli, David B. Davidson, Robert Braun, Paola Di Ninni, and Daniel Ung. Evaluating an alternate layout for the ska-low aperture array stations using computational electromagnetic simulations. In *2022 International Conference on Electromagnetics in Advanced Applications (ICEAA)*, pages 200–205, 2022.

[16] Robert Lehmensiek and Dirk I.L. de Villiers. On the performance of the ska mid-frequency array's reflector system and its feeds. In *2019 URSI Asia-Pacific Radio Science Conference (AP-RASC)*, pages 1–3, 2019.

[17] Robert Lehmensiek, Isak P. Theron, and Dirk I. L. de Villiers. Deriving an optimum mapping function for the ska-shaped offset gregorian reflectors. *IEEE Transactions on Antennas and Propagation*, 63(11):4658–4666, 2015.

[18] Robert Lehmensiek, Isak P. Theron, and Dirk I.L. de Villiers. An investigation of offset-fed beams on the proposed ska dishes with various degrees of shaping. In *2015 9th European Conference on Antennas and Propagation (EuCAP)*, pages 1–4, 2015.

[19] Alice Pellegrini, Jonas Flygare, Isak P. Theron, Robert Lehmensiek, Adriaan Peens-Hough, Jamie Leech, Michael E. Jones, Angela C. Taylor, Robert E. J. Watkins, Lei Liu, Andre Hector, Biao Du, and Yang Wu. Mid-radio telescope, single pixel feed packages for the square kilometer array: An overview. *IEEE Journal of Microwaves*, 1(1):428–437, 2021.

[20] Jayashree Roy, Michael Pleasance, Stephen Harrison, Andreas Wolfgang, and Kris Caputa. Overview of the single pixel feed receiver system of square kilometer array mid telescope. In *2022 3rd URSI Atlantic and Asia Pacific Radio Science Meeting (AT-AP-RASC)*, pages 1–4, 2022.

[21] Karl F. Warnick, Rob Maaskant, Marianna V. Ivashina, David B. Davidson, and Brian D. Jeffs. *Phased Arrays for Radio Astronomy, Remote Sensing, and Satellite Communications.* EuMA High Frequency Technologies Series. Cambridge University Press, 2018.

[22] J.G. Bij de Vaate, J. Bast, P. Benthem, M. Gerbers, S.J. Wijnholds, T. Booler, T. Colgate, B. Crosse, D. Emrich, P. Hall, B. Juswardy, D. Kenney, F. Schlageuhaufer, M. Sokolowski, A. Sutinjo, D. Ung, R. Wayth, A. Williams, M. Alderighi, P. Bolli, G. Comoretto, A. Mattana, J. Monari, G. Naldi, F. Perini, G. Pupillo, S. Rusticelli, M. Schiaffino, F. Schilliro, A. Aminei, R. Chiello, M. Jones, J. Baker, R. Bennett, R. Halsall, G. Kaligeridou, M. Roberts, H. Schnetler, J. Abraham, E. De Lera Acedo, A.J. Faulkner, N. Razavi-Ghods, D. Cutajar, A. DeMarco, A. Magro, and K. Zarb Adami. The ska1-low telescope: The station design and prototyping. In *2018 2nd URSI Atlantic Radio Science Meeting (AT-RASC)*, pages 1–1, 2018.

[23] U. Kiefner, R. B. Wayth, D. B. Davidson, and M. Sokolowski. Holographic calibration of phased array telescopes. *Radio Science*, 56(5):1–8, 2021.

[24] Cornelis R. Wilke, Stefan J. Wijnholds, and Jacki Gilmore. Calibratability of aperture arrays using self-holography. *IEEE Transactions on Antennas and Propagation*, 69(8):4527–4537, 2021.

[25] Stefan J. Wijnholds. Embedded element patterns in hierarchical calibration of large distributed arrays. In *2020 XXXIIIrd General Assembly and Scientific Symposium of the International Union of Radio Science*, pages 1–4, 2020.

[26] Maria Grazia Labate, Alice Pellegrini, Mark Waterson, and Robert Laing. How electromagnetic models can improve astronomical observations in the square kilometre array radio telescope. In *2023 17th European Conference on Antennas and Propagation (EuCAP)*, pages 1–5, 2023.

[27] Zaharias D. Zaharis, Ioannis P. Gravas, Pavlos I. Lazaridis, Traianos V. Yioultsis, Christos S. Antonopoulos, and Thomas D. Xenos. An effective modification of conventional beamforming methods suitable for realistic linear antenna arrays. *IEEE Transactions on Antennas and Propagation*, 68(7):5269–5279, 2020.

[28] Daniel J. Ludick, Rob Maaskant, David B. Davidson, Ulrich Jakobus, Raj Mittra, and Dirk de Villiers. Efficient analysis of large aperiodic antenna arrays using the domain green's function method. *IEEE Transactions on Antennas and Propagation*, 62(4):1579–1588, 2014.

[29] T. D. Carozzi and G. Woan. A fundamental figure of merit for radio polarimeters. *IEEE Transactions on Antennas and Propagation*, 59(6):2058–2065, 2011.

[30] R.E. Collin. *Field Theory of Guided Waves*. IEEE Press Series on Electromagnetic Wave Theory. Wiley, 1990.

[31] Donald R. Wilton. Review of current status and trends in the use of integral equations in computational electromagnetics. *Electromagnetics*, 12(3-4):287–341, 1992.

[32] Rob Maaskant. *Analysis of large antenna systems*. PhD thesis, Eindhoven University of Technology, 2010.

[33] T. Sarkar. A note on the choice weighting functions in the method of moments. *IEEE Transactions on Antennas and Propagation*, 33(4):436–441, 1985.

[34] S. Rao, D. Wilton, and A. Glisson. Electromagnetic scattering by surfaces of arbitrary shape. *IEEE Transactions on Antennas and Propagation*, 30(3):409–418, 1982.

[35] David B. Davidson. Convergence of the mpie galerkin mom thin wire formulation. *IEEE Transactions on Antennas and Propagation*, 69(10):7073–7078, 2021.

[36] S.U. Hwu, D.R. Wilton, and S.M. Rao. Electromagnetic scattering and radiation by arbitrary conducting wire/surface configurations. In *1988 IEEE AP-S. International Symposium, Antennas and Propagation*, pages 890–893 vol.2, 1988.

[37] M.M. Ney. Method of moments as applied to electromagnetic problems. *IEEE Transactions on Microwave Theory and Techniques*, 33(10):972–980, 1985.

[38] J. Song, Cai-Cheng Lu, and Weng Cho Chew. Multilevel fast multipole algorithm for electromagnetic scattering by large complex objects. *IEEE Transactions on Antennas and Propagation*, 45(10):1488–1493, 1997.

[39] J Laviada, Rob Maaskant, and R Mittra. Macro basis function framework for solving maxwell's equations in surface integral equation form. *The FERMAT Journal*, 3:1–16, 2014.

[40] V. V. S. Prakash and Raj Mittra. Characteristic basis function method: A new technique for efficient solution of method of moments matrix equations. *Microwave and Optical Technology Letters*, 36(2):95–100, 2003.

[41] Rob Maaskant, Raj Mittra, and Anton Tijhuis. Fast analysis of large antenna arrays using the characteristic basis function method and the adaptive cross approximation algorithm. *IEEE Transactions on Antennas and Propagation*, 56(11):3440–3451, 2008.

[42] Mengmeng Li, Dazhi Ding, Alexander Heldring, Jun Hu, Rushan Chen, and Giuseppe Vecchi. Low-rank matrix factorization method for multiscale simulations: A review. *IEEE Open Journal of Antennas and Propagation*, 2:286–301, 2021.

[43] Matthews Chose, André S. Conradie, Pierre I. Cilliers, and Matthys M. Botha. Physics-based iterative scheme for computing antenna array embedded element patterns. *Microwave and Optical Technology Letters*, 65(8):2359–2365, 2023.

[44] Tomislav Marinović, Dirk Izak Leon De Villiers, Dave J. Bekers, Martin N. Johansson, Anders Stjernman, Rob Maaskant, and Guy A. E. Vandenbosch. Fast characterization of mutually coupled array antennas using isolated antenna far-field data. *IEEE Transactions on Antennas and Propagation*, 69(1):206–218, 2021.

[45] Ha Bui-Van, Jens Abraham, Michel Arts, Quentin Gueuning, Christopher Raucy, David González-Ovejero, Eloy de Lera Acedo, and Christophe Craeye. Fast and accurate simulation technique for large irregular arrays. *IEEE Transactions on Antennas and Propagation*, 66(4):1805–1817, 2018.

[46] Quentin Gueuning, Eloy de Lera Acedo, Anthony Keith Brown, and Christophe Craeye. An inhomogeneous plane-wave based single-level fast direct solver for the scattering analysis of extremely large antenna arrays. *IEEE Transactions on Antennas and Propagation*, 70(10):9511–9523, 2022.

[47] Robert Garbacz and R Turpin. A generalized expansion for radiated and scattered fields. *IEEE transactions on Antennas and Propagation*, 19(3):348–358, 1971.

[48] R. Harrington and J. Mautz. Theory of characteristic modes for conducting bodies. *IEEE Transactions on Antennas and Propagation*, 19(5):622–628, 1971.

[49] Martin Vogel, Gopinath Gampala, Danie Ludick, Ulrich Jakobus, and C. J. Reddy. Characteristic mode analysis: Putting physics back into simulation. *IEEE Antennas and Propagation Magazine*, 57(2):307–317, 2015.

[50] Mats Gustafsson, Lukas Jelinek, Kurt Schab, and Miloslav Capek. Unified theory of characteristic modes—part ii: Tracking, losses, and fem evaluation. *IEEE Transactions on Antennas and Propagation*, 70(12):11814–11824, 2022.

[51] Ling Guan, Zi He, Dazhi Ding, and Rushan Chen. Efficient characteristic mode analysis for radiation problems of antenna arrays. *IEEE Transactions on Antennas and Propagation*, 67(1):199–206, 2019.

[52] Dirk Manteuffel, Feng Han Lin, Teng Li, Nikolai Peitzmeier, and Zhi Ning Chen. Characteristic mode-inspired advanced multiple antennas: Intuitive insight into element-, interelement-, and array levels of compact large arrays and metantennas. *IEEE Antennas and Propagation Magazine*, 64(2):49–57, 2022.

[53] Tomas Lonsky, Pavel Hazdra, and Jan Kracek. Characteristic modes of dipole arrays. *IEEE Antennas and Wireless Propagation Letters*, 17(6):998–1001, 2018.

[54] Bryan Dennis Raines. *Systematic design of multiple antenna systems using characteristic modes*. PhD thesis, The Ohio State University, 2011.

[55] Qi Wu, Wei Su, Zhi Li, and Donglin Su. Reduction in out-of-band antenna coupling using characteristic mode analysis. *IEEE Transactions on Antennas and Propagation*, 64(7):2732–2742, 2016.

[56] D. J. Ludick. Applying the theory of characteristic modes to the analysis of finite antenna array elements and ground planes of finite sizes. In *2019 13th European Conference on Antennas and Propagation (EuCAP)*, pages 1–4, 2019.

[57] Sandip Ghosal, Rakesh Sinha, Arijit De, and Ajay Chakrabarty. Characteristic mode analysis of mutual coupling. *IEEE Transactions on Antennas and Propagation*, 70(2):1008–1019, 2022.

[58] Kurt R. Schab, John M. Outwater, Matthew W. Young, and Jennifer T. Bernhard. Eigenvalue crossing avoidance in characteristic modes. *IEEE Transactions on Antennas and Propagation*, 64(7):2617–2627, 2016.

[59] Shunxi Lou, Baoyan Duan, Wei Wang, Chaoliu Ge, and Sihao Qian. Analysis of finite antenna arrays using the characteristic modes of isolated radiating elements. *IEEE Transactions on Antennas and Propagation*, 67(3):1582–1589, 2019.

[60] G. S. Cheng and Chao-Fu Wang. A novel periodic characteristic mode analysis method for large-scale finite arrays. *IEEE Transactions on Antennas and Propagation*, 67(12):7637–7642, 2019.

[61] A.T. de Hoop. *The N-port Receiving Antenna and Its Equivalent Electrical Network*. Philips Research Laboratories, 1975.

[62] Karl F. Warnick, David B. Davidson, and David Buck. Embedded element pattern loading condition transformations for phased array modeling. *IEEE Transactions on Antennas and Propagation*, 69(3):1769–1774, 2021.

[63] Pietro Bolli, Maria Grazia Labate, Andre van Es, and Luca Stringhetti. Antenna & station performance update for skala4.1-al. Technical Report SKA-TEL-SKO-0001099, SKAO, Jodrell Bank Observatory, June 2020.

[64] Rowanne Steiner, Daniel C. X. Ung, Anouk Hubrechsen, Robert D. Jones, Randall B. Wayth, Mark J. Bentum, and A. Bart Smolders. Optimizing processing time of radio-astronomy antenna simulations using feko. *The Applied Computational Electromagnetics Society Journal (ACES)*, 35(10):1153–1160, Oct. 2020.

[65] Mirko Bercigli. Galileo emt software applied to ska-low. In *2023 17th European Conference on Antennas and Propagation (EuCAP)*, pages 1–5, 2023.

[66] A. Ludwig. The definition of cross polarization. *IEEE Transactions on Antennas and Propagation*, 21(1):116–119, 1973.

[67] Pietro Bolli, David B. Davidson, Mirko Bercigli, Paola Di Ninni, Maria Grazia Labate, Daniel Ung, and Giuseppe Virone. Computational electromagnetics for

the SKA-Low prototype station AAVS2. *Journal of Astronomical Telescopes, Instruments, and Systems*, 8(1):011017, 2022.

[68] Pietro Bolli, David Davidson, Maria Grazia Labate, and Stefan J. Wijnholds. Antenna pattern modelling accuracy for a very large aperture array radio telescope with strongly coupled elements. *IEEE Antennas and Wireless Propagation Letters*, pages 1–5, 2023.

[69] M. G. Labate, Robert Braun, Peter Dewdney, Mark Waterson, and Jeff Wagg. Ska1-low: Design and scientific objectives. In *2017 XXXIInd General Assembly and Scientific Symposium of the International Union of Radio Science (URSI GASS)*, pages 1–4, 2017.

[70] K. R. Schab and J. T. Bernhard. A group theory rule for predicting eigenvalue crossings in characteristic mode analyses. *IEEE Antennas and Wireless Propagation Letters*, 16:944–947, 2017.

[71] Michal Masek, Miloslav Capek, Lukas Jelinek, and Kurt Schab. Modal tracking based on group theory. *IEEE Transactions on Antennas and Propagation*, 68(2):927–937, 2020.

[72] R. Kyle. Mutual coupling between log-periodic antennas. *IEEE Transactions on Antennas and Propagation*, 18(1):15–22, 1970.

[73] M. Hilbert, M.A. Tilston, and K.G. Balmain. Resonance phenomena of log-periodic antennas: characteristic-mode analysis. *IEEE Transactions on Antennas and Propagation*, 37(10):1224–1234, 1989.

[74] K. Balmain and J. Nkeng. Asymmetry phenomenon of log-periodic dipole antennas. *IEEE Transactions on Antennas and Propagation*, 24(4):402–410, 1976.

[75] Zhong-Lin Gong and K. Balmain. Reduction of the anomalous resonances of symmetric log-periodic dipole antennas. *IEEE Transactions on Antennas and Propagation*, 34(12):1404–1410, 1986.

[76] G. De Vito and G. Stracca. Comments on the design of log-periodic dipole antennas. *IEEE Transactions on Antennas and Propagation*, 21(3):303–308, 1973.

[77] Georgios Kyriakou, Pietro Bolli, Ravi Subrahmanyan, and David B. Davidson. Experimental verification of anomalous spectral features of skala4.1 antenna. In *2021 IEEE International Symposium on Antennas and Propagation and USNC-URSI Radio Science Meeting (APS/URSI)*, pages 47–48, 2021.

[78] M A Hassan, A Al Jabri, and K Al-Hakbani. Point-matching method for reduction of anomalous radiation of log-periodic dipole array. *Electronics Letters*, 27:1315–1317(2), July 1991.

[79] K. Jones and P. Mayes. Continuously scaled transmission lines with applications to log-periodic antennas. *IEEE Transactions on Antennas and Propagation*, 17(1):2–9, 1969.

[80] Jiacheng Zhao, Yikai Chen, and Shiwen Yang. In-band radar cross-section reduction of slot antenna using characteristic modes. *IEEE Antennas and Wireless Propagation Letters*, 17(7):1166–1170, 2018.

[81] Huiwen Sheng and Zhi Ning Chen. Radiation pattern improvement of cross-band dipoles using inductive-loading mode-suppression method. *IEEE Transactions on Antennas and Propagation*, 67(5):3467–3471, 2019.

[82] Peiyu Liang and Qi Wu. Characteristic mode analysis of antenna mutual coupling in the near field. *IEEE Transactions on Antennas and Propagation*, 66(7):3757–3762, 2018.

[83] Huan He, Yikai Chen, and Shiwen Yang. Novel low profile ultra-wideband capacitance loaded log-periodic monopole array with reduced transverse dimension. *IET Microwaves, Antennas & Propagation*, 13(9):1443–1449, 2019.

[84] R. Carrel. The design of log-periodic dipole antennas. In *1958 IRE International Convention Record*, volume 9, pages 61–75, 1961.

[85] R.H. DuHamel and M.E. Armstrong. Log-periodic transmission line circuits - part i: One-port circuits. *IEEE Transactions on Microwave Theory and Techniques*, 14(6):264–274, 1966.

[86] James McLean, Robert Sutton, and Heinrich Foltz. Investigation of the stop region of a compressed log-periodic dipole antenna. In *2014 IEEE Antennas and Propagation Society International Symposium (APSURSI)*, pages 1314–1315, 2014.

[87] D. Nyquist and K. Chen. Traveling wave antenna with non-dissipative loading. In *1958 IRE International Convention Record*, volume 14, pages 200–211, 1966.

[88] A.D. Yaghjian and S.R. Best. Impedance, bandwidth, and q of antennas. *IEEE Transactions on Antennas and Propagation*, 53(4):1298–1324, 2005.

[89] Miloslav Capek, Pavel Hazdra, and Jan Eichler. A method for the evaluation of radiation q based on modal approach. *IEEE Transactions on Antennas and Propagation*, 60(10):4556–4567, 2012.

[90] Agaram Raghunathan, Ravi Subrahmanyan, N. Udaya Shankar, Saurabh Singh, Jishnu Nambissan, K. Kavitha, Nivedita Mahesh, R. Somashekar, Gaddam Sindhu, B. S. Girish, K. S. Srivani, and Mayuri S. Rao. A floating octave bandwidth cone-disk antenna for detection of cosmic dawn. *IEEE Transactions on Antennas and Propagation*, 69(10):6209–6217, 2021.

[91] Georgios Kyriakou, Pietro Bolli, and Lorenzo Mezzadrelli. Suppresion of log-periodic dipole antenna spurious radiation by lumped element loading for radioastronomical application. *Radio Science*, n/a(n/a):e2023RS007758, 2023. e2023RS007758 2023RS007758.

[92] G. Macario, G. Pupillo, G. Bernardi, P. Di Ninni, G. Comoretto, P. Bolli, A. Mattana, J. Monari, F. Perini, M. Schiaffino, M. Sokolowski, and R. Wayth. Intrinsic cross polarisation maps from all-sky observations: an initial verification of ska-low station polarisation response. *Publications of the Astronomical Society of Australia (under review)*, 2023.

[93] Jean Cavillot, Denis Tihon, Francisco Mesa, Eloy De Lera Acedo, and Christophe Craeye. Efficient simulation of large irregular arrays on a finite ground plane. *IEEE Transactions on Antennas and Propagation*, 68(4):2753–2764, 2020.

[94] Pietro Bolli, Mirko Bercigli, Paola Di Ninni, Maria Grazia Labate, and Giuseppe Virone. Preliminary analysis of the effects of the ground plane on the element patterns of ska1-low. In *2020 14th European Conference on Antennas and Propagation (EuCAP)*, pages 1–5, 2020.

[95] Pietro Bolli, Mirko Bercigli, Paola Di Ninni, Lorenzo Mezzadrelli, and Giuseppe Virone. Impact of mutual coupling between SKALA4.1 antennas to the spectral smoothness response. *Journal of Astronomical Telescopes, Instruments, and Systems*, 8(1):011023, 2022.

[96] Georgios Kyriakou, Pietro Bolli, and Mirko Bercigli. Spectral smoothness of ground plane backed log-periodic dipole antennas for radioastronomical applications (under review). *International Journal of Antennas and Propagation*, 2023.

[97] Jean Cavillot, Christophe Craeye, and Eloy De Lera Acedo. Efficiency of a 3d metallic antenna on top of finite ground plane and soil. In *2022 International Conference on Electromagnetics in Advanced Applications (ICEAA)*, pages 245–247, 2022.

[98] A. T. Sutinjo, T. M. Colegate, R. B. Wayth, P. J. Hall, E. de Lera Acedo, T. Booler, A. J. Faulkner, L. Feng, N. Hurley-Walker, B. Juswardy, and et al. Characterization of a low-frequency radio astronomy prototype array in western australia. *IEEE Transactions on Antennas and Propagation*, 63(12):5433–5442, Dec 2015.

[99] Georgios Kyriakou and Pietro Bolli. Effects of the grid mesh on the isolated skala4.1 antenna. Technical Report SKAO-TEL-0002315, SKAO, Jodrell Bank Observatory, September 2023.

[100] Ang Li and Christos Masouros. Exploiting constructive mutual coupling in p2p mimo by analog-digital phase alignment. *IEEE Transactions on Wireless Communications*, 16(3):1948–1962, 2017.

[101] Sutinjo, A. T., Ung, D. C. X., Sokolowski, M., Kovaleva, M., and McSweeney, S. System equivalent flux density of a low-frequency polarimetric phased array interferometer. *A&A*, 660:A134, 2022.

[102] Cathryn M. Trott and Randall B. Wayth. Spectral calibration requirements of radio interferometers for epoch of reionisation science with the ska. *Publications of the Astronomical Society of Australia*, 33:e019, 2016.

[103] Alec T Josaitis, Aaron Ewall-Wice, Nicolas Fagnoni, and Eloy de Lera Acedo. Array element coupling in radio interferometry I: a semi-analytic approach. *Monthly Notices of the Royal Astronomical Society*, 514(2):1804–1827, 04 2022.

[104] Stefan J. Wijnholds, Michel Arts, Pietro Bolli, Paola di Ninni, and Giuseppe Virone. Using embedded element patterns to improve aperture array calibration. In *2019 International Conference on Electromagnetics in Advanced Applications (ICEAA)*, pages 0437–0442, 2019.

[105] Paola Di Ninni, Mirko Bercigli, Pietro Bolli, Maria Grazia Labate, and Stefan J. Wijnholds. Mutual coupling mitigation in array dense regime by an antenna distribution optimization in ska1-low. *Radio Science*, 57(11):e2022RS007507, 2022. e2022RS007507 2022RS007507.

[106] Randall B. Wayth, David Davidson, and Daniel Ung. Aperture efficiency of beamforming with mutual coupling in ska-low stations. In *2023 XXXVth General Assembly and Scientific Symposium of the International Union of Radio Science (URSI GASS)*, pages 1–4, 2023.

[107] Tobia D. Carozzi, Pietro Bolli, Ravi Subrahmanyan, and Robert Braun. Differentially rotated skala4.1 antennas in vogel configurations. In *2023 XXXVth General Assembly and Scientific Symposium of the International Union of Radio Science (URSI GASS)*, pages 1–4, 2023.

[108] David B. Davidson, Randall B. Wyath, and Daniel Ung. Evaluation of alternative ska-low station layouts. In *2023 XXXVth General Assembly and Scientific Symposium of the International Union of Radio Science (URSI GASS)*, pages 1–4, 2023.

[109] G. Virone, F. Paonessa, O. A. Peverini, G. Addamo, R. Orta, R. Tascone, and P. Bolli. Antenna pattern measurements with a flying far-field source (hexacopter). In *2014 IEEE Conference on Antenna Measurements & Applications (CAMA)*, pages 1–2, 2014.

[110] Juan D. González-Teruel, Scott B. Jones, David A. Robinson, Jaime Giménez-Gallego, Raúl Zornoza, and Roque Torres-Sánchez. Measurement of the broadband complex permittivity of soils in the frequency domain with a low-cost vector network analyzer and an open-ended coaxial probe. *Computers and Electronics in Agriculture*, 195:106847, 2022.

[111] Fabio Paonessa, Lorenzo Ciorba, Giuseppe Virone, Pietro Bolli, Alessio Magro, Andrew McPhail, Dave Minchin, and Raunaq Bhushan. SKA-Low Prototypes Deployed in Australia: Synoptic of the UAV-Based Experimental Results. *URSI Radio Science Letters*, 2:21, August 2020.

[112] Fabio Paonessa, Lorenzo Ciorba, Georgios Kyriakou, Pietro Bolli, and Giuseppe Virone. Uav-based measurement of sharp spectral resonances in mutually coupled ska-low elements. *IEEE Antennas and Wireless Propagation Letters*, pages 1–5, 2023.

[113] Miloslav Capek, Vit Losenicky, Lukas Jelinek, and Mats Gustafsson. Validating the characteristic modes solvers. *IEEE Transactions on Antennas and Propagation*, 65(8):4134–4145, 2017.

[114] Georgios Kyriakou, Pietro Bolli, and Giuseppe Virone. Characteristic modes analysis of mutually coupled log-periodic dipole antennas. In *2023 17th European Conference on Antennas and Propagation (EuCAP)*, pages 1–4, 2023.

[115] Sandip Ghosal, Rakesh Sinha, Arijit De, Ajay Chakrabarty, and Hungsun Son. Theory of coupled characteristic modes. *IEEE Transactions on Antennas and Propagation*, 68(6):4677–4687, 2020.

[116] Miloslav Capek, Lukas Jelinek, Petr Kadlec, and Mats Gustafsson. Memetic scheme for inverse design using exact reanalysis of method-of-moments models–part 1: Theory and implementation. *arXiv preprint arXiv:2110.08044*, 2021.

[117] A. Ludwig. Mutual coupling, gain and directivity of an array of two identical antennas. *IEEE Transactions on Antennas and Propagation*, 24(6):837–841, 1976.

[118] Georgios Kyriakou and Pietro Bolli. Investigating adverse low-frequency effects of log-periodic dipole antenna resonant radiation. In *2023 IEEE International Symposium on Antennas and Propagation and USNC-URSI Radio Science Meeting (USNC-URSI)*, pages 771–772, 2023.

[119] G. Bernardi, M. McQuinn, and L. J. Greenhill. Foreground Model and Antenna Calibration Errors in the Measurement of the Sky-averaged λ21 cm Signal at z~20. *The Astrophysical Journal*, 799:90, January 2015.

[120] G. Bernardi, J. T. L. Zwart, D. Price, L. J. Greenhill, A. Mesinger, J. Dowell, T. Eftekhari, S. W. Ellingson, J. Kocz, and F. Schinzel. Bayesian constraints on the global 21-cm signal from the cosmic dawn. *Monthly Notices of the Royal Astronomical Society*, 461(3):2847–2855, 2016.

[121] Judd D. Bowman, Alan E. E. Rogers, Raul A. Monsalve, Thomas J. Mozdzen, and Nivedita Mahesh. An absorption profile centred at 78 megahertz in the sky-averaged spectrum. *Nature*, 555(67), 2018.

[122] Saurabh Singh, Jishnu Nambissan T., Ravi Subrahmanyan, N. Udaya Shankar, B. S. Girish, A. Raghunathan, R. Somashekar, K. S. Srivani, and Mayuri Sathyanarayana Rao. On the detection of a cosmic dawn signal in the radio background. *Nature Astronomy*, February 2021.

[123] T. J. Mozdzen, J. D. Bowman, R. A. Monsalve, and A. E. E. Rogers. Limits on foreground subtraction from chromatic beam effects in global redshifted

21 cm measurements. *Monthly Notices of the Royal Astronomical Society*, 455(4):3890–3900, February 2016.

[124] Keith Tauscher, David Rapetti, Bang D. Nhan, Alec Handy, Neil Bassett, Joshua Hibbard, David Bordenave, Richard F. Bradley, and Jack O. Burns. Global 21 cm Signal Extraction from Foreground and Instrumental Effects. IV. Accounting for Realistic Instrument Uncertainties and Their Overlap with Foreground and Signal Models. *The Astrophysical Journal*, 915(1):66, July 2021.

[125] J. Cumner, E. de Lera Acedo, D. I. L. de Villiers, D. Anstey, C. I. Kolitsidas, B. Gurdon, N. Fagnoni, P. Alexander, G. Bernardi, H. T. J. Bevins, S. Carey, J. Cavillot, R. Chiello, C. Craeye, W. Croukamp, J. A. Ely, A. Fialkov, T. Gessey-Jones, Q. Gueuning, W. Handley, R. Hills, A. T. Josaitis, G. Kulkarni, A. Magro, R. Maiolino, P. D. Meerburg, S. Mittal, J. R. Pritchard, E. Puchwein, N. Razavi-Ghods, I. L. V. Roque, A. Saxena, K. H. Scheutwinkel, E. Shen, P. H. Sims, O. Smirnov, M. Spinelli, and K. Zarb-Adami. Radio antenna design for sky-averaged 21cm cosmology experiments: The reach case. *Journal of Astronomical Instrumentation*, 11(01):2250001, 2022.

[126] H. K. Vedantham, L. V. E. Koopmans, A. G. de Bruyn, S. J. Wijnholds, B. Ciardi, and M. A. Brentjens. Chromatic effects in the 21 cm global signal from the cosmic dawn. *Monthly Notices of the Royal Astronomical Society*, 437(2):1056–1069, January 2014.

[127] Nivedita Mahesh, Judd D. Bowman, Thomas J. Mozdzen, Alan E. E. Rogers, Raul A. Monsalve, Steven G. Murray, and David Lewis. Validation of the EDGES Low-band Antenna Beam Model. *The astronomical Journal*, 162(2):38, August 2021.

[128] Richard F. Bradley, Keith Tauscher, David Rapetti, and Jack O. Burns. A ground plane artifact that induces an absorption profile in averaged spectra from global 21 cm measurements, with possible application to edges. *The Astrophysical Journal*, 874(2):153, Apr 2019.

[129] Saurabh Singh, Jishnu Nambissan T, Ravi Subrahmanyan, N Udaya Shankar, BS Girish, A Raghunathan, R Somashekar, KS Srivani, and Mayuri Sathyanarayana Rao. On the detection of a cosmic dawn signal in the radio background. *Nature Astronomy*, 6(5):607–617, 2022.

[130] G. B. Taylor, S. W. Ellingson, N. E. Kassim, J. Craig, J. Dowell, C. N. Wolfe, J. Hartman, G. Bernardi, T. Clarke, A. Cohen, N. P. Dalal, W. C. Erickson, B. Hicks, L. J. Greenhill, B. Jacoby, W. Lane, J. Lazio, D. Mitchell, R. Navarro, S. M. Ord, Y. Pihlström, E. Polisensky, P. S. Ray, L. J. Rickard, F. K. Schinzel, H. Schmitt, E. Sigman, M. Soriano, K. P. Stewart, K. Stovall, S. Tremblay, D. Wang, K. W. Weiler, S. White, and D. L. Wood. First light for the first station of the long wavelength array. *Journal of Astronomical Instrumentation*, 01(01):1250004, 2012.

[131] Henrique R. Paravastu et al. Impedance Measurements of the Big Blade andFork Antennas on Ground Screensat the LWDA Site, 2007.

[132] Schmitt et al. Collected first light Engineering Memos from the Development of the Ground Screen Subsystem, 2009.

[133] D C Price, L J Greenhill, A Fialkov, G Bernardi, H Garsden, B R Barsdell, J Kocz, M M Anderson, S A Bourke, J Craig, M R Dexter, J Dowell, M W Eastwood, T Eftekhari, S W Ellingson, G Hallinan, J M Hartman, R Kimberk, T Joseph W Lazio, S Leiker, D MacMahon, R Monroe, F Schinzel, G B Taylor, E Tong, D Werthimer, and D P Woody. Design and characterization of the Large-aperture Experiment to Detect the Dark Age (LEDA) radiometer systems. *Monthly Notices of the Royal Astronomical Society*, 478(3):4193–4213, 05 2018.

[134] M. Spinelli, G. Bernardi, H. Garsden, L. J. Greenhill, A. Fialkov, J. Dowell, and D. C. Price. Spectral index of the Galactic foreground emission in the 50-87 MHz range. *Monthly Notices of the Royal Astronomical Society*, 505(2):1575–1588, August 2021.

[135] J. Dowell. Parametric Model for the first light-1 Dipole Response as a Function of Frequency, 2011.

[136] S. W. Ellingson, G. B. Taylor, J. Craig, J. Hartman, J. Dowell, C. N. Wolfe, T. E. Clarke, B. C. Hicks, N. E. Kassim, P. S. Ray, L. J Rickard, F. K. Schinzel, and K. W. Weiler. The lwa1 radio telescope. *IEEE Transactions on Antennas and Propagation*, 61(5):2540–2549, 2013.

[137] Marta Spinelli, Gianni Bernardi, and Mario G. Santos. On the contamination of the global 21-cm signal from polarized foregrounds. *Monthly Notices of the Royal Astronomical Society*, 489(3):4007–4015, November 2019.

[138] Brian C. Hicks, Nagini Paravastu-Dalal, Kenneth P. Stewart, William C. Erickson, Paul S. Ray, Namir E. Kassim, Steve Burns, Tracy Clarke, Henrique Schmitt, Joe Craig, and et al. A wide-band, active antenna system for long wavelength radio astronomy. *Publications of the Astronomical Society of the Pacific*, 124(920):1090–1104, Oct 2012.

[139] M Spinelli, G Kyriakou, G Bernardi, P Bolli, L J Greenhill, A Fialkov, and H Garsden. Antenna beam characterization for the global 21-cm experiment LEDA and its impact on signal model parameter reconstruction. *Monthly Notices of the Royal Astronomical Society*, 515(2):1580–1597, 07 2022.

[140] K.A. Michalski and J.R. Mosig. Multilayered media green's functions in integral equation formulations. *IEEE Transactions on Antennas and Propagation*, 45(3):508–519, 1997.

[141] Jishnu Nambissan T., Ravi Subrahmanyan, R. Somashekar, N. Udaya Shankar, Saurabh Singh, A. Raghunathan, B. S. Girish, K. S. Srivani, and Mayuri Sathyanarayana Rao. Saras 3 cd/eor radiometer: design and performance of the receiver. *Experimental Astronomy*, Jan 2021.

[142] MM Weiner. Validation of the numerical electro-magnetics code (nec) for antenna wire elements in proximity to earth. Technical report, MITRE CORP BEDFORD MA, 1991.

[143] T. J. Mozdzen, N. Mahesh, R. A. Monsalve, A. E. E. Rogers, and J. D. Bowman. Spectral index of the diffuse radio background between 50 and 100 MHz. *Monthly Notices of the Royal Astronomical Society*, 483(4):4411–4423, March 2019.

[144] Raul A. Monsalve, Alan E. E. Rogers, Judd D. Bowman, Nivedita Mahesh, Steven G. Murray, Thomas J. Mozdzen, Leroy Johnson, John Barrett, Titu Samson, and David Lewis. Absolute Calibration of Diffuse Radio Surveys at 45 and 150 MHz. *arXiv e-prints*, page arXiv:2012.11019, December 2020.

[145] Dominic Anstey, Eloy de Lera Acedo, and Will Handley. A General Bayesian Framework for Foreground Modelling and Chromaticity Correction for Global 21cm Experiments. *arXiv e-prints*, page arXiv:2010.09644, October 2020.

[146] C. G. T. Haslam, C. J. Salter, H. Stoffel, and W. E. Wilson. A 408 MHz all-sky continuum survey. II. The atlas of contour maps. *Astronomy and Astrophysics Supplement Series*, 47:1–143, January 1982.

[147] D. C. Price. Beamforming approaches towards detecting the 21-cm global signal from cosmic dawn with radio array telescopes. *Publications of the Astronomical Society of Australia*, 39:e060, 2022.

[148] Steven W. Ellingson. Sensitivity of antenna arrays for long-wavelength radio astronomy. *IEEE Transactions on Antennas and Propagation*, 59(6):1855–1863, 2011.

[149] Junhua Gu, Jingying Wang, Huanyuan Shan, Qian Zheng, Quan Guo, Yan Huang, Kuanjun Li, and Tianyang Liu. Global cd/eor signal detection with a dense digital beamforming array and beyond, 2022.

[150] André Young, Marianna V. Ivashina, Rob Maaskant, Oleg A. Iupikov, and David Bruce Davidson. Improving the calibration efficiency of an array fed reflector antenna through constrained beamforming. *IEEE Transactions on Antennas and Propagation*, 61(7):3538–3545, 2013.

[151] Christopher DiLullo, Gregory B. Taylor, and Jayce Dowell. Using the long wavelength array to search for cosmic dawn. *Journal of Astronomical Instrumentation*, 09(02):2050008, 2020.

[152] Christopher DiLullo, Jayce Dowell, and Gregory B. Taylor. Improvements to the search for cosmic dawn using the long wavelength array. *Journal of Astronomical Instrumentation*, 10(04):2150015, 2021.

[153] Dominic Anstey, John Cumner, Eloy de Lera Acedo, and Will Handley. Informing antenna design for sky-averaged 21-cm experiments using a simulated Bayesian data analysis pipeline. *Monthly Notices of the Royal Astronomical Society*, 509(4):4679–4693, November 2022.

Appendix A

Current vector of full RWG discretization in FEKO CMA

Let $\bar{J}_{RGW}$ be the $N_{RWG} \times 1$ RWG element discretization current vector and $\bar{J}_{ME}$ the $N_{ME} \times 1$ current vector per mesh element (ME) rather than per basis function. These two vectors are connected by a constant $N_{ME} \times N_{RWG}$ matrix L for a given mesh:

$$\bar{J}_{ME} = L\bar{J}_{RWG} \tag{A.1}$$

Let us consider the case of wires, where any wire current entry $J_{ME;n}$ is only the result of a linear combination of two RWG functions of the wire vertices, so two entries $J_{RWG;n_1}$, $J_{RWG;n_2}$ weighted as: $J_{ME;n} = L_{nn_1}J_{RWG;n_1} + L_{nn_2}J_{RWG;n_2}$. All the other entries of row n of L are then zero. For the case of a standard MoM analysis, one can have both the vectors available from the FEKO output files ($\bar{J}_{ME}$ is given in its output `.os` file and $\bar{J}_{RWG}$ in its `.str` file). The problem faced when using the Characteristic Modes Analysis is that the modal $\bar{J}_{RWG}$ vectors are not available in any output file, so any reconstruction would require the knowledge of L. If we wish to use the same mesh for both analyses, then the $2N_{ME}$ real non-zero entries of the L matrix can uniquely be determined by using the known results (at any one frequency) of the complex vectors J_{RWG}, J_{ME} in the $2N_{ME}$ equations that Eq. (A.1) represents, when taking into account both real and imaginary part.

Another important input in order to calculate the unkwnown CMA $\bar{J}_{RWG}$ eigenvectors is the $N_{RWG} \times N_{RWG}$ MoM impedance matrix Z. This can also be obtained in the form of a `.mat` file by FEKO when running any simulation. If the matrix L is then known for our mesh, the next steps to determine any modal eigenvector $\bar{J}_{RWG}$ which corresponds to an eigevalue λ, from its respective known $\bar{J}_{ME}$ are as follows:

1. calculate, using the Matlab function `null`, the null space of $\Im\{Z\} - \lambda\Re\{Z\}$ at a given tolerance (by default $N_{RWG} \cdot \epsilon(\|Z\|)$, where ϵ is the floating point relative accuracy at order of magnitude $\|Z\|$). This will result in a multitude of vectors $\bar{J}_{RWG}$ that are all possible eigenvectors according to the tolerance
2. among all the $\bar{J}_{RWG}$ eigenvectors of the previous step, choose that which minimizes the relative error $\|\bar{J}_{ME} - rL\bar{J}_{RWG}\|/\|\bar{J}_{ME}\|$, where $r = \|\bar{J}_{ME}\|/\|L\bar{J}_{RWG}\|$.

> This step will result in the RWG eigenvector which is numerically closer, when transformed by matrix L, to the ME eigenvector available by the FEKO results.

It is mentioned in Sec. 5.2 that this procedure is needed only for the cross-product quadratic forms $\bar{J}_{m_1} Z_{12} \bar{J}_{m_2}^T$, which are written in the RWG vector sense. In fact, for reasons of consistent normalization of the various such quadratic forms, and since it was easy to further apply this method to them, it has been used also in calculating the self-product quadratic forms $\bar{J}_{m_{1(2)}} Z_{11(22)} \bar{J}_{m_{1(2)}}^T$. A final useful check that the calculations are correct is also performed by checking the condition $\bar{J}_{m_1} Z_{12} \bar{J}_{m_2}^T = \bar{J}_{m_2} Z_{21} \bar{J}_{m_1}^T$ that has been ideally stated in Sec. 5.2.2. Our results showed that many of the eigenvectors that Matlab `null` calculates, although respecting the given tolerance, do not conform to that condition.

Furthermore, the eigenvectors of Matlab are actually unit, while the actual eigenvectors should have a magnitude such that the quadratic forms mentioned above (with a 1/2 factor) are equal to the modal power $P = P_{rad;m}(1 + j\lambda)$, whether that is indexed by m of the coupled antenna system or by m_1, m_2 of the single antenna. Some multiplicative factors should therefore appear in each of the equated sides of Eq. (5.2), namely $P_{rad,m_1}/(\bar{J}_{m_1} Z_{11} \bar{J}_{m_1}^T)$ on the right-hand-side and $P_{rad,m}/(\bar{J}_m Z \bar{J}_m^T)$ on the left-hand-side.

Appendix B

Efficient data storage for EEP simulations using array network power computations

We will outline here an interesting use of the array network theory formulation to calculate the input (or radiation) power, which is defined as the active power minus the losses and is used as the denominator in the directivity definition. The radiated power usually needs the full 3D pattern to be calculated at a good sampling rate, which for a lot of antennas and frequencies becomes intensive to store.

If we have the antenna S-parameter data available, denoted $\mathbf{S}_A$, we can transform our short-circuit EEPs to whatever port termination we want. Let's denote the θ, ϕ components of the short-circuited termination EEPs as $\bar{E}_\theta^{sc}$, $\bar{E}_\phi^{sc}$, 256 vector elements. Then according to [1] we can transform to a $Z_g = 100\ \Omega$, which is the LNA input impedance and our antenna reference impedance, as:

$$\begin{pmatrix} E_\theta^{Z_g} & E_\phi^{Z_g} \end{pmatrix} = (\mathbf{Z}_A + Z_g \mathbf{I}_n)^{-1} \cdot \mathbf{Z}_A \cdot \begin{pmatrix} \bar{E}_\theta^{sc} & \bar{E}_\phi^{sc} \end{pmatrix} \tag{B.1}$$

where $\mathbf{Z}_A = Z_g \cdot (\mathbf{I}_{256} - \mathbf{S}_A)^{-1} \cdot (\mathbf{I}_{256} + \mathbf{S}_A)$ is the antenna matrix. To transform to directivities, we need to calculate for each pattern n:

$$D_n^{Z_g} = \frac{4\pi \cdot \frac{1}{2\eta_0}(|E_{n,\theta}^{Z_g}|^2 + |E_{n,\phi}^{Z_g}|^2)}{P_{n,in}^{Z_g}} \tag{B.2}$$

In this equation, $P_{n,in}^{Z_g} = \frac{V_g^2}{2} \cdot \Re\left\{ Y_{n,in}^{Z_g} \right\}$ is the input power (in W) calculated using the source excitation ($V_g = 1\ V$ in our case) and the input impedance of antenna n when all other port terminations are Z_g. In this case it can be computed as $Y_{n,in}^{Z_g} = [(\mathbf{Z}_A + Z_g \mathbf{I}_n)^{-1} \cdot \mathbf{Z}_A \cdot (\mathbf{Z}_A + Z_g \mathbf{I}_n)^{-H}]_{nn}$ and $[\cdot]_{mn}$ means the m-th row, n-th column element of a matrix. In our scheme, therefore, we only need to store one set of EEPs as a FEKO `.ffe` file containing $\bar{E}_\theta^{sc}$, $\bar{E}_\phi^{sc}$, $\bar{D}^{sc}$, and a `.s256p` file containing $\mathbf{S}_A$. Last, if we want to obtain such an input power calculation for the station beams, we need to reformulate the formula derived from [21, Ch. 4] as:

$$P_{in,st}^{Z_g} = \frac{1}{2} \cdot \bar{V}_g^T \cdot \Re\{(\mathbf{Z}_A + Z_g \mathbf{I}_n)^{-1} \cdot \mathbf{Z}_A \cdot (\mathbf{Z}_A + Z_g \mathbf{I}_n)^{-H}\} \cdot \bar{V}_g \tag{B.3}$$